UNIVERSITY OF OKLAHOMA

GRADUATE COLLEGE

OBSERVATION OF OPPOSITE SIGN WW WITH AN ASSOCIATED PHOTON PRODUCTION AT A CENTER OF MASS ENERGY OF 13 TEV WITH THE ATLAS DETECTOR AT THE LHC

A DISSERTATION

SUBMITTED TO THE GRADUATE FACULTY

in partial fulfillment of the requirements for the

Degree of

DOCTOR OF PHILOSOPHY

By

Joseph Earl Lambert
Norman, Oklahoma
2022

OBSERVATION OF OPPOSITE SIGN WW WITH AN ASSOCIATED PHOTON PRODUCTION AT A CENTER OF MASS ENERGY OF 13 TEV WITH THE ATLAS DETECTOR AT THE LHC

A DISSERTATION APPROVED FOR THE
HOMER L. DODGE DEPARTMENT OF PHYSICS
ASTRONOMY

BY THE COMMITTEE CONSISTING OF

Dr. Braden Abbott, Chair

Dr. Howard Baer

Dr. Kerry Magruder

Dr. Bruce Mason

Dr. John Stupak

Acknowledgments

I would like to thank my advisor, Brad Abbott, for continue to work with me on all of the various projects I have had the opportunity to be a part of during my journey to get my PhD. I would not have completed my PhD without you.

Everything that I needed to know how to successfully analysis collision data was gained during my time on the WWW analysis. I would like to thank Junjie Zhu, Wenhao Xu, Jessica MetCalfe, Vallary Bhopatkar, and Muhammad Alhroob who worked with me to help me reach this point. My success on the analysis describe in this thesis was made possible through the work and experience I gained during this time.

I would also like to thank Alexander Paramonov and Marco Trovato. Working with both of you was the most fun and rewarding part of my graduate career. I was able to do work that I enjoyed and gained myriad technical skills that that continue to help me to this day.

Finally, I would like to thank Philip Gutierrez, Daniel Wilburn and Muhammad Alhroob for helping make this analysis a success.

Contents

List of Tables

List of Figures

Abstract

The analysis presented in this thesis expects to provide the first observation of the opposite sign WW with an associated photon process and to measure its fiducial cross section. The analysis uses proton-proton collision data collected between 2015 and 2018 using the ATLAS detector at a center of mass energy of 13 TeV corresponding to an integrated luminosity of 139 inverse fb. Only events where one W boson decays to an electron and the other W boson decays to a muon are considered. Significant deviations from the measured opposite sign WW with an associated photon production cross section and the Standard Model (SM) prediction can provide evidence for beyond the Standard Model (BSM) physics. In addition, any deviation from the SM prediction can be parameterized in the framework of an effective field theory (EFT) and limits can be placed on these EFT parameters. The results of the EFT measurement are beyond the scope of this thesis and will be presented in another thesis. The majority of the background events arise from processes with prompt photons including tt with an associated photon and Z boson production with an associated photon. The analysis also considers backgrounds from non-prompt photons from electrons or hadrons. To improve the measurement sensitivity, a BDT (boosted decision tree) is trained using several well modeled input variables. The BDT combines the information from the input variables into a single variable: the BDT score. The opposite sign WW with an associated photon fiducial cross section and statistical significance are calculated by performing a binned maximum likelihood fit using the BDT output distribution. The expected statistical significance of the measurement is 7.2 σ and the expected fiducial cross section is 10.5 $\pm$ 14% (cross section) $\pm$ 15% fb (measurement). Where the cross section uncertainty is associated with the determination of the fiducial volume and the measurement uncertainty is associated with the determination of the signal strength using the binned maximum likelihood fit.

Chapter 1

Introduction

The analysis presented in this thesis seeks to provide the first observation of the $W^{\pm}W^{\mp}\gamma$ process and measure it's fiducial cross section using data the proton-proton collision data collected at a center of mass energy ($\sqrt{s}$) of 13 TeV by the ATLAS detector in the period from 2015 to 2018.

Chapter 2 will introduce the standard model (SM) and the $W^{\pm}W^{\mp}\gamma$ production process as well as describe how Monte Carlo methods can be used to provide a theoretical prediction that can be compared to data. Chapter 3 will describe the Large Hadron Collider (LHC) and the ATLAS detector used to collect this data. Chapter 4 will describe the data collected by the ATLAS detector used in the analysis presented in this thesis. Chapter 5 will describe the MC simulation samples used for the theoretical prediction for the $W^{\pm}W^{\mp}\gamma$ process as well as other processes that act as backgrounds to the $W^{\pm}W^{\mp}\gamma$ process. Chapter 6 describes the procedure used to reconstruct the particles in the underlying interaction from the raw data from the ATLAS detector and the simulated ATLAS detector for MC samples. Chapter 7 describes the systematic uncertainties that are included in the MC simulated samples resulting from uncertainties in the underlying theoretical prediction as well as the result of detector resolution, noise, and efficiencies. Chapter 8 describes the requirements used to select events enriched in the $W^{\pm}W^{\mp}\gamma$ process and the backgrounds that pass those same cuts, defining the $e^{\pm}\mu^{\mp}\gamma$ signal region. Chapter 9 describes how each of the backgrounds to the $e^{\pm}\mu^{\mp}\gamma$ signal region are estimated and validated. Chapter 10 describes the boosted decision tree (BDT) that is used to combine information from many variables into a single variable that encodes all of the relevant information in the input variables to separate the $W^{\pm}W^{\mp}\gamma$ signal and the various backgrounds. Chapter 11 describes the binned maximum likelihood used to fit the BDT output distribution, providing the fiducial cross section for the $W^{\pm}W^{\mp}\gamma$ process and the statistical significance of the measurement. Chapter 12 summarizes the measurement procedure and presents the expected results.

Due to the fact that the analysis has not been given permission to unblind, we cannot look at the data in the Signal Region and only provide the expected results. Permission to unblind will be given once the independent effective field theory component of the analysis has been reviewed. Upon unblinding, significant deviations from the measured $W^{\pm}W^{\mp}\gamma$ cross section and the Standard Model prediction provide can provide evidence for beyond the Standard Model (BSM) physics. In addition, any deviation from the SM prediction can be parameterized in the framework of an effective field theory (EFT) and limits can be placed on these EFT parameters. The results of the EFT measurement are beyond the scope of this thesis and will be presented in another thesis.

Chapter 2

The Standard Model Prediction

2.1 The Standard Model

The world around us can be characterized by the matter that makes up our universe and the forces that allow matter to interact. The known forces are the familiar gravitational and electromagnetic forces and the less familiar, but no less important, strong and weak interactions. These forces are described by two pillars of modern physics: general relativity and the Standard Model (SM) [1, 2, 3, 4]. General relativity is concerned with the nature of spacetime and gravitational interactions. While gravity plays a large role in our everyday life, it has a negligible effect at the smallest scales that can be probed with modern technology.

The Standard Model is a gauge field theory within the framework of quantum field theory (QFT) based on the symmetry group $SU(3) \otimes SU(2) \otimes U(1)$ [5, 6, 7, 8]. QFT extends quantum mechanics to the relativistic regime and allows for the creation and destruction of particles and the concept of quantum fields. Electroweak interactions are described by the $SU(2) \otimes U(1)$ group and quantum chromodynamics (QCD) or the strong interaction is described by $SU(3)$ group. The electroweak interaction is composed of the electromagnetic ($U(1)$) and weak interactions ($SU(2)$) responsible for transmutation of nuclei during radioactive decay. In addition to the electroweak and strong interactions, the Standard Model predicts the existence of the Higgs boson that is responsible for giving mass to the particles of the Standard Model through spontaneous symmetry breaking [9, 10, 11, 12]. The Higgs potential exists as part of the electroweak interaction and gives mass to many of the Standard Model particles. The strong interaction overcomes the repulsive electromagnetic force between protons in atoms and holds nuclei together. The Standard Model provides accurate predictions related to interactions at the smallest scales that can be experimentally probed, particularly those that arise in high energy collisions produced within the ATLAS [13] detector by the Large Hadron Collider (LHC) [14]. One of the predictions of the SM is the rare production of $W^{\pm}W^{\mp}\gamma$ events.

The quantized gauge fields of the Standard Model exist in 4 dimensional Minkowski spacetime exhibit local gauge invariance with respect the $SU(3) \otimes SU(2) \otimes U(1)$ symmetry groups. Fields are associated with the generators of the groups of the Standard Model. By quantizing these fields, particles arise as well as interactions between particles. The particles predicted by the Standard Model are given in Figure 2.1.

Each particle is distinguished by a set of quantum numbers that determine the properties and interactions that each particle partakes in. One of the most fundamental quantum numbers is called spin. Fermions have half-integer spin and bosons have integer spin. Fermions make up the matter of the universe while bosons mediate the forces that allow the particles to interact. The other quantum numbers that we will discuss determine whether or not the particles are charged under a particular interaction. For example, electrons have electric charge; therefore, they interact through the electromagnetic force. In the same way, particles of the Standard Model can carry a charge related to the weak and strong interactions. These interactions are mediated through the exchange of a boson associated with the interaction. Particles that carry electric charge can interact by exchanging photons, particles that carry weak charge can interact by exchanging $W^{\pm}$ and Z bosons, and particles charged under the strong interaction can interact by exchanging gluons, or mesons built from the combination of two gluons. These bosons can be exchanged only between particles that carry quantum numbers associated with, or are charged under, the particular interaction. The Standard Model is a non-Abelian quantum field theory. The implication of this is that the bosons can interact with each other and with themselves. For example the charged massive $W^{\pm}$ bosons carries electric charge so they can interact by exchanging photons. The $W^{\pm}$ bosons are also charged under the weak interaction so they can interact with other $W^{\pm}$ bosons. This self-interaction is of particular importance to the study of the production of $W^{\pm}W^{\mp}\gamma$ as will be discussed later in this chapter.

Fermions can be either leptons or quarks. Leptons have non-zero quantum numbers for the weak isospin that is associated with the $SU(2)$ interaction and hypercharge which is associated with the $U(1)$ interaction so they can interact by exchanging photons and the massive $W^{\pm}$ and Z bosons. Quarks carry quantum numbers for weak isospin, hypercharge, and color charge so they partake in the same interactions as the leptons but also interact via the strong interaction through the exchange of gluons.

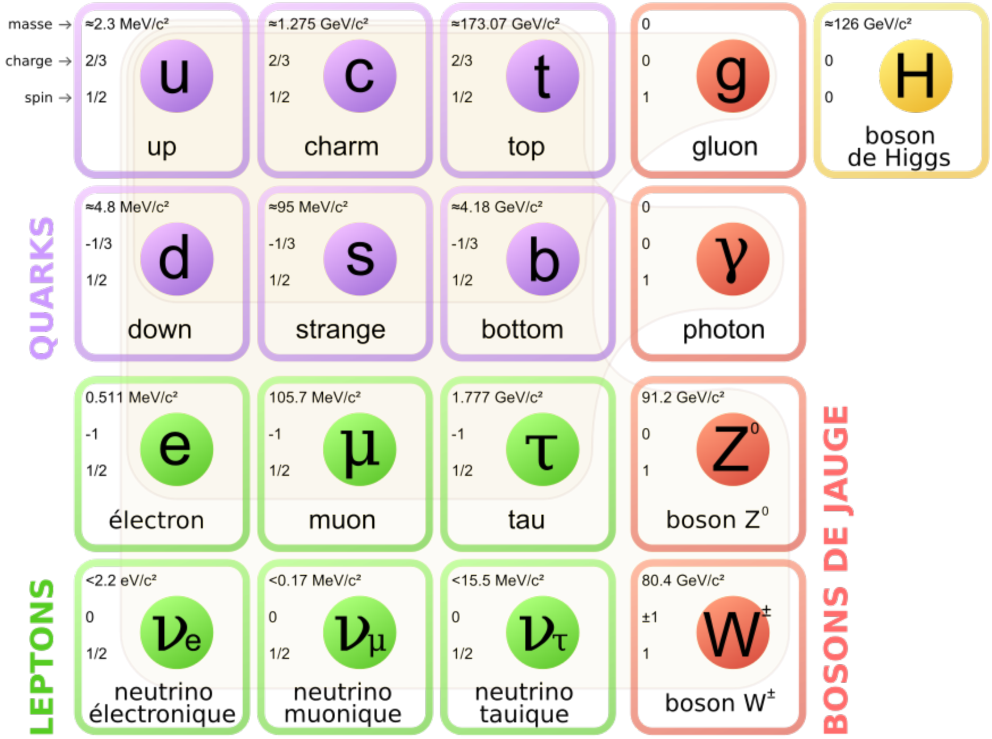

Figure 2.1: Particles of the Standard Model.

The leptons and quarks come in three generations, each with the same quantum numbers but a different mass. While this difference seems slight, the difference can be significant when studying the decay products in high energy experiments. Since the mass of a particle is tied to the energy of the particle, the heavier generations will decay to the lower generations. The mass of the particles can also have other effects. For example muons are basically heavy electrons but, due to the increased mass, they do not interact as strongly with matter. This allows muons to pass through material much more easily than electrons.

In addition to matter that is made up of the particles presented in Figure 2.1, there exists anti-matter that are themselves separate particles. Anti-matter is distinguished from matter by having opposite charge and parity quantum numbers. For example, positive electrons or positrons are anti-electrons. When an anti-particle and a particle interact, they can be be annihilated and converted to energy that then produces new particles. In the same way a particle and anti-particle pair can be produced under certain situations, for example, a photon interacting with the atoms can produce an electron/positron pair. In this thesis, anti-particles are often distinguished by placing a bar over the particle. For example $t\bar{t}$ represents a top quark and an anti-top quark. Other times, the anti-particle is not distinguishable for the particle (e.g. photons) and other times, the anti-particle will just be designated by the sign (i.e. e^+ for positrons).

The latest particle to be discovered and last particle to be predicted by the Standard Model is the Higgs boson that was discovered by both the ATLAS and CMS detectors at the LHC [15, 16]. The Higgs boson is responsible for spontaneously breaking the symmetry of the Standard Model, leading to the weak force mediators and the fermions acquiring mass.

2.1.1 Lagrangians and Groups

In high energy physics experiments, particles are accelerated to high energies and collided or scattered off of each other and the final state particles are measured in a detector. The evolution of a system from one state to another is governed by the Hamiltonian, H, of the system and the amplitude to go from the initial state $|a\rangle$ at time T_i to the final state $|b\rangle$ at time T_f is given by

$$\langle b|e^{-iH(T_f-T_i)}|a\rangle \tag{2.1}$$

In the limit that $T_f - T_i$ goes to infinity, the operator $e^{-iH(T_f-T_i)}$ is called the scattering matrix, S. Hence, the scattering matrix maps the initial state to the final state and the scattering amplitude is given by the matrix element $\langle b|S|a\rangle$. To make predictions about the final states that will be generated by high energy collisions, we need the Hamiltonian of the system.

While we ultimately want the Hamiltonian governing the interaction in high energy collisions, a theory is often specified by its Lagrangian instead and then the Hamiltonian is obtained by performing a Legendre transformation. This is due to the fact that any physical theory should be invariant under spacetime translations and Lorentz transformation. By Noether's theorem, transformations that leave the Lagrangian invariant correspond to conservation laws [17]. The conservation laws associated with spacetime translations and Lorentz transformations are the conservation of four-momentum and angular momentum. By applying simple requirements to the terms constructed of fields used to construct the Lagrangian, both of these symmetries can be guaranteed and these conservation laws will hold. The transformations that leave a system invariant are examples of symmetries and each symmetry can be represented by a group. The group associated with spacetime translation and Lorentz transformations is called the Poincare group. Theories are often constructed by specifying the symmetries of the system and then constructing the Lagrangian from fields that transform according to the group associated with the symmetry.

A group $\mathcal{G}$ is defined as a set of group elements g and an operation that transforms an element into another element of the set. An example would be the set of integers under addition. Adding two integers together yields another integer. This is an abstract concept that does not seem to have much to do with physics. To arrive at something with a physical meaning, we need to choose a representation for the elements of a group. A representation, R, is an operation that assigns each element of a group to an operator $D_R(g)$ that acts on some bases. Typically, the representation is taken to be a matrix. In this case, the basis that the matrices acts on is an n dimensional vector space with elements $\boldsymbol{\phi} = (\phi^1, ..., \phi^n)$ that are transformed by the representation of the group element:

$$\phi^i \to (D_R(g))^i_j \phi^j. \tag{2.2}$$

In this thesis, the Einstein summation convention is used, meaning that repeated indices imply a sum over that index. Further, Greek indices are summed over the four spacetime coordinates while roman indices sum of only the three spatial coordinates. If the group is taken to be $SO(3)$, the group elements can be interpreted as the set of matrices that generate rotations in three dimension space. If we consider very small rotations θ_a close to the identity, Equation 2.2 can be written approximately as

$$R(\theta) \sim 1 + \theta_a T^a_R \tag{2.3}$$

where T^a_R are called the generators of the group. For the case of the $SO(3)$ group, the generators correspond to the commonly seen rotation matrices in three dimensions. If the generators of the group commute, the group is said to be Abelian; otherwise, the group is said to be non-Abelian. The Standard Model and the $SO(3)$ groups are examples of non-Abelian groups.

We can see that the groups of the Standard Model represent symmetries or invariants of the physics of the universe. Since the Standard Model is a local gauge theory, the parameter θ in Equation 2.2 is an arbitrary function of spacetime. The representation of these groups are then used to construct terms that enter the Lagrangian. Once the Lagrangian has been determined, we can then start to make predictions. The next sections discuss the representations and implications of the $SU(3) \otimes SU(2) \otimes U(1)$ local gauge symmetry of the Standard Model.

2.2 Electroweak Interactions and the Higgs Mechanism

The electroweak interaction of the Standard Model is composed of the electromagnetic and weak interactions and is described by the $SU(2) \otimes U(1)$ group. There are four generators associated with the electroweak interaction: three for $SU(2)$ and 1 for $U(1)$. Each generator is associated with a gauge boson that acts as a force mediator for the interaction. For a particle to partake in the associated interaction, it must have a non-zero value for the associated quantum number. For the $SU(2)$ interaction, the quantum number is called weak isospin. For the $U(1)$ interaction, the quantum number is called hypercharge.

The representation of the group is provided by fermion fields that are grouped in a doublet:

$$\Psi = \begin{pmatrix} \Psi_L \\ \Psi_R \end{pmatrix} \tag{2.4}$$

where Ψ_L and Ψ_R represents a field for a left-handed and right-handed field, respectively. The handedness of a particle is related to the spin of the particle. The right and left-handed fermions transform under the $U(1)$ gauge group:

$$\Psi_{\mathrm{L,R}} \rightarrow [1 - ig'Y\beta(x)]\Psi_{\mathrm{L,R}} \tag{2.5}$$

where Y is the group generator, g' is the coupling strength and $\beta(s)$ is an arbitrary function of spacetime and represents the infinitesimal parameter associated with the transformation from the identity as seen in Equation 2.3. On the other hand, only the left-handed fermion field transforms according to the $SU(2)$ gauge group:

$$\Psi_{\mathrm{L}} \rightarrow [1 - igT_i\alpha^i(x)]\Psi_{\mathrm{L}} \tag{2.6}$$

where T_i are the group generators, g is the coupling strength, and $\alpha(x)$ is an arbitrary function of spacetime and is the parameter associated with the infinitesimal transformation from the identity. Since the $SU(2)$ interaction treats particles differently depending on the handedness of the particle, the interaction is referred to as chiral. Neutrinos are predicted by the Standard Model to be only exist as left-handed particles.

The $SU(2) \otimes U(1)$ Lagrangian is given by

$$\mathcal{L}_{\text{EW}} = -\frac{1}{4} A_a^{\mu\nu} A_{\mu\nu}^a - \frac{1}{4} B^{\mu\nu} B_{\mu\nu} + \bar{\Psi} i \gamma^\mu D_\mu \Psi. \tag{2.7}$$

where $A_a^{\mu\nu}$ are the three field strength tensors associated with the $SU(2)$ interaction, $B^{\mu\nu}$ is the field strength tensor associated with the $U(1)$ interaction, and D_μ is the covariant derivative. The covariant is given by

$$D_\mu = \partial_\mu - igT_a A_\mu^a - ig'.\frac{1}{2} Y B_\mu \tag{2.8}$$

where g is the coupling strength for the $SU(2)$ interaction, g' is the coupling strength for the $U(1)$ interaction, T_1 are the generators for the $SU(2)$ interaction, Y is the generator for the $U(1)$ interaction, A_a^μ are the three gauge fields associated with the weak isospin quantum number associated with the $SU(2)$ interaction, B^μ is the gauge field associated with the hypercharge quantum number associated with the $U(1)$ interaction. These weak isospin and hypercharge quantum numbers can be thought of as similar to the familiar electric charge.

Generally, the field strength tensor is given by

$$F_{\mu\nu} = \partial_\mu A_\nu - \partial_\nu A_\mu - ig[A_\mu, A_\nu] \tag{2.9}$$

where A^μ is the gauge field associated with the interaction and g is the coupling strength. When the generators of the group associated with the group do not commute, the extra term in the field strength is non-zero and allows the gauge fields for the interaction to self-interact. The $U(1)$ group is Abelian while the $SU(2)$ group is non-Abelian. As a result of the non-Abelian nature of the $SU(2)$ interaction, the associated gauge bosons can self-interact.

The gauge fields associated with the $SU(2) \otimes U(1)$ symmetry group are massless and therefore cannot correspond to the electroweak force mediators introduced in Section 2.1. Instead, the massive physical gauge bosons that are reconstructed in high energy physics experiments are given by a linear combination of the massless $SU(2) \otimes U(1)$ gauge fields. The mechanism that gives mass to particles and causes the mixing of the $SU(2) \otimes U(1)$ gauge fields is called spontaneous symmetry breaking that occurs due to the Higgs mechanism.

The Higgs mechanism involves introducing a Higgs field and an associated potential to the Standard Model Lagrangian. The Higgs field is a doublet of complex scalar fields:

$$\phi = \begin{pmatrix} \phi^1 \\ \phi^2 \end{pmatrix} \tag{2.10}$$

Terms associated with the Higgs field and a double well potential

$$\mathcal{L}_{\text{Higgs}} = D_\mu \phi^\dagger D^\mu \phi - \frac{1}{2}\lambda^2(|\phi|^2 - \eta^2)^2 \tag{2.11}$$

where D_μ is the covariant derivative given by Equation 2.8 are then added to the Lagrangian given in Equation 2.7. The potential has a continuous set of minimum given by the condition $|\phi|^2 = \eta^2$. The expectation value for the potential will then be $\langle \phi \rangle = \eta$. Due to the non-zero expectation value, the system will chose one of the minima and the symmetry of the electroweak interaction is spontaneously broken. By making a convenient choice for the arbitrary phase of the Higgs field and expanding the Higgs field about the minima, the Higgs field can be written as

$$\phi = \begin{pmatrix} 0 \\ \eta + \frac{h}{\sqrt{2}} \end{pmatrix} \tag{2.12}$$

where h is a real scalar field that can then be interpreted as a displacement from the minima. Using Equation 2.12, to compute $D_\mu \phi^\dagger D^\mu \phi$ results in three linear combinations of the $SU(2) \otimes U(1)$ gauge fields that have mass terms in the electroweak Lagrangian and one linear combination that does not have an associated mass term. The linear combinations of the $SU(2) \otimes U(1)$ gauge fields are given by

$$\gamma = B \cos\theta_w + A_3 \sin\theta_w \tag{2.13}$$

$$Z = B \cos\theta_w + A_3 \cos\theta_w \tag{2.14}$$

$$W^\pm = \frac{1}{\sqrt{2}}(A_1 \mp iA_2) \tag{2.15}$$

where θ_W, is referred to as the weak mixing angle or the Weinberg angle and must be determined through experimental measurements, γ corresponds to the massless photon, Z corresponds to the massive neutral Z boson, and $W^\pm$ corresponds to the massive charged $W^\pm$ bosons. The $W^\pm$ and Z bosons can be identified as the mediators of the weak interaction and the γ is can be interpreted as the force mediator for the electromagnetic interaction.

The fermions of the Standard Model also gain mass through an interaction, called the Yukawa interaction, to gain mass. The mass terms for the fermions that are added to the Standard Model Lagrangian are given by:

$$\mathcal{L}_{\text{Yukawa}} = \frac{m_{f\sqrt{2}}}{\nu}[\bar{\mathbf{\Psi}}_R(\phi^\dagger \mathbf{\Psi}_L) + (\bar{\mathbf{\Psi}}_L \phi^\dagger)\mathbf{\Psi}_R] \tag{2.16}$$

where m_f is the mass of the fermion that must be determined experimentally. The Standard Model predicts that all neutrinos are left-handed. Since the Yukawa interaction is between left-handed and -right-handed fermion fields, neutrinos are predicted to be massless by the Standard Model.

2.3 Quantum Chromodynamics (QCD)

The strong interaction or quantum chromodynamics (QCD) is described by the non-Abelian $SU(3)$ symmetry group. There are eight generators associated with the $SU(3)$ group and each generator is associated with a gluon, the force mediator for the strong interaction. Due to the non-Abelian structure of the strong interaction, gluons can self-interact just like the $W^{\pm}$ bosons of the weak interaction. The fields that transform according to the $SU(3)$ symmetry group are called quarks. As mentioned in Section 2.1, there are three generations of quarks and each generation contains two flavors of quarks. Quarks are the only particle to partake in the strong interaction and carry a quantum number called color or color charge. The colors can be either red, green, blue, anti-red, anti-green, or anti-blue. Quarks can only exist in a colorless state. Since each quark only carries one color, quarks are only found in bound states called hadrons. Mesons are formed by two quarks and baryons, like protons, are bound states of three quarks.

The QCD Lagrangian is given by

$$\mathcal{L}_{\text{QCD}} = -\frac{1}{4}F^a_{\mu\nu}F^{\mu\nu}_a + \bar{q}_i(i\gamma^\mu(D_\mu) - m_i)q_i \tag{2.17}$$

where the i^{th} quark field is given by q_i and the associated mass of the quark is given by m_i. The covariant derivative appearing in Equation 2.17 is given by

$$D_\mu = \partial_\mu - igA^a_\mu T^a \tag{2.18}$$

where g is the strong coupling constant, T^a are the generators of the $SU(3)$ interaction and G^a are the gauge fields associated with the strong interaction.

Unlike photons and the weak interaction force mediators, the strength of the strong force increases with distance. As the distance increases, the potential energy will eventually be high enough that it is energetically more favorable for another quark/anti-quark pair to be

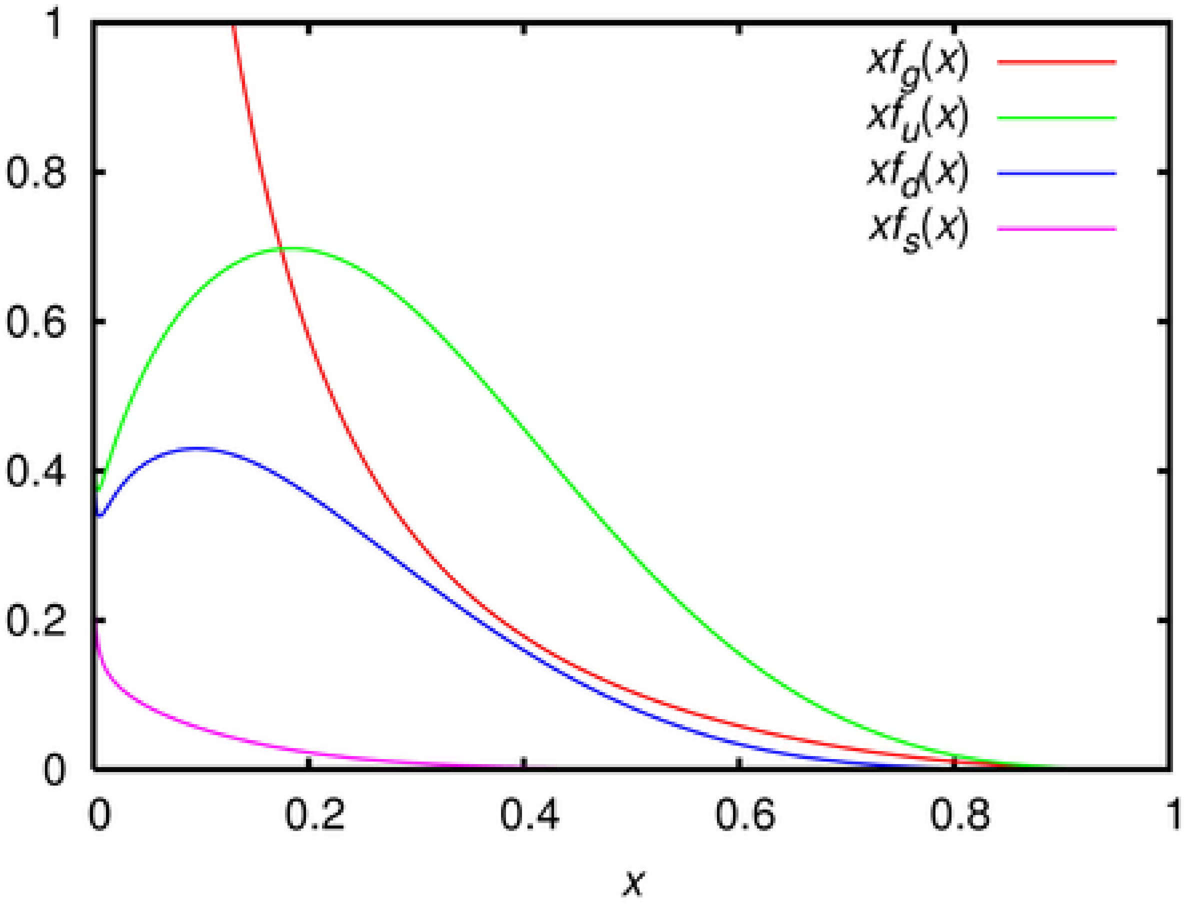

Figure 2.2: CTEQ6 parton distribution function. Each curve represents a probability distribution for the fraction of the momentum for each flavor of quark considered: u, d, s, c (4FS)

produced from the vacuum, forming additional hadrons. If the energy imparted to a pair of quarks is great enough, the number of quarks created in this manner can form a jet of strongly interacting particle.

2.4 Parton Distribution Functions (PDF)

The data analyzed in this thesis is generated by measuring the final state particles using the ATLAS detector produced by colliding two protons together at high energy. Protons are bound states of two up quarks and a down quark, called valence quarks. When a collision between two protons occurs, the quarks or gluons in the protons interact. The resulting final state depends on the flavor of the quarks or gluons in the interaction as well as the momentum transfer Q^2. The quarks available to be part of the interaction include the two up and down valence quarks and quarks that result from QCD radiation called sea quarks. This means that the quarks that can enter into the interaction is not limited to the up and down quarks and gluons present in the proton but also the other quark flavors. In order to provide theoretical predictions on what final states will arise from the collision of two protons, the probability that a quark of a given flavor will interact with momentum transfer Q^2 is needed. This is provided by the parton distribution function (PDF). An example of the CTEQ6 PDF set is given in Figure 2.2. Note that the PDF displayed only provides information of the four lightest quark flavors. This is referred to as the four flavor scheme. A process that requires a bottom quark in the proton can still be modeled in this situation by assuming that a gluon is involved with the interaction and produces a $b\bar{b}$ pair and one of the bottom quarks is involved in the interaction. PDF sets that consider the bottom quark as well as the four lightest quark flavors use the five flavor scheme.

2.5 $W^{\pm}W^{\mp}\gamma$ prediction

Measurements of triboson processes, including $W^{\pm}W^{\mp}\gamma$, provide an essential test of the Standard Model of particle physics. In the Standard Model, the electroweak interaction is based on the non-Abelian $SU(2) \otimes U(1)$ gauge group and provides precise predictions for the interactions between the electroweak force carriers (the $W^{\pm}$ and Z bosons and the γ) with each other and with themselves. Studies of the production of triboson processes provides a window into this non-Abelian structure of the Standard Model. Any significant deviation from the Standard Model prediction could provide evidence of new physics or physics beyond the Standard Model (BSM). Any deviations from the Standard Model can also be parameterized in the framework of an effective field theory (EFT). Limits can then be placed on the anomalous couplings.

Examples of the $W^{\pm}W^{\mp}\gamma$ process is illustrated in Figure 2.3. Additional Feynman diagrams for the $W^{\pm}W^{\mp}\gamma$ process are included in Appendix B. From the example Feynman diagrams, we see that the $W^{\pm}W^{\mp}\gamma$ process has contributions from quartic gauge couplings (first diagram) as well as triple gauge couplings (second diagram). This analysis focuses on quartic gauge couplings. The 14 operators associated with anomalous quartic gauge couplings (aQGC) that the $W^{\pm}W^{\mp}\gamma$ process is sensitive to are indicated in Figure 2.1 in the columns for $WW\gamma Z$ and $WW\gamma\gamma$. These correspond to the quartic gauge coupling in first diagram in Figure 2.3. The limit setting procedure and expected results for the limits on the aQGC parameters are beyond the scope of this thesis and will be included in another thesis.

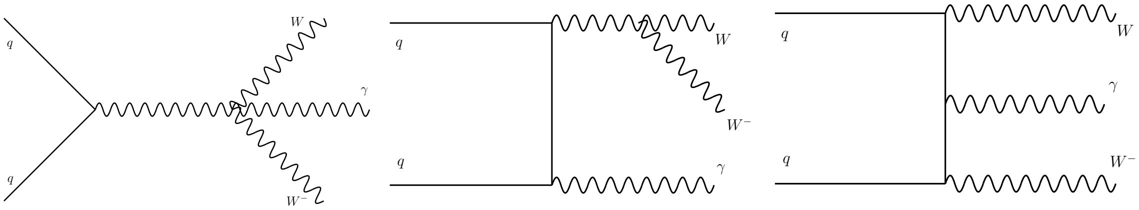

Figure 2.3: Feynman diagrams for the ISR $W^{\pm}W^{\mp}\gamma$ process. (Left) Feynman diagram depicting the production of $W^{\pm}W^{\mp}\gamma$ involving the TGC, (Middle) Feynman diagram depicting the production of $W^{\pm}W^{\mp}\gamma$ involving the QGC, and (Right) Feynman diagram depicting the production of $W^{\pm}W^{\mp}\gamma$ for the fermion-mediated process.

Table 2.1: Dimension-8 operators $\mathcal{O}_j$, separated into Mixed (M), Longitudinal(S) and Transverse (T)

	$WWWW$	$WWZZ$	$WW\gamma Z$	$WW\gamma\gamma$	$ZZZZ$	$ZZZ\gamma$	$ZZ\gamma\gamma$	$Z\gamma\gamma\gamma$	$\gamma\gamma\gamma\gamma$
$\mathcal{O}_{S,0}$,$\mathcal{O}_{S,1}$	x	x			x				
$\mathcal{O}_{M,0}$,$\mathcal{O}_{M,1}$,$\mathcal{O}_{M,6}$,$\mathcal{O}_{M,7}$	x	x	x	x	x	x	x		
$\mathcal{O}_{M,2}$,$\mathcal{O}_{M,3}$,$\mathcal{O}_{M,4}$,$\mathcal{O}_{M,5}$		x	x	x	x	x	x		
$\mathcal{O}_{T,0}$,$\mathcal{O}_{T,1}$,$\mathcal{O}_{T,2}$	x	x	x	x	x	x	x	x	x
$\mathcal{O}_{T,5}$,$\mathcal{O}_{T,6}$,$\mathcal{O}_{T,7}$		x	x	x	x	x	x	x	x
$\mathcal{O}_{T,8}$,$\mathcal{O}_{T,9}$					x	x	x	x	x

A previous search for $W^{\pm}W^{\mp}\gamma$ was performed at ATLAS using 20.3 fb^{-1} of data collected by the ATLAS detector using proton-proton collision collided at a center of mass energy ($\sqrt{s}$) of 8TeV and limits were placed on the $W^{\pm}W^{\mp}\gamma/W^{\pm}Z\gamma$ cross section as well as aQGC parameters [18].

Chapter 3

The ATLAS Detector at the LHC

3.1 LHC

Located approximately 100 m below the ground on the border of France and Switzerland near Geneva, CERN (Conseil Europeen pour la Recherche Nucleaire) operates the LHC (Large Hadron Collider), a circular hadron collider and the world's most powerful particle accelerator [14]. At points along the 27 km circumference of the ring housing the LHC, protons (and, for special runs, lead ions) are collided at interaction points that are surrounded by detectors that collect the flurry of particles resulting from the high energy collisions so that the events can be reconstructed, studied, and hopefully understood. The data used in the analysis presented in this thesis represents $139\,\mathrm{fb}^{-1}$ of proton-proton collisions at a center-of-mass energy ($\sqrt{s}$) of $13\,\mathrm{TeV}$ collected at one such detector: the ATLAS (A Toroidal LHC ApparatuS) detector [19]. Other detectors located at other interaction points of the LHC include: CMS (Compact Muon Solenoid) [20], ALICE (A Large Ion Collider Experiment) [21], and LHCb (Large Hadron Collider Beauty) [22]. The layout of the CERN complex along with the LHC and the different associated experiments can be seen in Figure 3.1.

The LHC uses electromagnetic fields to steer and accelerate proton beams in opposite directions around the LHC ring. Protons are injected into the LHC ring after having been

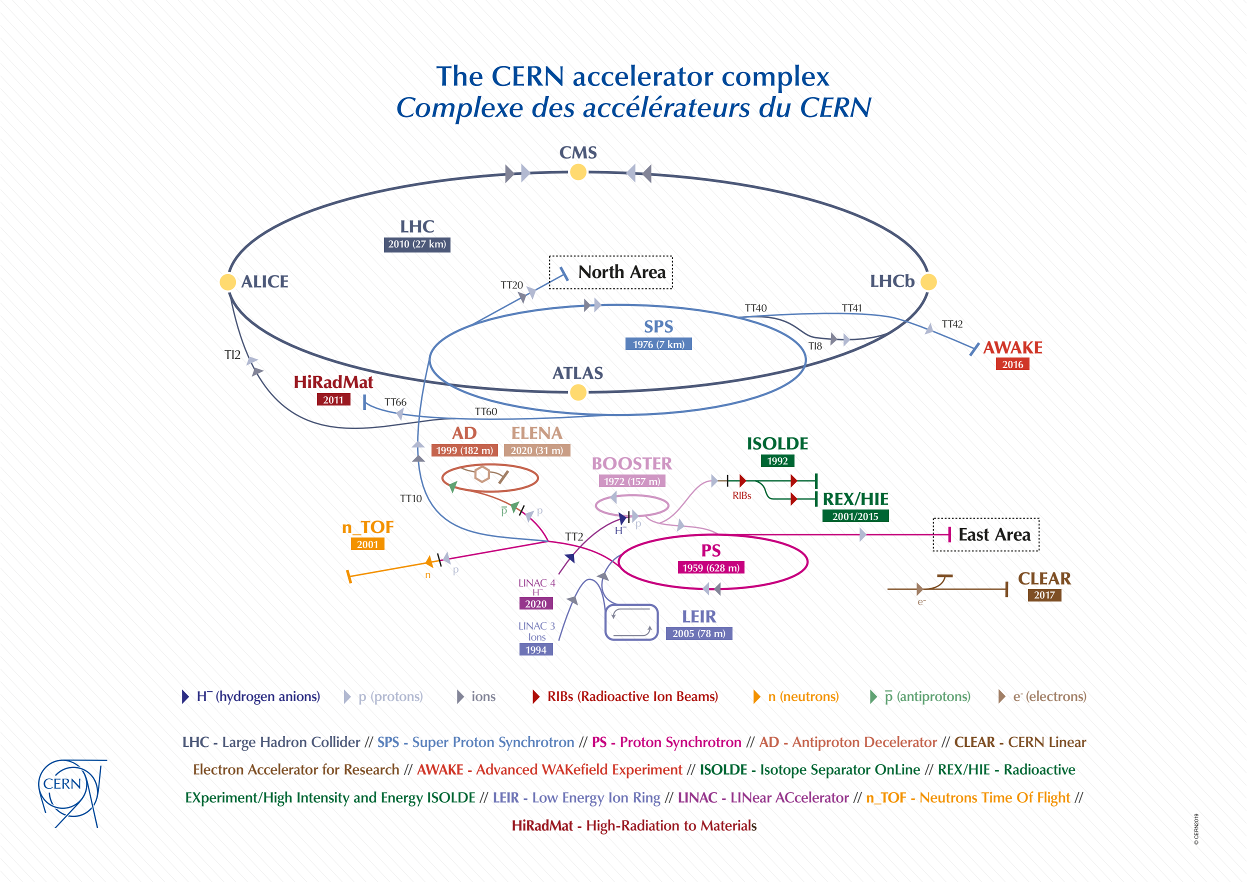

Figure 3.1: The CERN complex located on the border of the France and Switzerland, near Geneva. The LHC and the many experiments operated by CERN are indicated. Of particular note is the ATLAS detector, which was used to collect the data used to perform the analysis described in this thesis.

accelerated to an initial energy of 450 GeV by a series of other accelerators: LINAC2, PS Booster, PS, and the SPS. To keep the proton beams circulating around the LHC, superconducting dipole magnets steer the proton beams using approximately 8 T magnetic fields. Superconducting radio frequency cavities operated at a frequency of 400 MHz accelerates proton beams in opposite directions around the LHC until they reach a final energy of approximately 6.5 TeV [23]. To limit the number of collisions between the protons in the circulating beams and air particles, the beams are kept within a vacuum tube kept at a pressure of approximately 10^{-10} mbar. Since the vacuum is not perfect, some stray collisions still occur.

After reaching the target energy, the proton beams are focused using superconducting quadropole magnets and collided at the LHC interaction points. Each proton beam contains 2808 equally spaced bunches, or groups or protons, resulting in collisions every 25 ns (50 ns for the data taken in 2015). The expected number of collisions produced per unit time is given by:

$$\frac{dN}{dt} = \mathcal{L}\sigma_{\text{total}} \tag{3.1}$$

where the instantaneous luminosity ($\mathcal{L}$) is measured in units of the number of events per unit area per unit time and the hard scattering cross section (σ), which can be thought of as the probability for a hard scattering event to occur, is measured in the units of area. Integrating Equation 3.1 over the operation time of the ATLAS detector at a particular center of mass energy quantifies the amount of data collected

$$N_{\text{events}} = L\sigma_{\text{total}} \tag{3.2}$$

in terms of the total number of hard-scattering events (collisions with a large momentum transfer) produced and the total or integrated luminosity L. The standard unit for L and σ is the barn ($\text{b} = 10^{-24}\text{cm}^2$) and the inverse barn ($\text{b}^{-1}$), respectively. Due to the small scale that the experiments at the LHC probe, the femtobarn (fb) and inverse femtobarn (fb^{-1}) are more commonly used. The total integrated luminosity collected by the ATLAS detector between 2015 and 2018 is measured using the LUCID-2 ATLAS sub-detector [24, 25] and found to be $139\,\text{fb}^{-1} \pm 1.7\%$ [26]. Replacing the total hard scattering cross section with the cross section of a particular process, for example $W^{\pm}W^{\mp}\gamma$, in Equation 3.2 yields the total expected number of events for that process

$$N_{W^{\pm}W^{\mp}\gamma} = L\sigma_{W^{\pm}W^{\mp}\gamma}. \tag{3.3}$$

produced during the data taking period corresponding to L. From Equation 3.2 and Equation 3.3, it is clear that, for rare processes (small expected cross sections), a large (and accurately measured) luminosity or a long data taking period is required to study the process. In addition to hard-scattering interactions that can produce events of interest to this thesis, many soft-scattering interactions where the total momentum transfer is low often occur in the same bunch crossing. These additional interactions are called pile-up and can interfere with the collision of interest.

3.2 ATLAS

The data used in this thesis was collected between 2015 and 2018 using the ATLAS detector, located at one of the four main interaction points of the LHC. The ATLAS detector [13], illustrated in Figure 3.2, is a cylindrical detector measuring 44 m long and 25 m high and composed of three detector systems, each with there own purpose, technology, and sub-detectors/components. Each detector component is a set of sensors arranged in cylinder (barrel and endcap) that encloses the previous detector component. The sub-detectors include the inner detector that uses a dense array of sensors to identify the origin (primary vertex) of an event of interest, identifying locations for additional collisions (secondary vertices) and measure the momentum of the particles produced in the collision of interest. Surrounding the inner detector is a solenoid magnet that produces a 2 T magnetic field that bends the trajectories of charged particles as they traverse the inner detector, allowing their momentum and charge to be measured. The middle layer of the ATLAS detector contains the electromagnetic and hadronic calorimeters. The calorimeters measure the energy of the particles that leave the inner detector and help separate strongly interacting particles (pions, etc.) from electrons and photons. Surrounding the calorimeters is a combination of the muon spectrometer and 3 superconducting toroid magnets: one barrel and two endcap magnets. Since muons interact more weakly than other particles (other than neutrinos), these particles often leave the calorimeter before being completely absorbed and pass through the muon spectrometer and toroid magnet system. The toroid magnets produce a strong magnetic field that bends the trajectories of muons, complementing the information of the momentum and charge of muons provided by the inner detector and colorimeters. Supporting the operation of the ATLAS detector are many off-detector services that include monitoring, cooling, power, triggering, data readout and more. Only with all of these components working properly can data needed to probe interesting physics be collected.

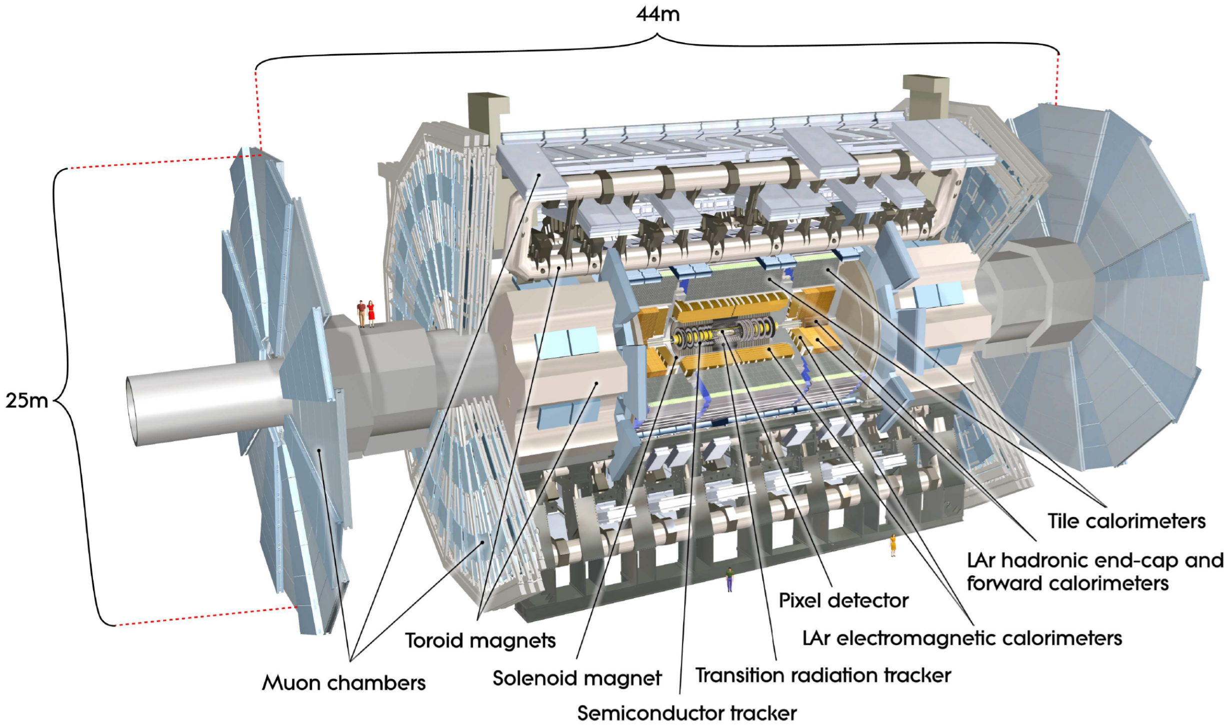

Figure 3.2: The ATLAS detector. The three main sections of the ATLAS detector are the inner detector, the calorimeter, and the muon spectrometer. Additional details about each sub-detector are given in the text.

3.2.1 Detector coordinate system and related quantities

The ATLAS detector used a right handed coordinate system illustrated in Figure 3.3. The origin is taken to be at the center of the detector and the expected origin for events entering the detector. The z-axis lies along the beam direction, the x-axis points towards the center of the LHC, and the y-axis points up. The azimuthal angle (ϕ) is measured from the positive x-axis around the z-axis. Since the ATLAS detector is azimuthally symmetric, distributions of ϕ are expected to be flat but still useful for describing the distance between particles. The polar angle (θ) is measured from the positive z-axis but is rarely used to characterize the properties of a particle. Instead, the pseudorapidity

$$\eta = -\ln \tan\left(\frac{\theta}{2}\right) \tag{3.4}$$

or, for massive particles, rapidity

$$y = \frac{1}{2}\ln\left(\frac{E+p_z}{E-p_z}\right) \tag{3.5}$$

is used since particles being studied are relativistic and these quantities are invariant under Lorentz transformations, where θ is not. The relationship between η and θ is illustrated in Figure 3.4. The ATLAS detector is forward/backward symmetric so distributions of η are expected to be symmetric for $\eta > 0$ and $\eta < 0$ so the absolute value is often used instead. The distance between particles is given by

$$\Delta R = \sqrt{\Delta\phi^2 + \Delta\eta^2} \tag{3.6}$$

As mentioned in Section 2.4, the proton is made of three quarks, each quark carrying a fraction of the energy imparted to the proton as a whole. For this reason, the component of momentum in the z-direction is not known but the momentum in the transverse plane (x-y plane) is approximately 0 before the collision. For this reason, quantities used to define particles momentum and direction are often specified in the the transverse plane. For example, the transverse momentum $\left(p_{\mathrm{T}} = \sqrt{p_x^2 + p_y^2}\right)$. Due to the conservation of momentum, the total momentum in the transverse plane is expected to be zero. Any momentum imbalance (deviation from 0), referred to as ”missing transverse energy”, ($E_{\mathrm{T}}^{\mathrm{miss}}$) is associated with neutrinos that escape without interacting with the detector. The following sections will describe the components of the ATLAS detector that allow experiments to measure the coordinates and variables mentioned in this section.

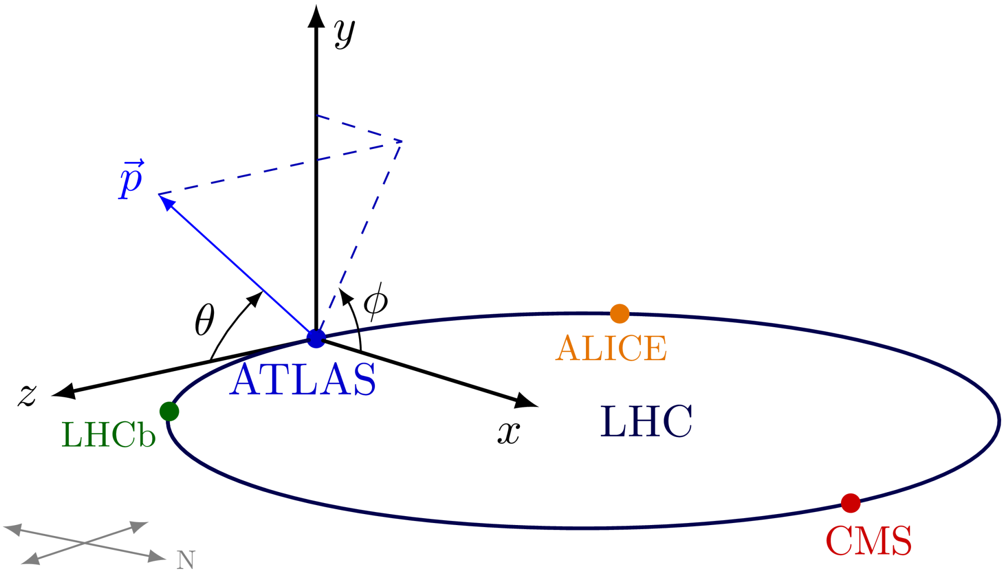

Figure 3.3: Coordinate system used to describe the ATLAS detector.

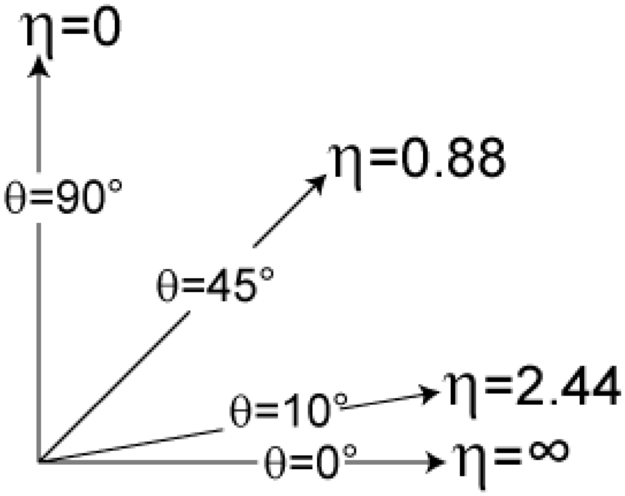

Figure 3.4: relationship between the polar angle, θ, and pseudorapidity

3.2.2 Inner detector

The inner detector (ID) [19] occupies a cylindrical volume centered on the interaction point (IP) that is enclosed by a solenoid magnet that immerses the ID in a 2 T magnetic field. Within this volume are three sub-detectors: the silicon pixel detector, the SCT (silicon strip tracker), and the TRT (transition radiation tracker). These sub-detectors are sensitive to charged particles and, together, provide measurements within $|\eta| < 2.5$. Each detector is composed of a barrel component illustrated in Figure 3.5 and an endcap component illustrated in Figure 3.6. The high density of silicon pixels and silicon strips within the inner detector provide highly granular information on the path charged particles follow through the inner detector and provide information on the origin of the event of interest (primary vertex) and the origin of any additional interactions (pile-up) or subsequent decays (secondary vertices) that might occur at the same time. The coordinates of the reconstructed primary vertex are specified using the longitudinal impact parameter ($Z_0 \sin\theta$) and the transverse impact parameter (d_0). The TRT provides a high number of 1D measurements that enhance the tracking capabilities (momentum measurement) provided by the silicon detectors. The magnetic field bends the trajectory of charged particles, allowing the charge and momentum to be determined. The remainder of this section describes the detector technology employed in each sub-detector.

Pixel detector

The pixel detector [27] is the detector nearest the interaction point. The high resolution and high granularity information provided by the pixel detector allows for precision tracking and the determination of the primary vertex. The pixel detector is composed of 4 layers of sensors (the innermost layer is referred to the insertable b-layer (IBL)) [28, 29] arranged in concentric cylinders centered on the interaction point. Typically, each layer provides one 3D point measurement of the position of a charged particle that traverses the range covered by the pixel detector. The barrel component of the pixel detector covers the range within $|\eta| < 1.4$ and the endcap extends this to $|\eta| < 2.5$. Each layer is composed of densely placed, high resolution semi-conductor silicon sensors. Each sensor is arranged in pixels with dimensions: $50\,\mu\text{m}$ (R-ϕ plane) $\times$ $250\,\mu\text{m}$ (z direction) for the IBL and $50\,\mu\text{m}$ (R-ϕ plane) $\times$ $40\,\mu\text{m}$ (z direction) for the remaining three layers. A voltage is applied across the sensor,

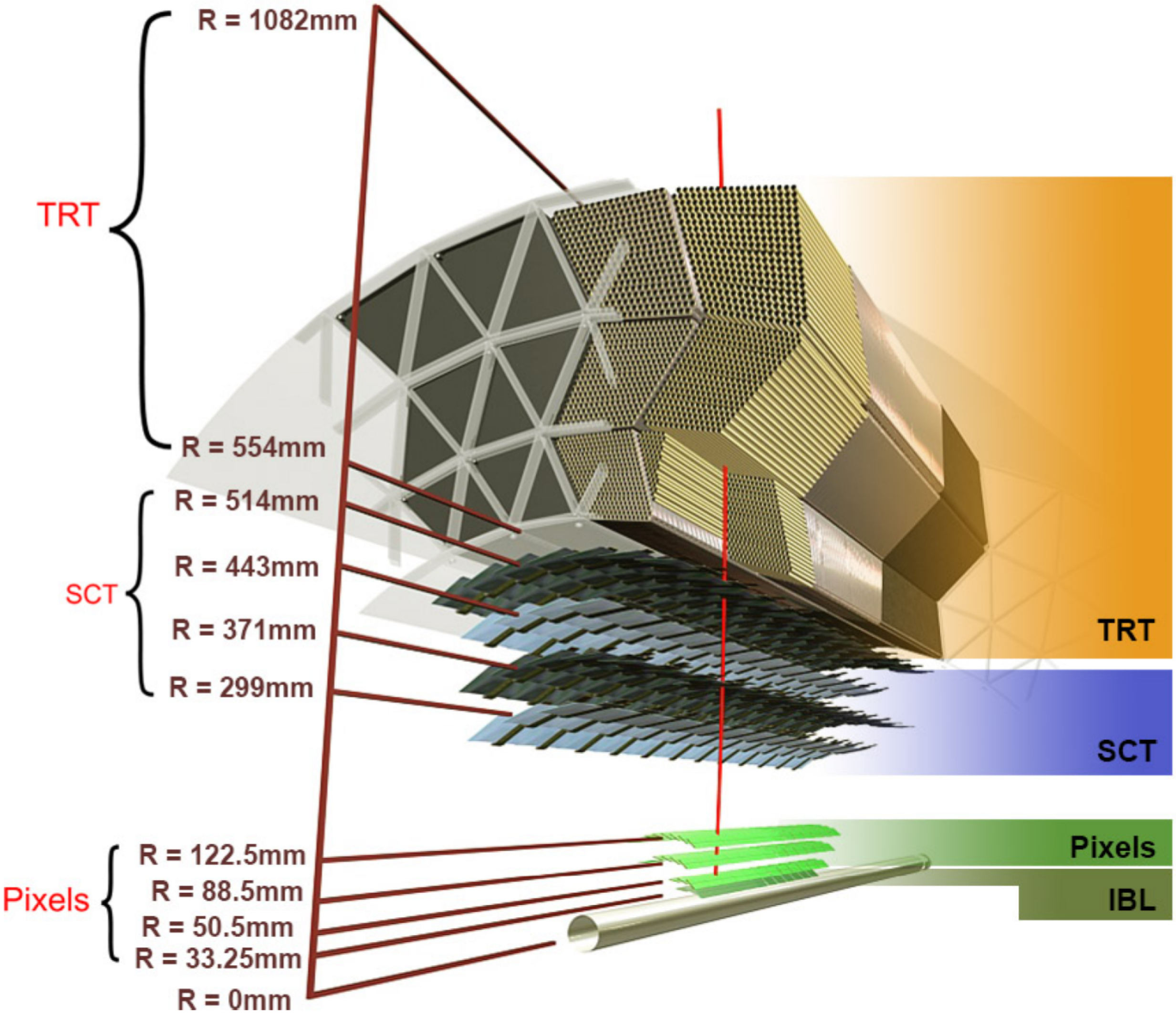

Figure 3.5: Barrel region of the ATLAS inner detector

producing a charge depletion region in the material. When a charged particle traverses the charge-depletion region, charge is deposited and the material becomes ionized. The deposited charge is amplified by the voltage applied across the sensor and pushed towards the readout component.

Silicon strip tracker (SCT)

Surrounding the silicon pixel detector [30] is the silicon strip detector (SCT). The sensors in the SCT are similar to the sensors in the pixel detector but are not placed as densely and

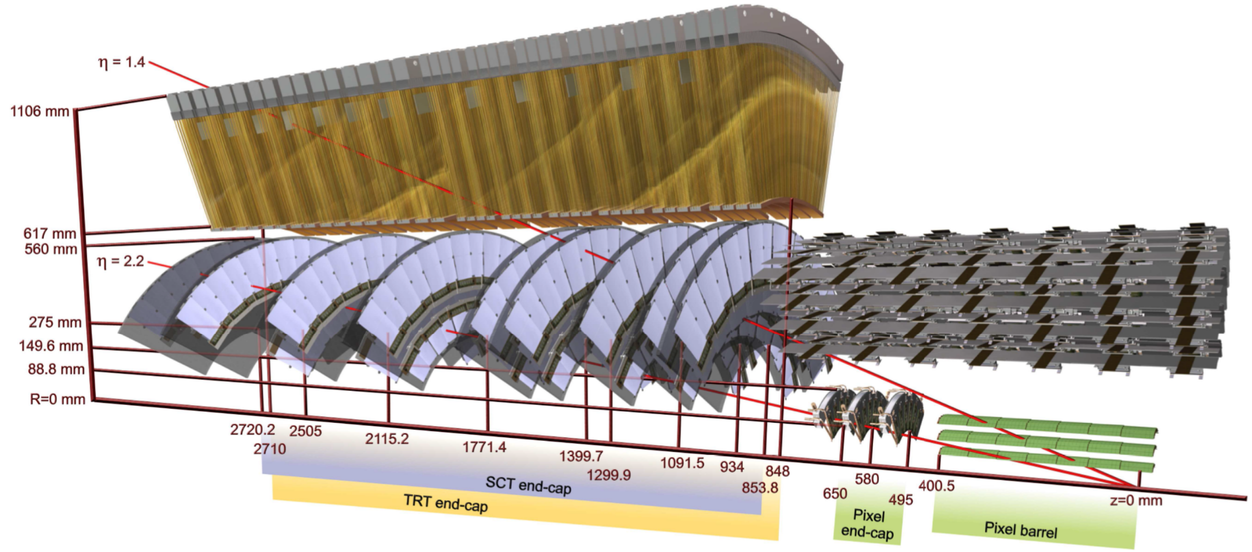

Figure 3.6: Endcap region of the ATLAS inner detector.

the sensors are composed of strips rather than pixels. The width of the strips are 80 µm. To provide a measurement of the position of charged particles that traverse the SCT, each strip sensor is paired with another strip sensor placed at an angle of 40 mrad relative to the paired sensor. There are four paired-layers of sensors in the barrel and nine paired-layers in the endcap. The SCT provides measurements of charged particles traversing the SCT in the range $|\eta| < 2.5$.

Transition radiation tracker (TRT)

The transition radiation tracker (TRT) [31, 32, 33] is composed of a large number of straw tubes filled with ionizable gas. In the barrel region, the straw tubes are parallel to the beam pipe; in the endcaps, the straw tubes are perpendicular. Each tube is composed of an gold-plated tungsten wire surrounded by a thin tube 4 mm in diameter. The gas in each tube is composed primarily of Xenon and a smaller amount of carbon dioxide. When a charged particle traverses the TRT, the charged particle ionizes the gas in the straw tubes. The deposited charge is amplified by a bias applied between the central wire and the tube, causing an "avalanche" of charge to flow towards the wire in the center of the tube. The time required for the charge to reach the central wire is used to infer how close the charged particle came to the central wire. The TRT typically provides 36 position measurements in the R-ϕ plane for a charged particle traversing the TRT within $|\eta| < 2.0$. Due to the high number of position measurements, the TRT improves the tracking capability (momentum resolution) provided by the other detectors in the inner detector.

3.2.3 Calorimeters

The calorimeter system [34] used in the ATLAS detector illustrated in Figure 3.7 occupies the detector volume between the solenoid magnet enveloping the inner detector and the muon spectrometer. The calorimeter system is intended to completely absorb all of the energy of all particles produced in collisions expect for weakly interacting particles such as muons and neutrinos before they can leave the calorimeter system. By absorbing all of the energy before particles can exit the calorimeter system, the total energy of the event can be measured in the transverse plan, allowing conservation of momentum to be employed to calculate the "missing transverse energy." The calorimeter system provides energy measurements as a function of η and ϕ withing $|\eta| < 4.9$. There are two separate sub-detectors comprising the calorimeter system: the electromagnetic (EM) calorimeter and the hadronic calorimeter. Both types of calorimeter are sampling calorimeters. Sampling calorimeters use alternating layers of an absorbing material and an active material. The absorbing layers interact with the particle, removing a fraction of the energy and inducing a shower of secondary particles in the layer of the active material. A fraction of the energy contained in the shower of electromagnetic radiation is measured (sampled) using the material in the active layer. Combining the information from each layer in the calorimeter, the energy of the incident particle can be inferred. The EM calorimeter is built of alternating layers of an absorbing material optimized to absorb the energy of particles that interact via electromagnetic interactions and layers of an active material, in this case , liquid argon. The hadronic calorimeter is built of alternating layers of absorbing material specialized in interacting with particles that interact via the strong interaction and layers of an absorbing material (either liquid argon or scintillating tiles depending on whether the calorimeter is in the forward region (endcap) or the barrel region.

Complementing the EM calorimeter and the hadronic calorimeter are the liquid argon forward calorimeter and a liquid argon pre-sampler. The forward calorimeter covers the range $3.1 < |\eta| < 4.9$ and extends the pseudorapidity coverage of both the EM calorimeter and the hadronic calorimeter to $|\eta|$ of 4.9. The placement of the forward calorimeters is given in Figure 3.8. The electromagnetic pre-sampler covers the range $|\eta| < 1.8$ and provides an energy measurement that compensates for energy loss due to material in front of the EM calorimeter.

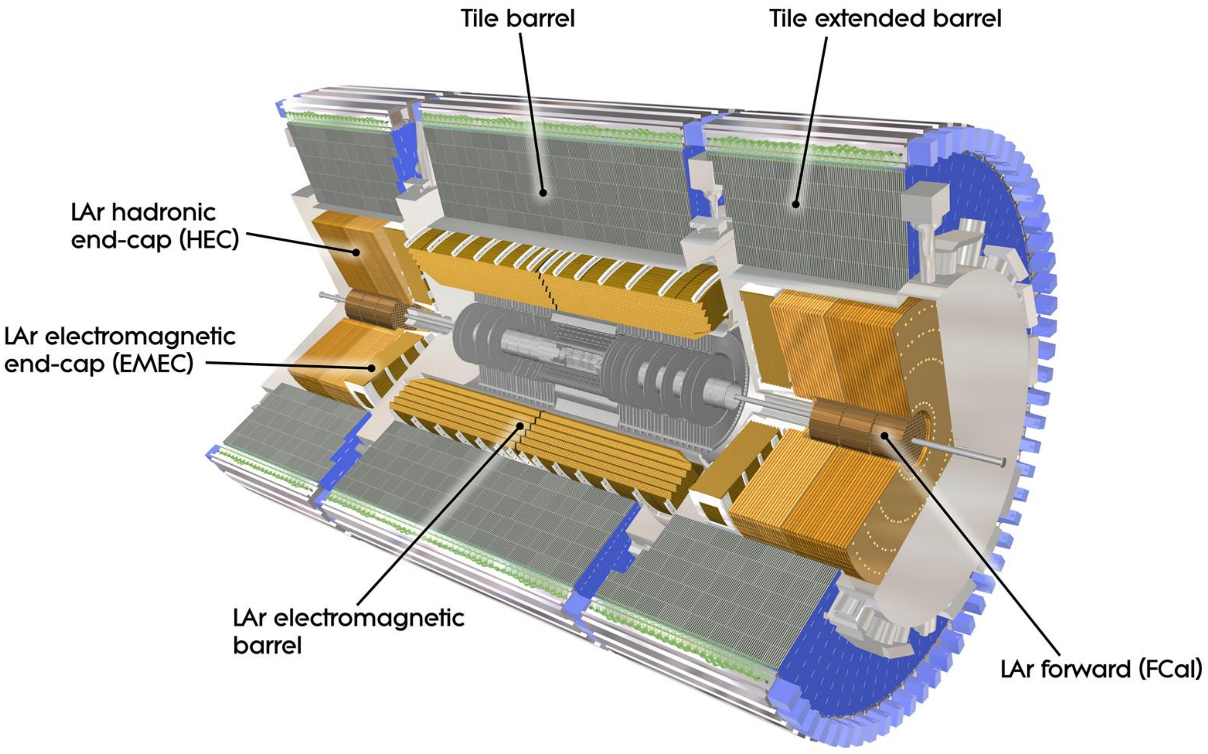

Figure 3.7: The electromagnetic and hadronic calorimeters of the ATLAS detector.

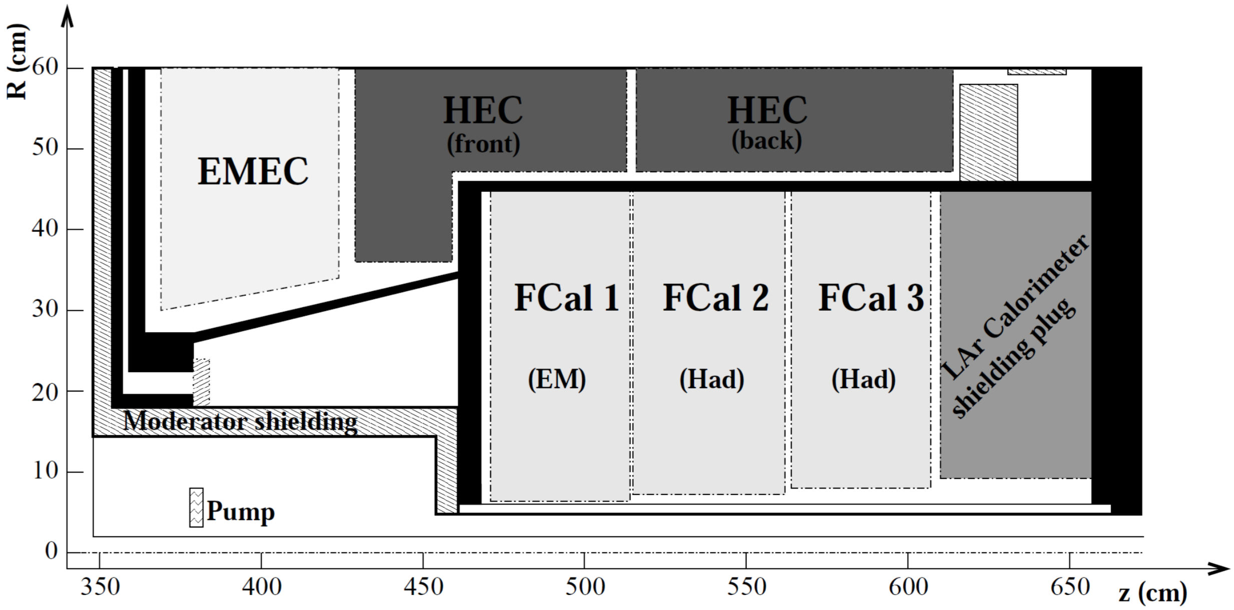

Figure 3.8: The forward calorimeters and electromagnetic and hadronic endcap calorimeters of the ATLAS detector.

Electromagnetic calorimeter

The EM calorimeter [35, 36] is the calorimeter system closest to the interaction point and provides energy and position measurements within the range $|\eta| < 3.2$. There are barrel, referred to as the liquid argon electromagnetic calorimeter barrel (LAr EM calorimeter), and endcap, referred to as the liquid argon electromagnetic endcap (EMAC), components. These will be referred to as the EM calorimeter in this thesis. The primary purpose of the EM calorimeter is to measure the energy of electrons and photons. An important parameter describing the EM calorimeter is interaction length. Interaction length is the distance that a particle must traverse through a material for the particles energy to be reduced by a factor of 1/e. Since electrons have a shorter interaction length than hadrons, the EM calorimeter is placed closer to the interaction point than the hadronic calorimeter. Electrons and photons that interact with the lead absorbing material induce a shower of electromagnetic radiation (secondary particles) that ionize the liquid argon that makes up the active material. The ions are collected with the help of an electric field, becoming a current in the readout electronics.

The EM calorimeter is separated into angular segments of 0.003×0.025 in the η-ϕ in the barrel region and decreasing granularity as the distance from the interaction point increases to 0.1 × 0.1 in the furthest layers of the endcap. In this way, detailed positional information that can be matched to tracks in the inner detector are made available in the early layers and the final layers can work to contain residual energy of incident electrons or photons. A typical section of the EM calorimeter is illustrated in Figure 3.9. The accordion shape of the EM calorimeter allows for multiple position measurements to be made at different depths in the same segment. (3 within the region $|\eta| < 2.5$ and 2 in the region $2.5 < |\eta| < 3.2$

The region within $1.36 < |\eta| < 1.52$, where the barrel and endcap components of the EM calorimeter meet, is referred to as the "crack region." Electrons and photons reconstructed in this region are often rejected since the performance of the EM calorimeter is greatly degraded in this region.

Hadronic calorimeter

Enveloping the EM calorimeter is the hadronic calorimeter [37, 38]. In this thesis the different components of the hadronic calorimeter illustrated in Figure 3.7 will be referred to collectively as the hadronic calorimeter unless otherwise stated. Different technology is employed in the barrel and endcap hadronic calorimeters. In the barrel region (and extended barrel) the hadronic calorimeter uses steel as the absorbing material and scintillating tiles for the active material. In the endcap component of the hadronic calorimeter, the absorbing material is copper and the the active material is liquid argon. Particles that interact strongly with the absorbing material induce showers of secondary particles in the scintillating tiles that are readout. Information from these layers are combined and used to reconstruct showers of strongly interacting particles consistent with quarks or gluons. The hadronic calorimeter provides energy measurements within $|\eta| < 3.2$. The barrel component covers the range $|\eta| < 1.7$ and the endcap extends this to cover the range $1.7 < |\eta| < 3.2$. The hadronic calorimeter in the barrel region contains three layers that are separated into segments ranging from 0.1 × 0.1 in η, ϕ in the first (inner-most) layer to 0.2 × 0.2 in the third (outer-most)

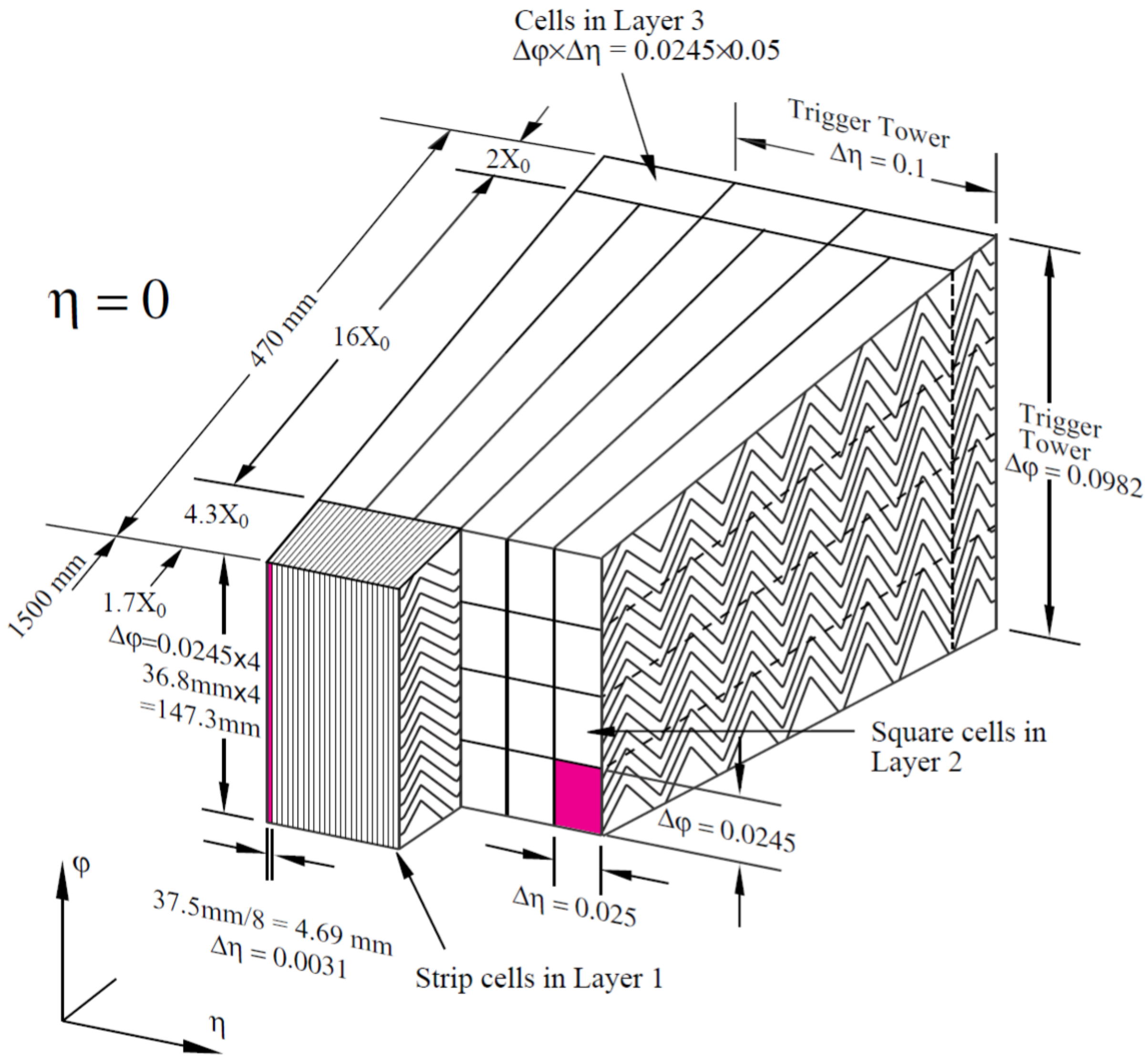

Figure 3.9: A typical segment of the electromagnetic calorimeter of the ATLAS detector.

layer.

3.2.4 Muon system

The muon system [39, 40] illustrated in Figure 3.10 is the final layer of the ATLAS detector. Unlike other particles resulting from collisions at the LHC, muons are weakly interacting and typically only lose a fraction of their energy traversing the inner detector and calorimeter system. To take advantage of the fact that muons are the only particles (except for neutrinos)

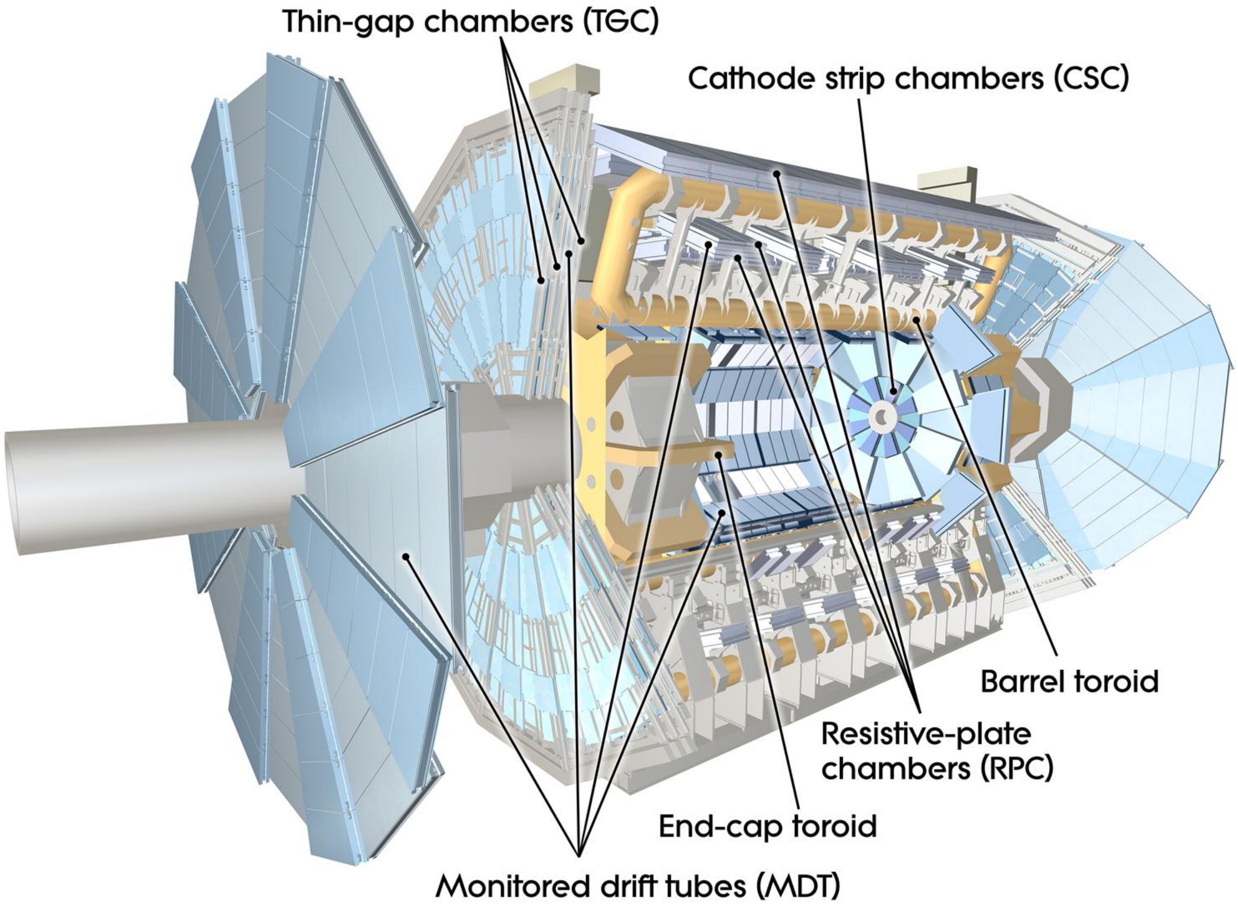

Figure 3.10: The muon system of the ATLAS detector.

exiting the calorimeter system of the ATLAS detector, the muon system is constructed around the calorimeter system and is used to measure the momentum and charge of muons which offer a very efficient way to identify events of interest. The muon system works in a similar manner as the inner detector and uses a strong magnetic field to bend the trajectory of charged particles (muons in this case) as they traverse a set of granular detectors. Combining information from the inner detector and the muon spectrometer allows for tracks to be matched, increasing the momentum resolution for muons. To increase the quality of the objects that we consider in this analysis, muons are required to have tracks in the muon spectrometer and for those tracks to be matched to tracks in the inner detector.

The muon system can be logically divided into three components: a set of eight air-core toroid magnets [41] placed axially around the calorimeter system, the muon spectrometer and the muon trigger system which are built on and around the toroid magnets. The muon spectrometer provides measurements of muon momentum and charge while the muon trigger system is a dedicated set of detectors that provide information with a very small latency that is used to identify events of interest (those with high energy muons) used for triggering.

The muon spectrometer is composed of three layers of detectors that are composed of monitored drift tubes (MDTs) and cathode strip chambers (CSCs). The magnetic field produced by the large toroid magnets is used to bend the trajectory of muons, allowing their charge and momentum to be inferred. The MDTs and CSCs are placed in concentric cylinders before, between, and after the the coils of the toroid magnets in the barrel region. In the endcap region, these are located before and after the endcap magnets.

The MDT chambers cover the region within $|\eta| < 2.7$ except for the region $2.0 < |\eta| < 2.7$ where the first layer is replaced by CSCs. The MDTs are tubes with a diameter of 29.970 mm that contain pressurized gas and a central anode wire that is kept at a potential difference relative to the enveloping cathode tube. When muons traverse the gas in the tube, the gas becomes ionized and swept towards the central wire to be readout.

The forward region ($|\eta| > 2.0$) is characterized by high particle density which results in a large particle flux and high track density. The MDTs can safely handle a particle flux of about 150 Hz/cm^2. In the forward region, this limit is exceeded. To preserve the momentum resolution of the MS found in the barrel region, the first layer of the MS in the region $2.0 < |\eta| < 2.7$ are replaced by CSCs. The CSCs are multiwire proportional chambers. A set of anode wires are sandwiched between two sets of cathode strips. One set of cathode strips runs parallel to the anode wires and the other set run perpendicular to the plane containing the anode wires. When a charged particle traverse the CSC, the gas is ionized. By interpolating the charge between neighboring cathode strips, the position coordinate in both directions in the plane of the detector can be inferred. Using the additional information provided by the CSCs compared to the MDTs, ambiguities between multiple tracks in the detector can be resolved.

The muon trigger system covers the range $|\eta| < 2.4$. The resistive plate chambers (RPCs) cover the barrel region in $|\eta| < 1.05$ and thin gap chambers (TGCs), which are similar to CSCs, extend this to the endcaps in $|\eta| < 2.4$. The RPCs and TGCs have lower precision than the MDTs and the CSCs but provide quicker readout and provide information on the number and an estimate of their energy.

RPCs are chambers with anode and cathode plates. When a muon traverses the chamber, the gas is ionized. The ions are swept to the positive side while being pushed from the negative side, producing a current in the readout electronics.

3.2.5 Trigger and readout

The LHC produces collisions every 25 ns in the ATLAS detector which corresponds to a rate of 40 MHz. If the data from the ATLAS detector was recorded every collision, the amount of data being recorded would exceed $10\,\mathrm{TB\,s^{-1}}$. Since the bandwidth available for detector readout as well as the amount of storage space available to CERN is limited, this rate of data collection is not feasible and must be reduced.

The solution to this problem starts with the realization that the vast majority of the collisions produced in the ATLAS detector are uninteresting soft collisions and can be ignored. To reduce the amount of data that is required to be collected to a manageable level while simultaneously minimizing the number of interesting events that are left unrecorded, ATLAS employs a two layer trigger (event screening) system [42].

The trigger system is required to determine whether or not the ATLAS detector should be readout on the time scale of the time between collisions. Once the data from the ATLAS detector is readout, more time can be taken to decide if the event should actually be recorded for offline analysis. This two step process matches what is used in the ATLAS detector.

The first level of the trigger system is implemented using custom electronic circuits that use a subset of the data provided by the muon and calorimeter systems to quickly determine if something worth looking at more closely is present. If something of interest is found by the low level trigger, the ATLAS detector is readout and passed to the high level trigger (HLT). The low level trigger system reduces the 40 MHz rate of collisions at the interaction point to about 80 kHz.

The HLT is software running on a dedicated server farm that performs partial reconstruction of the event using algorithms similar to what is used in offline analysis. The decision to keep an event or not is based on whether or not the event matches one of the HLT triggers, which define signatures of interest to the ATLAS physics program. The HLT further reduces the rate at which events are recorded to 1 kHz.

Chapter 4

Data Samples

4.1 Data sample

The data used to perform the analysis presented in this thesis was collected by the ATLAS detector during the period from 2015 to 2018. The data set corresponds to an integrated luminosity of $139\,\mathrm{fb}^{-1} \pm 1.7\%$ of proton–proton collision data at a center-of-mass energy of $\sqrt{s} = 13\,\mathrm{TeV}$. To maintain the quality of the data used, only data collected while the LHC and ATLAS detector were fully operational are considered. Only events collected while the time between collisions was 25 ns are considered for use. This includes part of the data set collected during 2015 and the entire data set collected from 2016 to 2018.

Events are recorded for offline analysis if they match a set of requirements that define one of the high level triggers described in Section 3.2.5. Events used in this thesis are required to pass the trigger requirements for at least one of the single-electron and single-muon triggers that are described in References [43, 44, 45, 46].

The single-electron triggers select events where there is a track in the inner detector matched to a cluster in the calorimeter system. A likelihood discriminate is trained to identify electrons using the track and cluster information. Based on the output of the likelihood discriminate, electrons are classified as either "LooseLH", "MediumLH", or "TightLH".

These classifications correspond to the likelihood that the electron is correctly identified, with loose electrons being most likely to be mis-identified and tight electrons being the most likely to be correctly identified. In 2015 the single-electron triggers required electrons to satisfy the medium identification requirements and have $E_{\mathrm{T}} > 24\,\mathrm{GeV}$. During the period from 2016 to 2018, electrons had to satisfy the tight identification requirements, be isolated from nearby objects, and have $E_{\mathrm{T}} > 26\,\mathrm{GeV}$. Electrons can be more reliably identified when they have a high p_{T}. Two other triggers were implemented that were optimized to efficiently select electrons with high p_{T}: one selects electrons with $E_{\mathrm{T}} > 60\,\mathrm{GeV}$ that satisfy the medium identification requirement and another selects electrons with $E_{\mathrm{T}} > 120\,\mathrm{GeV}$ in 2015 and $E_{\mathrm{T}} > 140\,\mathrm{GeV}$ from 2106 to 2018.

The single-muon triggers select events that have tracks in the inner detector and the muon spectrometer. Similarly to the single-electron triggers, the single-muon triggers make use of likelihood discriminates that classify muons if they satisfy a tight, loose, or medium identification and isolation requirements. In 2015 the single-muon triggers required muons to have $p_{\mathrm{T}} > 20\,\mathrm{GeV}$ and to satisfy a loose isolation requirement. During the period from 2016 to 2018, the single-muon triggers required that muons have $p_{\mathrm{T}} > 26\,\mathrm{GeV}$ and satisfy a medium isolation requirement. To make use of the fact that muons can be more reliably classified at high p_{T}, an additional single-muon trigger is used to select muons with $p_{\mathrm{T}} > 60\,\mathrm{GeV}$ regardless of isolation classification.

Chapter 5

Object Reconstruction

This chapter describes the procedure used to reconstruct the particles produced in a collision from the raw data collected by the ATLAS detector as well as other requirements on events and reconstructed objects used in the analysis present in this thesis. The requirements on reconstructed objects follow the standard recommendations provided by the ATLAS CP (combined performance) groups for collision data collected by ATLAS in the period from 2015 to 2018.

This thesis considers five different types of physics objects that are reconstructed from the raw data collected by the ATLAS detector. These include: electrons, ($e^{\pm}$), photons (γ) muons ($\mu^{\pm}$), jets (j) and missing transverse energy ($E_{\mathrm{T}}^{\mathrm{miss}}$). The remainder of this chapter will describe how these objects are reconstructed and the requirements used to define them.

The ATLAS detector is composed of many different subdetectors. The choice and placement of the subdetectors was driven by the need to be able to accurately and efficiently measure the charge, momentum and energy of different particles as well to distinguish different particles with sufficient accuracy. The interaction of different particles with each of the ATLAS subdetectors is illustrated in Figure 5.1. Electrons are light, charged leptons and leave tracks in the inner detector and shower primarily in the electromagnetic calorimeter. Photons leave a similar signature in the electromagnetic calorimeter but do not leave tracks in the inner detector. Muons are basically heavy electrons that interact weakly with the ATLAS detect compared to other particles and so are the only charged particles to reach the muon spectrometer. Hadrons primarily interact with the hadronic calorimeter, leaving jets of strongly interacting particles as their energy is deposited into the hadronic calorimeter. The relatively long lifetime of b hadrons that result in a displaced vertex and other small differences allows them to be efficiently identified. $E_{\mathrm{T}}^{\mathrm{miss}}$ represents the transverse momentum imbalance in an event.

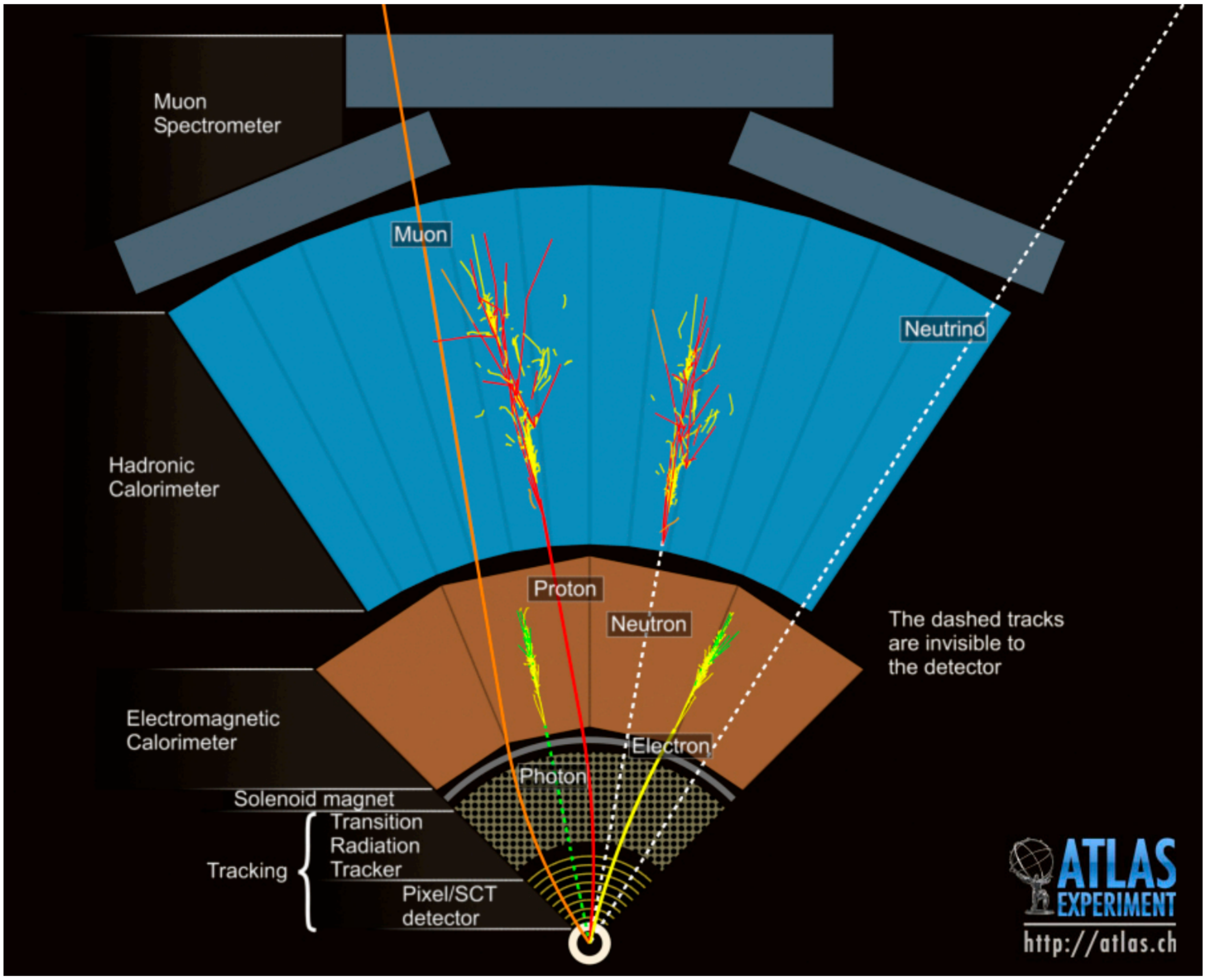

Figure 5.1: Illustration of the interactions of different particles with the different ATLAS subdetectors.

Physics objects such as electrons, muons, and jets are reconstructed by analyzing the raw information provided by the ATLAS detector and all of its subdetectors. Reconstructed objects can be identified with varying degrees of certainty depending on the requirements, or working point, used to define the particle. Different working points offer different true positive and false negative rates. Particles that are correctly identified and arise from the primary interaction are called prompt while those that are incorrectly identified or incorrectly identified as coming from the primary interaction are referred to as nonprompt. Nonprompt objects can either originate from the decay of a particle produced in the primary interaction, arise from pileup collisions, or the particle can misidentified. The working point used by an analysis depends on the phase space where the measurement is performed and the size of the nonprompt backgrounds expected. Working points with high true positive rates are often referred to as ”tight” working points and those with low true positive rates are referred to as ”medium” or ”loose” working points. For the analysis presented in this thesis, working points are selected to provide small false positive rates so that additional background estimation and validation for these extra backgrounds is not required.

5.1 Electrons

Electrons are reconstructed from energy deposited in the electromagnetic calorimeter matched to tracks in the inner detector. A likelihood (LH) discriminant is trained using several variables including the shape of the shower in the electromagnetic calorimeter, the ratio of the energy deposited in the calorimeter to the momentum measured from the matched track in the inner detector to separate prompt and nonprompt electrons. Higher values of the LH discriminant are associated with a higher background rejection efficiency (lower false positive rate) but lower signal acceptance efficiency (true positive rate). Discrete working points are defined by requiring the LH output to be greater than some value. The discrete working points are referred to as LooseLH, MediumLH, and TightLH. Where the TightLH working point provides the highest background rejection efficiency (lowest false positive rate). In this analysis, electrons are required to pass the TightLH identification requirement. To reject nonprompt electrons (jets faking an electron signature, photon conversion, etc.), electrons are required to be isolated from other physics objects. Similar to the identification working points, there also exist isolation working points. For this analysis, we require electrons to pass the PLVTight (prompt lepton veto tight) working point. Electrons are required to have $p_{\mathrm{T}} > 20\,\mathrm{GeV}$ and $0 < |\eta| < 1.37$ or $1.52 < |\eta| < 2.47$. The region between $1.37 < |\eta| < 1.52$ is referred to the calorimeter crack region and is excluded due to the poor electron identification efficiency in this region. To reject electrons originating from the decay of a secondary particle (W, Z, heavy flavor hadron, etc.), electrons considered in this analysis are required to be consistent with the primary collision. The ratio of the transverse distance from the beam line to the primary vertex, referred to as the transverse impact parameter, and its uncertainty

$$d_0\text{Significance} = |d_0|/\sigma(d_0) \tag{5.1}$$

is required to be less than 5.0. Additionally, the difference between the track origin and the primary vertex, $|\Delta Z_0 \sin(\theta)|$, is required to be less than 0.5 mm. MC correction scale factors calculated by comparing MC simulation to data are used to correct differences between MC simulation and data [47].

5.2 Muons

Muons are reconstructed from tracks in the muon spectrometer and the inner detector [48]. Muons are weakly interacting particles and are the only charged particle to escape the calorimeter system. For this reason, muons are more reliably identified compared to electrons. To reject mis-identified muons, originating primarily from pion and kaon decay, muons are required to pass the Medium identification requirement. The Medium identification requirement ensures that there are hits in the muon spectrometer and that the hits in the muon spectrometer and the inner detector are compatible. To reject nonprompt muons, muons considered in this analysis are required to be isolated from other objects. This is accomplished by requiring muons to pass the `PflowTight_FixedRad` isolation working point [49] and muons are required to have $|d_0\text{Significance}| < 3.0$ and $|\Delta Z_0 \sin(\theta)| < 0.5$ mm. The analysis only considers muons with $p_{\text{T}} > 20\,\text{GeV}$ that fall with $|\eta| < 2.5$. MC correction scale factors calculated by comparing MC simulation to data are used to correct differences between MC simulation and data [50].

5.3 Photons

Photons have a similar signature in the electromagnetic calorimeter to electrons. The main difference between electrons and photons as seen by the detector is that photons are not charged so they do not leave tracks in the inner detector. Photons are reconstructed from energy deposited in the electromagnetic calorimeter. To ensure that photons considered in this analysis are properly identified, photons are required to pass the Tight identification working point [51]. When photons interact with the material, the photons can convert to an electron-positron pair. If this occurs within the inner detector, the photon can leave tracks in the inner detector, just like an electron. Photons are required to not have a hit in the inner b-layer. If there are hits in other layers of the inner detector but the decay vertex is reconstructed, the photon is still considered. Photons are also required to be isolated from other objects by requiring they pass the FixedCutTight isolation requirement [51]. Photons considered in this analysis are required to to have $p_{\text{T}} > 20\,\text{GeV}$ and fall within $|\eta| < 2.37$ but not in the calorimeter crack region within $1.37 < |\eta| < 1.52$. MC correction scale factors calculated by comparing MC simulation to data are used to correct differences between MC simulation and data [47].

5.4 Jets

Hadrons interacting in the hadronic calorimeter manifest as showers of hadronic particles that leave energy deposits in the calorimeters. Since hardrons can also be charged, the information collected by the calorimeter system can be combined with information from the inner detector in the range $|\eta| < 2.5$. Jets are reconstructed using the anti-k_t algorithm [52] with a radius parameter $R = 0.4$. The input to the anti-k_t algorithm are objects provided by the particle flow (PFlow) [53] algorithm within $|\eta| < 2.5$ and are referred to as particle flow or PFlow objects. In the forward region, $|\eta| > 2.5$, the input to the anti-k_t algorithm is information from the calorimeter system. These objects approximate individual particles and are formed by combining information from the inner detector and calorimeters. A discriminant is trained to reject jets from pileup in the central region of the detector called the JVT (jet vertex tagger) discriminant [54]. Jets with $p_{\mathrm{T}} < 60\,\mathrm{GeV}$ and within $|\eta| < 2.4$ are required to have a JVT > 0.59. Additionally, jets are required to have $p_{\mathrm{T}} > 20\,\mathrm{GeV}$ and be within the range $|\eta| < 2.5$. MC correction scale factors calculated by comparing MC simulation to data are used to correct differences between MC simulation and data [55].

5.5 b-jets

Hadrons containing b quarks have a relatively long lifetime that results in a displaced vertex and allows jets originating from hadrons containing a b quark to be identified efficiently. Since the branching ratio of the top quark to a b quark ($t \rightarrow W^{\pm}b$) is effectively 100%, being able to identify or tag a jet as originating from a hadron containing a b quark is very useful for identifying processes with top quarks. In this analysis, jets tagged as b-jets are referred to as b-jets and are a subset of the jets previously discussed. Hence, b-jets pass all the requirements discussed in Section 5.4. In addition to the jet requirements, b-jets are required to be tagged as a b-jet by the `Dl1r` algorithm [56] at the 85% working point which corresponds corresponds to a true positive rate of 85% for identifying b-jets. The

`DL1r` algorithm is a neural network trained on the output of several other discriminants that makes use of information related to the long lifetime of b hadrons such as the presence of a displaced vertex and the decay of the b hadron.

5.6 Missing transverse momentum

Missing transverse momentum, $E_{\mathrm{T}}^{\mathrm{miss}}$, represents the momentum imbalance in an event due to neutrinos that do not interact with the detector. $E_{\mathrm{T}}^{\mathrm{miss}}$ is reconstructed by taking the negative sum of the momentum of all reconstructed objects that have been discussed so far (electrons, muons, jets) as well as an additional term referred to as the soft term that contains all of the tracks associated with the primary collision that are not accounted for in the reconstructed objects [57, 58]. The soft term accounts for the objects that do not pass the p_{T} requirements for reconstructed objects.

5.7 Overlap removal

To avoid assigning energy deposits in the calorimeter system or tracks in the inner detector to more than one object, the standard overlap removal algorithm is applied to the reconstructed objects described in this chapter:

1. If there exists an electron and a muon in an event and the electron and muon are reconstructed using the same track in the inner detector, then the electron is removed.

2. If there exists an electron and a jet in an event, and the jet is within $\Delta R < 0.2$ of the electron, then the jet is removed. If the jet is between $0.2 < \Delta R < 0.4$ of the electron, then the electron is removed.

3. If there exists a muon and a jet in the event and the jet is within $\Delta R < 0.2$ of the muon and the jet and muon are reconstructed using no more than two of the same tracks in the inner detector, then the muon is removed; otherwise, the jet is removed.

4. If there exists an electron or muon and a photon in the event and the photon is within $\Delta R < 0.4$ of the one of the leptons, then the photon is removed.
5. If there exists a photon and a jet in an event and the jet is within $\Delta R == 0.4$ of the photon, then the jet is removed.

Chapter 6

Monte Carlo Simulated Samples

6.1 Monte Carlo simulated samples

In addition to data collected by the ATLAS detector, Monte Carlo (MC) simulated samples are also produced, representing the theory prediction that we compare to data collected by the ATLAS detector. These MC samples can be divided into separate categories: the $W^{\pm}W^{\mp}\gamma$ signal sample and samples for processes that are backgrounds to, or mimic, the signal process. The background processes can be further divided into samples for processes that have the same final state as $W^{\pm}W^{\mp}\gamma$ and those that do not. The processes that have the same final state as the signal enter the region where we perform the measurement of $W^{\pm}W^{\mp}\gamma$ naturally. MC typically models these processes well, allowing us to use the samples directly in the statistical analysis after being validated properly. Processes that do not have the same final state can still contribute to the $W^{\pm}W^{\mp}\gamma$ background through detector effects and by the algorithms that are used to reconstruct physics objects mis-identifying the object. These processes are typically not well modeled by MC simulation and require additional effort to correct the modeling before they can be used during the statistical analysis.

The reconstruction algorithms employed in ATLAS to reconstruct the underlying event are not perfect. There are residual effects related to selection efficiencies, energy resolution and energy scale. For this reason, the MC simulated events cannot be directly compared to data but must be first transformed to take into account the various detector effects. This is accomplished by simulating the ATLAS detector [59] modeled using the `GEANT4` [60] simulation software package. There are two types of simulation: full simulation and fast simulation. Fast simulation is faster, but uses a simplified model of the electromagnetic and hadronic calorimeters and full simulation [61] uses `GEANT4` to model the entire detector. This substitution can affect the modeling of jets and $E_{\mathrm{T}}^{\mathrm{miss}}$. The particles in each MC event then traverse the simulated detector, producing simulated ATLAS data that can be processed using the same reconstruction software as real data.

Differences between reality (data) and simulation (MC) are accounted for by using a set of corrections derived by comparing data to MC simulation for well understood processes as well as a set of variations that parameterize how different detector effects could affect the resulting events. The correction factors that are applied to MC simulation account for several effects including: the efficiency of the requirements that we apply to events and objects in those events, the resolution of the detector, and systematic offsets that can affect observable quantities.

Each MC simulated sample is re-weighted such that the total number of events for each simulated process is given by Equation 3.2, relating the theoretical cross section and the experimentally derived integrated luminosity.

For the data collected by the ATLAS detector, each event is accompanied by additional interactions in the same bunch crossing or neighboring bunch crossings, referred to as pile-up, that obfuscate the event of interest by introducing extra tracks in the inner detector or energy deposits in the calorimeter system. To properly compare MC simulated events and data, the effect of pile-up is accounted for by simulating this process using the PYTHIA8 software package and the A2 [62] tune and overlaying this onto each MC simulated sample. Since the pile-up conditions in the ATLAS detector change over time, the pile-up contribution is re-weighted to match the average number of pile-up events observed during the operation of the ATLAS detector.

6.1.1 $W^{\pm}W^{\mp}\gamma$ signal sample

The $W^{\pm}W^{\mp}\gamma$ signal process is simulated at NLO in QCD using SHERPA 2.2.11 [63] and the NNPDF3.0 NNLO PDF set. Up to two additional light-flavor jets are simulated at LO in QCD and added to the NLO $W^{\pm}W^{\mp}\gamma$ process. The $W^{\pm}W^{\mp}\gamma$ signal sample includes all process that contribute to the $\ell\nu\ell\nu\gamma$ final state. This includes contributions from processes other than $W^{\pm}W^{\mp}\gamma$ such as $ZZ\gamma$ where one Z boson decays to $Z \rightarrow \tau^{\pm}\tau^{\mp} \rightarrow e^{\pm}\mu^{\mp}\gamma$ and the other decays to neutrinos or jets as well as events from $W^{\pm}W^{\pm}\gamma$+jets where the two W bosons have the same charge. The cross section for the $W^{\pm}W^{\mp}\gamma$ signal sample is 441.4 fb.

Since the analysis presented in this thesis seeks to study the $W^{\pm}W^{\mp}\gamma$ process only; a set of requirements are applied at the level of the generator, defining a fiducial region enriched in $W^{\pm}W^{\mp}\gamma$ events. Once the $W^{\pm}W^{\mp}\gamma$ measurement is performed, the result will be extrapolated to the fiducial region rather than the total phase space included in the generated sample.

The fiducial volume is defined such that it contains the events selected by the cuts applied after event reconstruction defining the signal region where $W^{\pm}W^{\mp}\gamma$ is measured. Photons are required to have $p_{\mathrm{T}} > 20\,\mathrm{GeV}$ and be within $|\eta| < 2.37$. Since charged leptons can radiate photons, photons are rejected if there is an electron within $\Delta R < 0.2$ of the photon or a muon within $\Delta R < 0.1$ of the photon. Leptons are required to have $p_{\mathrm{T}} > 20\,\mathrm{GeV}$ and be within $|\eta| < 2.50$. Since leptons can arise from the decay of jets, leptons are discarded if there is a jet with $p_{\mathrm{T}} > 20\,\mathrm{GeV}$ and $|\eta| < 4.5$ within $\Delta R < 0.1$ of the lepton. Electrons arising from the decay of τ leptons are considered as well as electrons of muons directly from the W boson decay. The fiducial volume is defined as having at least one photon and an opposite-flavor, opposite-charge electron-muon pair satisfying the requirements above. To account for the p_{T} requirement associated with the single-electron and single-muon triggers, one lepton is required to have $p_{\mathrm{T}} > 25\,\mathrm{GeV}$. After applying the fiducial volume selection, the fiducial cross section is found to be 10.54 fb $^{+1.79}_{-1.18}\%$ due to PDF uncertainties and $^{+16.97}_{-11.21}\%$ due to scale uncertainties. The PDF uncertainty is found by varying the PDF set used and the scale uncertainty is found by varying the renormalization and factorization scales.

6.1.2 Prompt photon background MC samples

There are three process that contribute a significant amount to the background for the $W^{\pm}W^{\mp}\gamma$ process and have a prompt (not nonprompt or fake) photon: $t\bar{t}\gamma$, $Z\gamma$, and $VZ\gamma$.

$t\bar{t}\gamma$: $t\bar{t}\gamma$ and $tW\gamma$

The $t\bar{t}\gamma$ and $tW\gamma$ are collectively referred to as $t\bar{t}\gamma$ in this thesis since the $t\bar{t}\gamma$ process and the $tW\gamma$ process only differ by an additional b-jet in the final state.

The largest background for this analysis comes from $t\bar{t}\gamma$. The only difference between the signal process and $t\bar{t}\gamma$ is the additional jets from the top decay. Two separate $t\bar{t}\gamma$ samples are produced and combined: one where the associated photon arises from the initial interaction and one where the photon arises from the top quark decay or subsequent decay products. The $t\bar{t}\gamma$ process is simulated using MadGraph5_aMC@NLO 2.7.3 [64] and the `NNPDF3.0 NLO` [65] PDF set. The event generator is interfaced with Pythia 8.240 [66] using a custom parameter tune referred to as the A14 parameter tune [67]. Pythia8 models the parton shower, hadronization, and fragmentation of the underlying event. Top quarks are decayed using MadSpin [68, 69] to preserve spin correlations. The other heavy flavor quarks (bottom and charm) are decayed using the EvtGen v1.6.0 software package. The $t\bar{t}\gamma$ process where the photo arises from the initial interaction is simulated at NLO in QCD. The $t\bar{t}\gamma$ process where the associated photon is radiated from the decay products of the top quarks or W bosons is simulated as $t\bar{t}$ at LO in QCD and a photon is required to come from the decay of the top quarks or subsequent decay products.

The simulation of $tW\gamma$ is handled in a similar manner as the $t\bar{t}\gamma$ process: one sample is produced where the photon arises from the initial interaction and one sample where the photon arises from the decay of the top quark or the W boson or their subsequent decay products. The $tW\gamma$ process is simulated using MadGraph5_aMC@NLO and the `NNPDF2.3lo` PDF set at LO in QCD. MadGraph is interfaced to Pythia 8.240 using the A14 parameter tune to handle the parton shower, hadronization and fragmentation of the underlying event and the decay of heavy-flavor quarks is handled by the EvtGen software package.

$Z\gamma$

$Z\gamma$ is the second largest background to the $W^{\pm}W^{\mp}\gamma$ signal process. Events from $Z\gamma$ mimic the $W^{\pm}W^{\mp}\gamma$ process when the Z boson decays to τ leptons which then decay to an electron and a muon. The $Z\gamma$ process is simulated using Sherpa 2.2.8 and the NNPDF3.0 NNLO PDF set. Two or three light-jets are simulated at LO in QCD and combined with the NLO $Z\gamma$ process. Events where the Z boson is off-shell ($\ell\ell\gamma$) are also included. The photon in the event can originate from the initial interaction or can be radiated from the charged particles in the event.

$VZ\gamma$: $WZ\gamma$ and $ZZ\gamma$

The $VZ\gamma$ process contains contributions from $W^{\pm}Z\gamma$ and a much smaller contribution from $ZZ\gamma$.

$W^{\pm}Z\gamma$ events can enter the signal region when the W and Z boson decay to opposite-flavor leptons and one of the leptons associated with the Z decay is not reconstructed. The $W^{\pm}Z\gamma$ process is simulated using Sherpa 2.2.11 and the NNPDF3.0 NNLO PDF set. Up to two light-flavor jets are simulated at LO in QCD and combined with the NLO $W^{\pm}Z\gamma$ process. The photon associated with the event can arise from either the initial interaction or be radiated from the charged particles associated with the event.

$ZZ\gamma$ contributes a very small amount to the $W^{\pm}W^{\mp}\gamma$ background and is combined with the $W^{\pm}Z\gamma$ process throughout this thesis. The $ZZ\gamma$ process can mimic the $W^{\pm}W^{\mp}\gamma$ signal process in a similar manner to the $W^{\pm}Z\gamma$ process except that two leptons are required to not be reconstructed. The $ZZ\gamma$ process is simulated using Sherpa 2.2.5 and NNPDF3.0 NNLO PDF set. Up to three light-flavor jets are simulated at LO in QCD and combined with the NLO $ZZ\gamma$ process. The photon associated with the event can arise from either the initial interaction or be radiated from the charged particles associated with the event.

6.1.3 Nonprompt photon background MC samples

Some processes can mimic the signal when an electron or a jet is reconstructed as a photon. These processes have corresponding process with a prompt photon: $t\bar{t}$, WW, WZ, and Z+jets. Since MC does not typically model nonprompt processes well, the MC estimates for these backgrounds are corrected using data-driven MC correction scale factors that are discussed in Section 9.3 and Section 9.4 respectively. In this section we will mention how the underlying MC samples are produced.

VV: WW, WZ

The WW and WZ processes are collectively referred to as VV or diboson throughout this thesis. The diboson process corresponds to the signal ($W^{\pm}W^{\mp}\gamma$), and the $W^{\pm}Z\gamma$ and $ZZ\gamma$ background processes without a prompt photon; therefore, these processes can mimic the signal in the same way as the corresponding prompt photon process as long as a nonprompt photon is present. The mechanism that produces the nonprompt photon depends on the process. For $WZ \to \mu^{\pm}e^{\mp}e^{\pm}$, the electron that has the same charge as the muon from the W boson decay can either be reconstructed as a photon or the electron can radiate a photon and only the radiated photon is reconstructed. For the other diboson processes, the only significant mechanism that produces nonprompt photons is jets faking photons.

The VV process is simulated at NLO in QCD using Sherpa 2.2.2 and the `NNPDF3.0nnlo` PDF set. Up to one additional light-flavor jets are simulated at LO in QCD and added to the NLO $W^{\pm}W^{\mp}\gamma$ process. The virtual QCD correction were provided by the OpenLoops 1 library [70, 71, 72]. Off-shell W and Z contributions are included so the process simulated is $\ell\ell\nu\nu$, and $\ell\ell\ell\nu$. The case where there are four, one or zero leptons produced are not considered in this thesis since their contribution is found to be negligible.

$t\bar{t}$: $t\bar{t}$ and tW

The $t\bar{t}$ and the tW processes are collectively referred to as $t\bar{t}$ in this thesis. These backgrounds differ from the $t\bar{t}\gamma$ process by the absence of a prompt photon; therefore, $t\bar{t}$ can mimic the $W^{\pm}W^{\mp}\gamma$ signal in the same way that $t\bar{t}\gamma$ does as long as there exists a nonprompt photon. The only significant mechanism for nonprompt photons to be produced with $t\bar{t}$ events is through jets faking a photon.

The $t\bar{t}$ process is simulated at NLO in QCD using Powheg-Box v2 [73, 74, 75, 76] and the NNPDF3.0NLO PDF set. MadGraph is interfaced to Pythia 8.230 using the A14 parameter tune to handle the parton shower, hadronization and fragmentation of the underlying event and the decay of heavy-flavor quarks is handled by the EvtGen v1.6.0 software package.

The tW process is simulated at NLO in QCD using Powheg-Box v2 in the 5-flavor scheme and the `NNPDF2.3lo` set of PDFs. MadGraph is interfaced to Pythia 8.230 using the A14 parameter tune to handle the parton shower, hadronization and fragmentation of the underlying event and the decay of heavy-flavor quarks is handled by the EvtGen v1.6.0 software package. Diagram removal is used to remove interference and overlap between the $t\bar{t}$ and tW samples.

Z+jets

The Z+jets process corresponds to the $Z\gamma$ process without a prompt photon; therefore, Z+jets events can mimic the $W^{\pm}W^{\mp}\gamma$ signal as long as a nonprompt photon is present. The only significant mechanism for nonprompt photons to be produced with $t\bar{t}$ events is through jets faking a photon.

The Z+jets process is simulated at NLO in QCD using Sherpa 2.2.1 and the `NNPDF3.0nnlo`

PDF set. While the sample is produced at NLO in QCD, the NNLO cross section is available [77] and is used to normalized the Z+jets sample to the NNLO prediction. Up to two partons are simulated at NLO in QCD and up to four partons are simulated at LO in QCD using the Comix [78] and OpenLoops 1 libraries.

Chapter 7

Experimental Systematic Uncertainties

The theoretical prediction from MC simulation, the modeling provided by the ATLAS detector, and the reconstruction of data and MC introduce several sources of uncertainty into the analysis of ATLAS data. To properly compare MC simulation representing the theoretical prediction and ATLAS data, these different uncertainties need to be estimated and included in the statistical analysis. This is accomplished by generating variations for each source of uncertainty and including them as independent nuisance parameters when the measurement is performed.

7.1 MC prediction uncertainties

The theoretical prediction provided by MC is an estimate that often makes many assumptions. The effect of these assumptions and approximations is provided by PDF set variations, variations of the renormalization and factorization scales, variation of parameters associated with the parton shower, and comparing MC simulated samples generated using different generators that make different assumptions. These uncertainties are referred to as theoretical uncertainties. In the analysis presented in this thesis, theory uncertainties are included for the $W^{\pm}W^{\mp}\gamma$ signal process as well as for the $t\bar{t}\gamma$ and $Z\gamma$ processes since they comprise the majority of the background to the $W^{\pm}W^{\mp}\gamma$ process.

The uncertainty due to initial-state-radiation (ISR) was estimated by comparing the nominal $t\bar{t}\gamma$ sample with two additional samples, which have the same setting as the nominal one, but with the Var3c up or down variation of the A14 tune, which corresponds to the variation of α_{S} for initial state radiation (ISR) in the A14 tune.

To evaluate the renormalization and factorization scale uncertainties, the two scales were varied simultaneously by factors 2.0 and 0.5. To evaluate the PDF uncertainties for the nominal PDF, the 100 replicas for `NNPDF2.3lo` were taken into account.

The renormalization and factorization scale uncertainties are estimated using the internal SHERPA 2.2.11 weights by varying μ_R and μ_F separately up and down by a factor of 2 with respect to the nominal weight. The effect of varying μ_R and μ_F is estimated simultaneously on the Matrix-element calculation and the parton shower. Similarly, the PDF systematic effects are estimated using the internal SHERPA 2.2.11 weights of the `PDF4LHC` resulting in 30 nuisance parameters.

An exact approach as in $W^{\pm}W^{\mp}\gamma$ was used to estimate the renormalization, factorization scale and PDF uncertainties.

7.2 Experimental systematic uncertainties

The uncertainties arising from inaccuracies in the simulation of the ATLAS detector, as well as the uncertainties associated with the reconstruction of objects making up the underlying event in data and MC such as the resolution of the detector, are taken into account by producing different MC samples that are produced under different assumptions about the operation of the ATLAS detector. These uncertainties are referred to as experimental uncertainties. In this way, all uncertainty other than the Poisson statistical uncertainty on data is applied to MC simulation.

There are two types of systematic uncertainties: those that affect only the weight associated for each event and those that affect the reconstructed event itself and must be represented as a completely new sample with events containing potentially different reconstructed objects. The latter kind of systematic uncertainties are associated with uncertainties that affect the four-vectors of the events and can result in the objects associated with the event being reconstructed as different objects, not reconstructed at all, or objects that were previously removed being reconstructed.

The remainder of this section will describe groups of systematic uncertainties and how they are produced.

7.2.1 Luminosity

The uncertainty on the integrated luminosity collected from 2015 to 2018 that is used in the analysis presented in this thesis is 1.7% [26]. The uncertainty is obtained by performing beam-separation scans [24] and the information collected by the LUCID-2 ATLAS subdetector [79]. Further details on the luminosity measurement can be found in Reference [26].

7.2.2 Uncertainty in pileup modeling

Pileup is accounted for by simulating additional soft interactions and overlaying these onto MC simulated samples. The distribution of the number of interactions per event in the MC simulated samples is re-weighted to match the distribution of the number of interactions per event observed in data for each data taking period. The distribution of the number of interactions per event used is for the re-weighting procedure is varied by its uncertainty to generate alternative event weights [80] that are propagated through the analysis and used as systematic uncertainties in the $W^{\pm}W^{\mp}\gamma$ signal strength measurement.

7.2.3 Lepton systematic uncertainties

There are several sources of uncertainty associated with reconstructed electrons and muons in MC simulation. For electrons, the systematic uncertainties that are considered are related to the trigger, identification, isolation, and reconstruction efficiency. For muons, these same systematic uncertainties are considered as well as systematic uncertainties associated with the inner detector (ID), the muon spectrometer (MS), momentum scale, as well as a track-to-vertex-association (TTVA) impact parameter selection.

MC simulation is corrected by applying scale factors that are derived using the tag-and-probe method [81, 48] applied to sets of events that are selected to be enriched in events from the well understood $Z \rightarrow ee$ and $Z \rightarrow \mu\mu$ processes. These events are selected by taking advantage of the large Z+jets cross section as well as the fact that the reconstructed di-lepton mass ($m_{\ell\ell}$) will be close to the Z boson mass if the leptons originated from the decay of a Z boson. One of the leptons, referred to as the tag lepton, is required to pass a strict set of requirements so that it can be identified correctly with a high likelihood. The other lepton in the event is referred to as the probe lepton. By studying the the probe lepton, selection efficiencies can be studied and scale factors can be obtained that correct MC simulation as a function of different lepton kinematic variables to match the same distributions in data [82, 49].

Uncertainties are obtained by varying the selection requirements and the uncertainty on non-Z events that are included in the set of selected events. Uncertainties on the lepton momentum scale is obtained by performing the event selection after varying the lepton momentum up and down by 1σ and the uncertainties on the lepton momentum resolution are obtained by repeating the event selection after smearing the lepton momentum [50, 83].

7.2.4 Photon systematic uncertainties

Photon identification and isolation efficiencies are measured in data [84] and scale factors are calculated by taking the ratio of the efficiencies in data and MC simulation as a function of photon kinematic variables. Photon efficiencies are calculated using a set of events that are enriched in events where a photon is radiated from an electron in $Z \rightarrow e^{\pm}e^{\mp}$ decays. Photon efficiencies are also estimated by exploiting the similarity between showers in the electromagnetic (EM) calorimeter for electrons and photons to extrapolate from results obtained by studying $Z \rightarrow e^{\pm}e^{\mp}$ events without a radiated photon to photons. Systematic uncertainties are obtained by varying these scale factors up and down by their associated uncertainties. Systematic uncertainties related to the energy scale and resolution of photons are calculated together with the energy and scale resolution of electrons.

7.2.5 Jet systematic uncertainties

Systematic uncertainties on jets are separated into three categories: jet energy resolution, jet energy scale, and jet vertex tagger systematic uncertainties. Systematic uncertainties related to b-tagging are discussed in the next section.

Jet energy scale (JES)

The procedure used to calculate the jet energy calibration or jet energy scale and its associated systematic uncertainties is described in Reference [85, 55]. There are several different categories of effects that contribute the JES uncertainty including those uncertainties resulting from: modeling and statistical uncertainties from extrapolating from the central region, jet flavor composition, effects due to pileup interactions, detector response, b-jet energy scale, and more. Each of these categories of systematic uncertainties are often due to more than one physics process and are calculated using a variety of different methods.

Jet energy resolution (JER)

There are 13 separate systematic uncertainties related to the jet energy resolution. These systematic uncertainties are obtained by producing alternative samples after smearing the jet energy in the MC samples [86].

Jet vertex tagger (JVT)

An systematic uncertainty associated with the jet vertex tagger (JVT) [54] requirement used when selecting jets is obtained by varying the parameters associated with tracking and vertexing in the inner detector by the relevant detector resolution.

7.2.6 *b*-tagging systematic uncertainties

The largest background when studying $W^{\pm}W^{\mp}\gamma$ is from $t\bar{t}\gamma$. To differentiate between $W^{\pm}W^{\mp}\gamma$ and $t\bar{t}\gamma$, it is very efficient to veto events that contain a jet the has been tagged as arising from the decay of a b-hadrons, referred to as b-jets. Since b-hadrons have a longer decay length than light flavor jets, they can be differentiated. The act of classifying a jet as originating from a b-hadron is called b-tagging and, in this analysis, is performed using the `DL1r` algorithm. The efficiency (true positive rate) and mis-tag rate (false positive rate) for the b-tagging algorithm are measured in data using the methods described in References [87, 88, 89]. Systematic uncertainties on the b-tagging efficiency and mis-tag rate are obtained by varying the inputs to the b-tagging algorithm. The b-tagging algorithms make use of a large number of different variables, many of which are correlated. To reduce the number of components to be varied to produce systematic uncertainties and to de-correlate the input variables, primary component analysis (PCA) is used and only a subset of the most important components are kept, forming a lower dimensional space. Systematic uncertainties are obtained by varying the components of this lower dimensional space.

7.2.7 Missing transverse energy ($E_{\mathrm{T}}^{\mathrm{miss}}$) systematic uncertainties

The $E_{\mathrm{T}}^{\mathrm{miss}}$ is reconstructed [90] from the vector sum of several terms corresponding to electrons, muons, photons, and jets. The uncertainties due to these different reconstructed objects are propagated through the $E_{\mathrm{T}}^{\mathrm{miss}}$ calculation and so the effect of these uncertainties on the $E_{\mathrm{T}}^{\mathrm{miss}}$ calculation are accounted for in those systematic uncertainties. The only term that is not taken into account by other systematics is due to the soft-term in the $E_{\mathrm{T}}^{\mathrm{miss}}$ calculation. The uncertainty on the soft-term is estimated by comparing the ratio of the soft-term and the hard-term in MC simulation and data [91]. One systematic uncertainty is obtained by taking the average deviation of the ratio from one as an overall uncertainty. Two other systematic uncertainties are obtained by comparing the E_x^{miss} and E_y^{miss} resolution between data and MC simulation.

Chapter 8

Event Selection

8.1 $e^{\pm}\mu^{\mp}\gamma$ Signal Region

The $W^{\pm}W^{\mp}\gamma$ signal process can produce different final states in the ATLAS detector depending on whether the W bosons decay leptonically ($W^{\pm} \rightarrow \ell^{\pm}\nu$) or hadronically ($W^{\pm} \rightarrow jj$). The different final states can then be distinguished by the number of leptons in the final state. The final states with one or zero leptons suffer from very high backgrounds; therefore, only the two lepton final state is considered. The two lepton $W^{\pm}W^{\mp}\gamma$ final state can be classified into three different channels based on the flavor of the leptons: $e^{\pm}e^{\mp}$, $e^{\pm}\mu^{\mp}$, and $\mu^{\pm}\mu^{\mp}$. Processes that resemble the same-flavor final state produce an overwhelming number of events compared to the opposite-flavor channel; therefore, only the $e^{\pm}\mu^{\mp}$ channel is considered. It is also possible that the leptons have the same charge but this process is more rare than the same-charge process and is not considered as signal in this analysis.

In this analysis, the $W^{\pm}W^{\mp}\gamma$ process is studied in the $W^{\pm}W^{\mp}\gamma \rightarrow e^{\pm}\nu\mu^{\mp}\nu$ channel. This final state is characterized as having an opposite-charge electron muon pair and two neutrinos that are correlated with an imbalance in the transverse momentum measured in the ATLAS detector.

Processes that can mimic the $W^{\pm}W^{\mp}\gamma$ final state include: $t\bar{t}\gamma$, $Z\gamma$, and $W^{\pm}Z\gamma$. The

$t\bar{t}\gamma$ final state differs from the $W^{\pm}W^{\mp}\gamma$ final state by the presence of b-jets. These events can be largely vetoed by rejecting events with b-tagged jets. The $Z\gamma$ process can mimic the $W^{\pm}W^{\mp}\gamma$ final state when the Z boson decays to τ leptons that then decay to an electron and a muon plus neutrinos. The $W^{\pm}Z\gamma$ process can mimic the $W^{\pm}W^{\mp}\gamma$ final state when the W and Z bosons decay to opposite flavor leptons (e and μ) and the lepton with the same charge as the W boson is not reconstructed.

Other processes can mimic the $W^{\pm}W^{\mp}\gamma$ final state due to electrons or jets being misidentified as photons or from nonprompt photons. The processes that mimic the $W^{\pm}W^{\mp}\gamma$ final state due to jets faking prompt photons correspond to the signal and backgrounds with prompt photons but without the prompt photon. Processes that mimic the $W^{\pm}W^{\mp}\gamma$ final state due to electrons faking photons arise almost entirely to diboson events and WZ in particular. In this case, the WZ decays to $\mu^{\pm}e^{\mp}e^{\pm}$ and the electron with the same charge as the W boson fakes a photon. Since the nonprompt photon arises from the Z boson, the reconstructed mass of the electron and photon will be close to the Z boson mass. This is useful for removing this particular background.

A signal region (SR) is defined to maximize the number of $W^{\pm}W^{\mp}\gamma$ while minimizing the number of background events. From the preceding discussion, the $e^{\pm}\mu^{\mp}\gamma$ signal region can be defined as having one opposite-charge electron-muon pair, where one lepton has a $p_{\mathrm{T}} > 27\,\mathrm{GeV}$ to satisfy the trigger requirements discussed in Chapter 4, missing transverse momentum, no b-jets, and remove events where the reconstructed electron-photon mass ($m(e,\gamma)$) is consistent with the Z boson mass. The full cuts defining the $e^{\pm}\mu^{\mp}\gamma$ SR are given in Table 8.1. Distributions of kinematic variables for the electron, muon, and photon are given in Figure 8.1 and yields for the same region are given in Table 8.2. From the yields, we see that $t\bar{t}\gamma$ and $Z\gamma$ contribute the majority to the $W^{\pm}W^{\mp}\gamma$ background in the $e^{\pm}\mu^{\mp}\gamma$ SR and that there are smaller contributions from nonprompt photon sources, namely those with photons originating from jets faking photons. The validation and estimation of these backgrounds will be the subject of the next chapter.

$e^{\pm}\mu^{\mp}\gamma$ SR
Leading lepton $p_T > 27\,\text{GeV}$
$E_T^{\text{miss}} > 20\,\text{GeV}$
$\lvert m(e,\gamma) - m_Z \rvert > 5\,\text{GeV}$
N(b-jets) == 0 with 85% b-tag working point

Table 8.1: $e^{\pm}\mu^{\mp}\gamma$ SR definition.

$W^{\pm}W^{\mp}\gamma$	Signal	237.2 ± 2.0
$t\bar{t}\gamma$	prompt γ	398.1 ± 3.1
$Z\gamma$		141.5 ± 14.4
$VZ\gamma$		28.3 ± 0.4
$t\bar{t}$	jet → γ	25.8 ± 1.9
Zjets		11.6 ± 8.5
$\ell\nu\ell\nu$		10.4 ± 1.1
$\ell\ell\ell\nu$	$e \to \gamma$	32.9 ± 1.1
$\ell\ell\ell\ell$		4.3 ± 0.2
Total		890.0 ± 17.3

Table 8.2: Yields in the $e^{\pm}\mu^{\mp}\gamma$ SR. Uncertainty is statistical only.

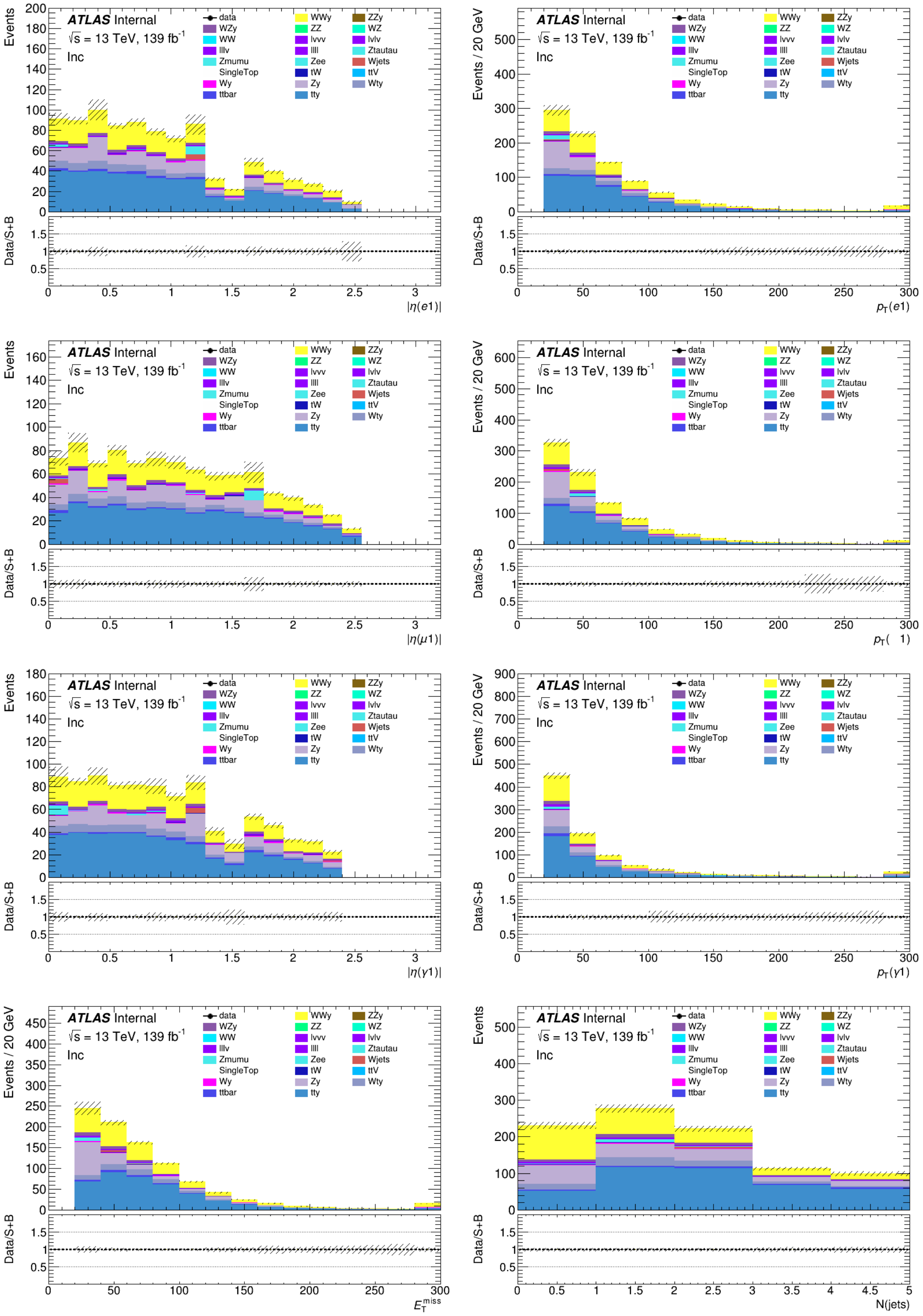

Figure 8.1: Kinematic distributions in the $e^{\pm}\mu^{\mp}\gamma$ SR. Uncertainty is statistical only.

Chapter 9

Background Estimation and Validation

9.1 Estimate of the $t\bar{t}\gamma$ fake process

The largest background to the $W^{\pm}W^{\mp}\gamma$ process is due to $t\bar{t}\gamma$. The most significant difference between $W^{\pm}W^{\mp}\gamma$ and $t\bar{t}\gamma$ is the presence of b-jets in the $t\bar{t}\gamma$ process that are absent in the $W^{\pm}W^{\mp}\gamma$ process. Requiring that all events with a b-tagged jet are vetoed from the $e^{\pm}\mu^{\mp}\gamma$ SR greatly reduces the contribution from $t\bar{t}\gamma$. To select a set of events that is enriched in $t\bar{t}\gamma$ events and does not overlap the set of events selected for the $e^{\pm}\mu^{\mp}\gamma$ signal region, we can require a single b-jet and define the $t\bar{t}\gamma$ control region. The full list of requriements defining the $t\bar{t}\gamma$ control region is given in Table 9.1. Distributions of kinematic variables for the electron, muon, and photon are given in Figure 9.1 and yields for the same region are given in Table 9.2. From the yields, we see that the $t\bar{t}\gamma$ control region requirements select a set of events that is enriched in $t\bar{t}\gamma$ with the other contributions being mostly from $t\bar{t}$.

$t\bar{t}\gamma$ CR
Leading lepton $p_T > 27\,\mathrm{GeV}$
$E_T^{\mathrm{miss}} > 20\,\mathrm{GeV}$
$\lvert m\,(e,\gamma) - m_Z\rvert > 5\,\mathrm{GeV}$
N(b-jets) == 1 with 85% b-tag working point

Table 9.1: $t\bar{t}\gamma$ CR definition.

$W^{\pm}W^{\mp}\gamma$	Signal	17.5 ± 0.6
$t\bar{t}\gamma$	prompt γ	1500.5 ± 6.0
$Z\gamma$		20.5 ± 7.1
$VZ\gamma$		3.6 ± 0.2
$t\bar{t}$	jet → γ	87.5 ± 3.5
$\ell\nu\ell\nu$		1.0 ± 0.3
$\ell\ell\ell\nu$	$e \rightarrow \gamma$	2.2 ± 0.3
$\ell\ell\ell\ell$		0.4 ± 0.1
Total		1633.3 ± 10.0

Table 9.2: Yields in the $t\bar{t}\gamma$ control region. Uncertainty is statistical only.

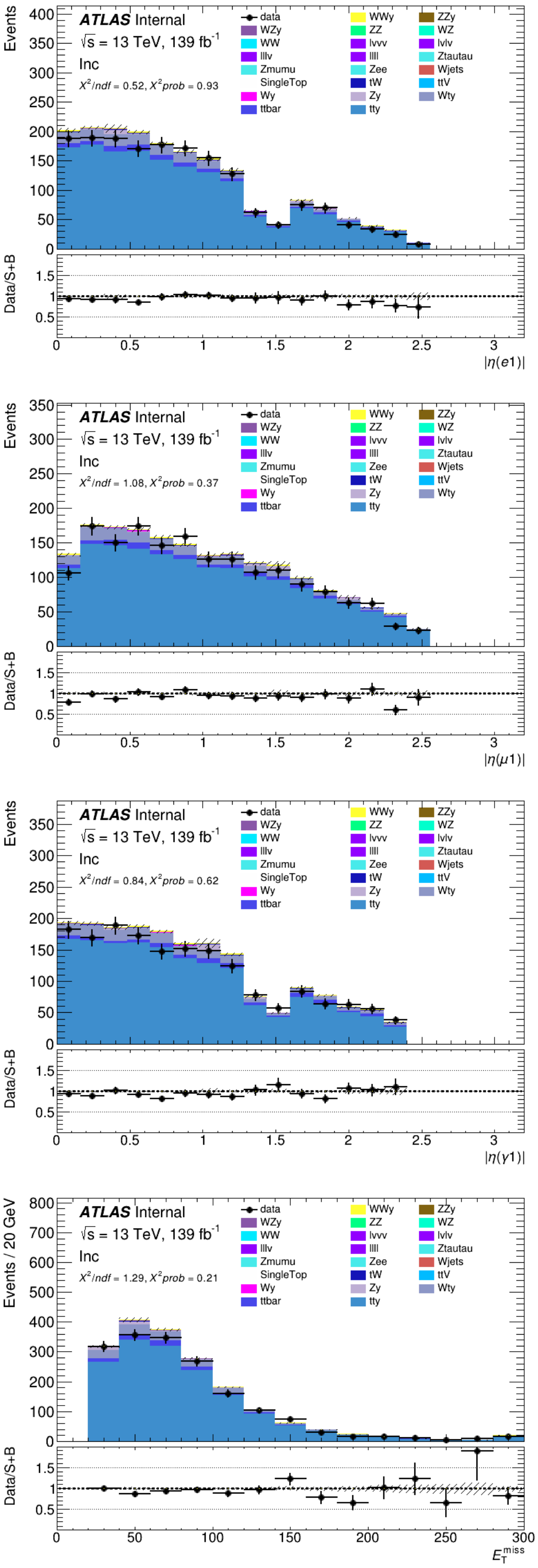

Figure 9.1: Kinematic distributions in the $e^{\pm}\mu^{\mp}\gamma$ SR. Uncertainty is statistical only.

9.2 Estimate of the $Z\gamma$ fake process

The second largest background to the $W^{\pm}W^{\mp}\gamma$ process after $t\bar{t}\gamma$ is due to $Z\gamma$. The leptonic decay of Z bosons is typically characterized by two same-flavor opposite-charge leptons. For $Z\gamma$ to satisfy the $e^{\pm}\mu^{\mp}\gamma$ signal region requirements, the Z boson decays to two tau leptons that in turn decay to an electron muon pair. Requiring the events satisfying the $e^{\pm}\mu^{\mp}\gamma$ signal region requirements have an opposite-charge electron muon pair removes almost all events from $Z\gamma$. To select a set of events that is enriched in $Z\gamma$ events and does not overlap the set of events selected for the $e^{\pm}\mu^{\mp}\gamma$ signal region, we require events to have an opposite-charge same-flavor lepton pair, defining the $Z\gamma$ control region. Since the cross section times branching ratio for the $WZ \rightarrow e^{\pm}\ell^{\pm}\ell^{\mp}$ decay is much smaller than for the $Z \rightarrow \mu^{\pm}\mu^{\mp}$ and $Z \rightarrow e^{\pm}e^{\mp}$ decays, the requirement on the reconstructed electron-photon mass can be dropped. The requirements defining the $Z\gamma$ control region are given in Table 9.3. Distributions of kinematic variables for the leptons and photon are given in Figure 9.2 and yields for the same region are given in Table 9.4. From the yields, we see that the $Z\gamma$ control region requirements select a set of events that is enriched in $t\bar{t}\gamma$ with almost no other contributions.

$Z\gamma$ CR
Leading lepton $p_T > 27\,\text{GeV}$
$E_T^{\text{miss}} > 20\,\text{GeV}$
$m\,(\ell\ell\gamma) < 100\,\text{GeV}$
N(b-jets) == 0 with 85% b-tag working point

Table 9.3: $Z\gamma$ CRs definition.

$W^{\pm}W^{\mp}\gamma$	Signal	41.3 ± 0.8
$t\bar{t}\gamma$	prompt γ	37.3 ± 0.9
$Z\gamma$		24222.9 ± 196.9
$VZ\gamma$		31.7 ± 0.5
Zjets	jet → γ	178.9 ± 53.5
Total		24519.6 ± 204.1

Table 9.4: Yields in the $Z\gamma$ SR. Uncertainty is statistical only.

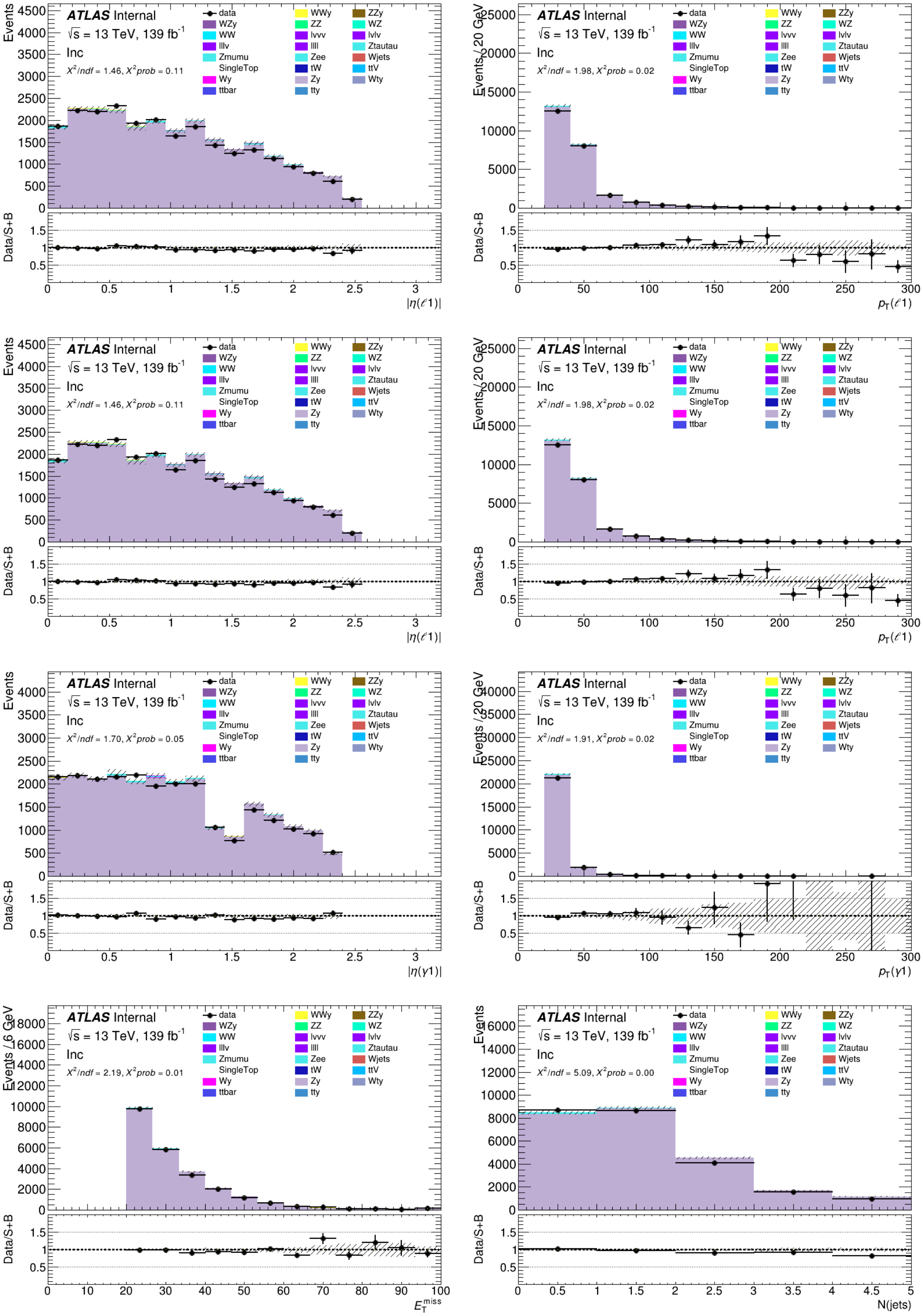

Figure 9.2: Kinematic distributions in the $e^{\pm}\mu^{\mp}\gamma$ SR. Uncertainty is statistical only.

9.3 Estimate of the $e \to \gamma$ fake process

In the $e^{\pm}\mu^{\mp}\gamma$ signal region, it is possible for electrons to either be reconstructed as photons or the electron can radiate a photon and only the photon is reconstructed. Events where this occurs are referred to as $e \to \gamma$ fake events. In MC simulation, events arise from the $e \to \gamma$ fake process if there is an electron at truth level or if there is a truth electron that is not reconstructed within $\Delta R < 1.0$ of the photon. The events selected from MC simulation in the $e^{\pm}\mu^{\mp}\gamma$ signal region as well as those that are removed by the Z veto, $|m(e\gamma) - m(Z)| < 5\,\text{GeV}$ requirement are given in Table 9.5. From the yields, we can see that the majority of the events that arise from the $e \to \gamma$ fake process originate from diboson (VV) processes and that the Z veto is very efficient at removing these events from the $e^{\pm}\mu^{\mp}\gamma$ signal region.

process	Region	
	$e^{\pm}\mu^{\mp}\gamma$ SR	VV CR
$t\bar{t}$	2.6 ± 0.6	0.4 ± 0.2
Zjets	1.0 ± 0.7	2.0 ± 2.0
$\ell\ell\ell\ell$	3.9 ± 0.2	8.1 ± 0.3
$\ell\ell\ell\nu$	30.5 ± 1.1	71.3 ± 2.2
Total	39.3 ± 1.3	82.54 ± 3.0

Table 9.5: Yields identified as arising from the $e \to \gamma$ fake process in MC simulation in the $e^{\pm}\mu^{\mp}\gamma$ signal region and the diboson control region. Uncertainty is statistical only.

9.3.1 $e \to \gamma$ fake estimate

The $e \to \gamma$ fake background is estimated using MC simulation that has been corrected by data driven MC correction scale factors. The correction scale factors are derived in the $Z \to e^{\pm}e^{\mp}$ and $Z \to e^{\pm}\gamma$ control regions defined in Table 9.6. The $Z \to e^{\pm}e^{\mp}$ control region is designed to be enriched in events from $Z \to e^{\pm}e^{\mp}$ and the $Z \to e^{\pm}\gamma$ control region is designed to be enriched in events from $Z \to e^{\pm}e^{\mp}$ where one of the photons is reconstructed as a photon.

MC correction scale factors are obtained by taking the ratio of the $e \to \gamma$ fake rate (FR)

$Z \to e^{\pm}e^{\mp}$ CR	$Z \to e^{\pm}\gamma$ CR
$N(e) == 2$ $N(\gamma) == 0$ $\lvert m(ee) - m(Z) \rvert \leq 30\,\mathrm{GeV}$	$N(e) == 1$ $N(e) == 1$ $\lvert m(e\gamma) - m(Z) \rvert \leq 30\,\mathrm{GeV}$
Leading e $p_{\mathrm{T}} > 27\,\mathrm{GeV}$ $N(b\text{-jets}) == 0$	

Table 9.6: Definitions for the $Z \to e^{\pm}e^{\mp}$ and $Z \to e^{\pm}\gamma$ control regions used to measure the $e \to \gamma$ fake MC correction scale factors.

measured in MC and scaling this to match the fake rate measured in data:

$$\mathrm{SF} = \frac{\mathrm{FR}_{\mathrm{Data}}}{\mathrm{FR}_{MC}} \tag{9.1}$$

This means that if the MC simulation predicts that 1 event enters the $e^{\pm}\mu^{\mp}\gamma$ signal region through the $e \to \gamma$ fake process but the $e \to \gamma$ fake rate in MC simulation is half of the $e \to \gamma$ fake rate in data, we need to scale the predicted number of $e \to \gamma$ fake events by 2 to get an accurate estimate. The $e \to \gamma$ fake rates are measured in the $Z \to e^{\pm}e^{\mp}$ and $Z \to e^{\pm}\gamma$ control regions defined in Table 9.6 and are given by

$$\mathrm{FR} = \frac{N(e^{\pm}e^{\mp})}{N(e^{\pm}\gamma)} \tag{9.2}$$

as a function of the photon p_{T} and η. The binning used is $p_{\mathrm{T}}(\gamma) = \{20, 25, 35, 45, 60\}$ GeV and $|\eta(\gamma)| = \{0, 0.5, 1.0, 1.52, 2.0, 2.37\}$. Since the analysis does not consider electrons and photons in the crack region ($1.37 < |\eta| < 1.52$), scale factors for this η range are also not considered.

The number of Z and non-Z events are determined by making use of the fact that the $m(e^{\pm}e^{\mp})$ distribution in the $Z \to e^{\pm}e^{\mp}$ control region and the $m(e^{\pm}\gamma)$ distribution in the $Z \to e^{\pm}\gamma$ control region have different shapes for Z and non-Z processes. The Z process is modeled by Breit-Wigner distribution convoluted with a crystal ball and the non-Z events are modeled by a 4^{th} order Bernstein polynomial. The width of the Breit-Wigner is fixed to the Z width and the mean of the Crystal Ball is fixed to 0, but all other model parameters are free in the fit. After fitting the parameterized distributions to the $m(e^{\pm}e^{\mp})$ and $m(e^{\pm}\gamma)$ distributions in MC simulation and data and integrating the result, results in the measurement of the number of Z and non-Z events.

Figure 9.3 shows an example of the resulting fit in the $Z \to e^{\pm}e^{\mp}$ and $Z \to e^{\pm}\gamma$ control regions using MC simulation and data. The distribution of events from Z decay are given by the curve labeled "Signal" and the distribution of other processes are given by the curve labeled "Background." Comparing the sum of the two curves, labeled "Total" in the figure, to data shows good agreement, indicating that the parametric models successfully model the two distributions.

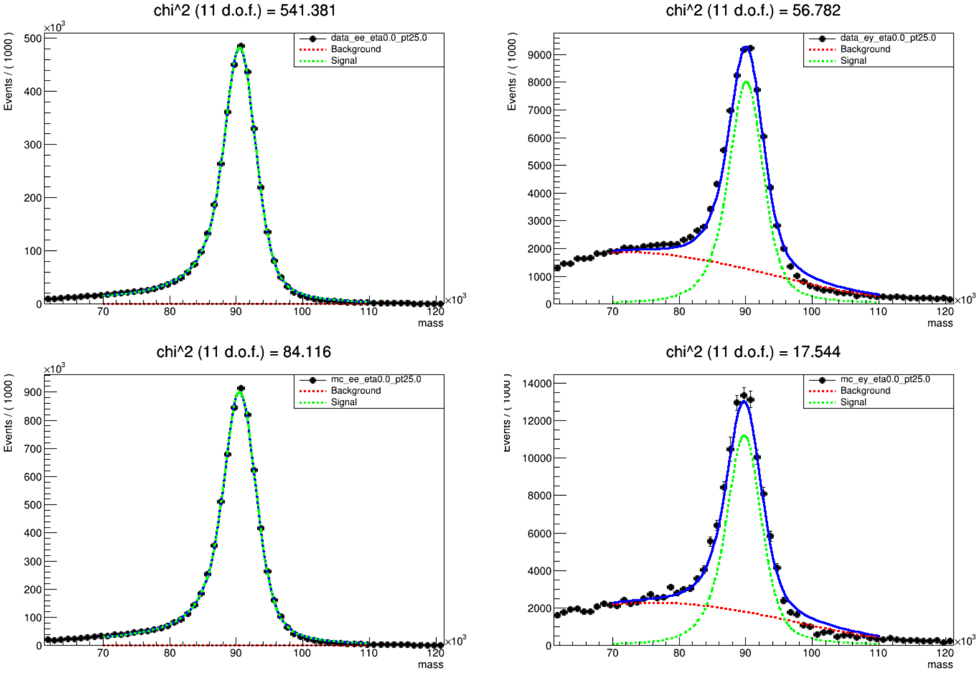

Figure 9.3: Result of performing the template fit described in the text. (Top Left) Template performed in the $Z \to e^{\pm}e^{\mp}$ control region using data. (Top right) Template performed in the $Z \to e^{\pm}e^{\mp}$ control region using MC. (Bottom Left) Template performed in the $Z \to e^{\pm}\gamma$ control region using data. (Bottom Right) Template performed in the $Z \to e^{\pm}\gamma$ control region using MC.

The MC correction scale factors obtained using Equation 9.2, Equation 9.1, and the measured number of events arising from Z decay are given in Table 9.7.

$e \to \gamma$ scale factors

		η					
		0 - 0.5	0.5 - 1.0	1.0 - 1.37	1.37 - 1.52	1.52 - 2.0	2.0 - 2.37
p_{T}[GeV]	above 60	1.32	0.98	1.11	-	0.95	0.98
	45 - 60	1.24	1.06	1.05	-	0.90	1.05
	35 - 45	1.25	1.09	1.05	-	0.98	1.06
	25 - 35	1.12	1.25	1.22	-	0.81	0.98
	20 - 25	0.70	1.13	1.19	-	0.96	1.01

Table 9.7: Measured $e \to \gamma$ scale factors.

9.3.2 Systematic uncertainties

Several systematic uncertainties on the $e \to \gamma$ fake estimate are considered. The number of events in the $Z \to e^{\pm}e^{\mp}$ and $Z \to e^{\pm}\gamma$ control regions obtained by the template fit are varied up and down by the uncertainty on the measured number of events to produce alternative $e \to \gamma$ fake estimates. When the template fit is performed, assumptions are made about the shape of the background distribution. To include the effect of these assumptions on the $e \to \gamma$ fake estimate, new MC correction scale factors are produced after replacing the 4^{th} order Bernstein polynomial with a 5^{th} order Bernstein polynomial. An assumption is also made about what events should be considered in the template fit. Nominally, only events with $m(ee)$ or $m(e\gamma)$ within 30 GeV of the Z mass are considered. To account for this choice, additional $e \to \gamma$ fake MC correction scale factors are produced after increasing and decreasing the distance from the Z mass by 5 GeV. The variations on the $e \to \gamma$ fake estimate are propagated through the remainder of the analysis and taken into account when the measurement of the $W^{\pm}W^{\mp}\gamma$ signal strength is performed.

9.3.3 Validation of the $e \to \gamma$ fake estimate

Contributions to the $W^{\pm}W^{\mp}\gamma$ background in the $e^{\pm}\mu^{\mp}\gamma$ signal region from the $e \to \gamma$ fake process are small due to the efficiency of the Z veto, $|m(e,\gamma) - m(Z)| < 5\,\mathrm{GeV}$. Inverting this requirement selects a set of events that are enriched in $e \to \gamma$ fake events that are orthogonal to the events selected by the $e^{\pm}\mu^{\mp}\gamma$ signal region requirements. The new region is referred to as the diboson control region or the VV control region. The full list of requirements defining the diboson control region are given in Table 9.8. Distributions of kinematic variables for the electron, muon, and photon are given in Figure 9.4 and yields for the same region are given in Table 9.9. The $e \to \gamma$ and jet $\to \gamma$ processes have been corrected using data driven MC correction scale factors have been applied to correct for mis-modeling between data and the MC prediction. The jet $\to \gamma$ data driven MC correction scale factors are derived in a similar way to the $e \to \gamma$ fake MC correction scale factors and will be discussed in the next section. The agreement between data and the estimate provided by MC simulation is reasonable given the uncertainties on the backgrounds, suggesting that our estimate for the $e \to \gamma$ process is sufficient.

VV CR
Leading lepton $p_T > 27\,\mathrm{GeV}$
$E_T^{\mathrm{miss}} > 20\,\mathrm{GeV}$
$\lvert m(e,\gamma) - m_Z \rvert < 5\,\mathrm{GeV}$
N(b-jets) == 0 with 85% b-tag working point

Table 9.8: VV CR definition.

$W^{\pm}W^{\mp}\gamma$	15.10 ± 0.75
$VZ\gamma$	2.44 ± 0.52
$Z\gamma$	3.56 ± 2.47
$t\bar{t}\gamma$	31.06 ± 3.41
jet $\to \gamma$	3.86 ± 1.52
$e \to \gamma$	88.52 ± 6.48
Total	144.54 ± 8.53
data	146

Table 9.9: Yields in the diboson control region. Uncertainty includes statistical uncertainties as well as all systematic uncertainties included in this analysis presented in this thesis.

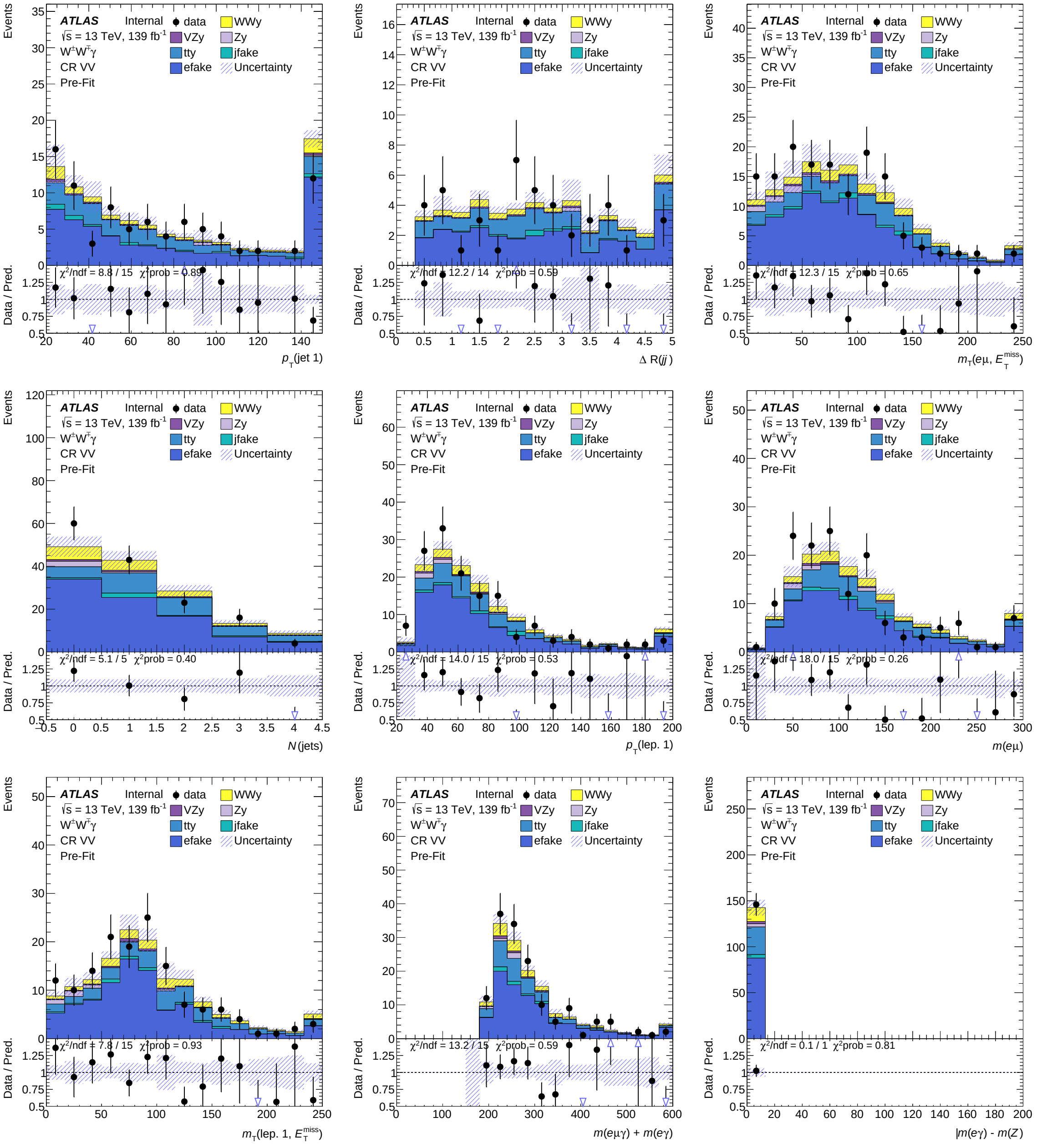

Figure 9.4: Distributions of various variables for events in the diboson control region. The uncertainties indicated in the figures includes statistical uncertainties as well as all systematic uncertainties included in this analysis presented in this thesis.

9.4 Estimate of the jet → γ fake process

Events where the photon arises due to hadronic decay or where a jet is mis-identified as a photon are refereed to as jet → γ fake events or jet fakes throughout this thesis and are a background to the $W^{\pm}W^{\mp}\gamma$ process. The contribution from events arising from the jet → γ fake process is estimated by applying data-driven MC correction scale factors calculated in a region enriched in jet → γ events to the MC estimate for the jet → γ process.

9.4.1 Origin of jet → γ events

Events entering the $e^{\pm}\mu^{\mp}\gamma$ SR from jet → γ fakes originate from processes similar the signal and backgrounds with prompt photons ($t\bar{t}\gamma$, $Z\gamma$, $W^{\pm}W^{\mp}\gamma$, and $W^{\pm}Z\gamma$) except that there is no prompt photon ($t\bar{t}$, Zjets, and VV). MC samples for processes without a prompt photon are used to estimate the contribution from jet → γ fakes. Sample overlap removal is applied between the prompt and non-prompt MC samples so that these samples are orthogonal and events where the photon arises from ISR or FSR are contained in the prompt photon samples (e.g. $t\bar{t}\gamma$) and photons arising from other sources are contained in the other sample ($t\bar{t}$). The yields for the samples used for the jet → γ fake estimate before any scale factors have been applied are given in Table 9.10. The generators used to produce each MC estimate can affect how well the MC models the jet → γ fake process and are indicated in Table 9.11.

Process	Yield
$t\bar{t}$	23.0 ± 1.8
$\ell\ell\ell\ell$	0.4 ± 0.1
$\ell\ell\ell\nu$	2.3 ± 0.3
$\ell\nu\ell\nu$	10.4 ± 1.1
Zjets	10.4 ± 8.5
Total	46.7 ± 8.7

Table 9.10: Yields for the jet → γ background in the $e^{\pm}\mu^{\mp}\gamma$ SR. Uncertainty is statistical only.

jet → γ Process	Type	Generator
$t\bar{t}$	Heavy flavor	POWHEG-BOX v2 +PYTHIA 8.230
tW		POWHEG-BOX v2 +PYTHIA 8.230
Zjets	Light flavor	SHERPA 2.2.2
VV		SHERPA 2.2.1

Table 9.11: Summary of the processes used estimate the jet → γ fake contribution as well as the generator used to produce the sample.

9.4.2 jet → γ estimate in the Zjets control region

Contributions to the $W^{\pm}W^{\mp}\gamma$ background in the $e^{\pm}\mu^{\mp}\gamma$ signal region from the jet → γ fake process are small but this is not due to any specific requirement so there is not an easy way to form a jet → γ fake control region near the $e^{\pm}\mu^{\mp}\gamma$ signal region. Instead, we note that the requirement that $m(\ell\ell\gamma) < 100\,\text{GeV}$ defining the $Z\gamma$ control region is used to veto jet → γ fake events. The Zjets control region is defined by inverting the $m(\ell\ell\gamma)$ requirement of the $Z\gamma$ control region. The full list of requirements defining the diboson control region are given in Table 9.12.

Zjets CR
Leading lepton $p_T > 27\,\text{GeV}$
$E_T^{\text{miss}} > 20\,\text{GeV}$
$m\,(\ell\ell\gamma) > 100\,\text{GeV}$
N(b-jets) == 0 with 85% b-tag working point

Table 9.12: Zjets CRs definition.

Assuming that the mechanism that causes jets to fake photons is independent of the flavor of the leptons in the event, the jet → γ fake process can be studied in a region with two same-flavor opposite-sign leptons and be extrapolated to the signal region with a $\ell^{\pm}\ell^{\mp}$ pair. Data-driven MC correction scale factors are measured as a function of the photon p_{T} and η by taking the ratio of the number of events in MC simulation to the number of events

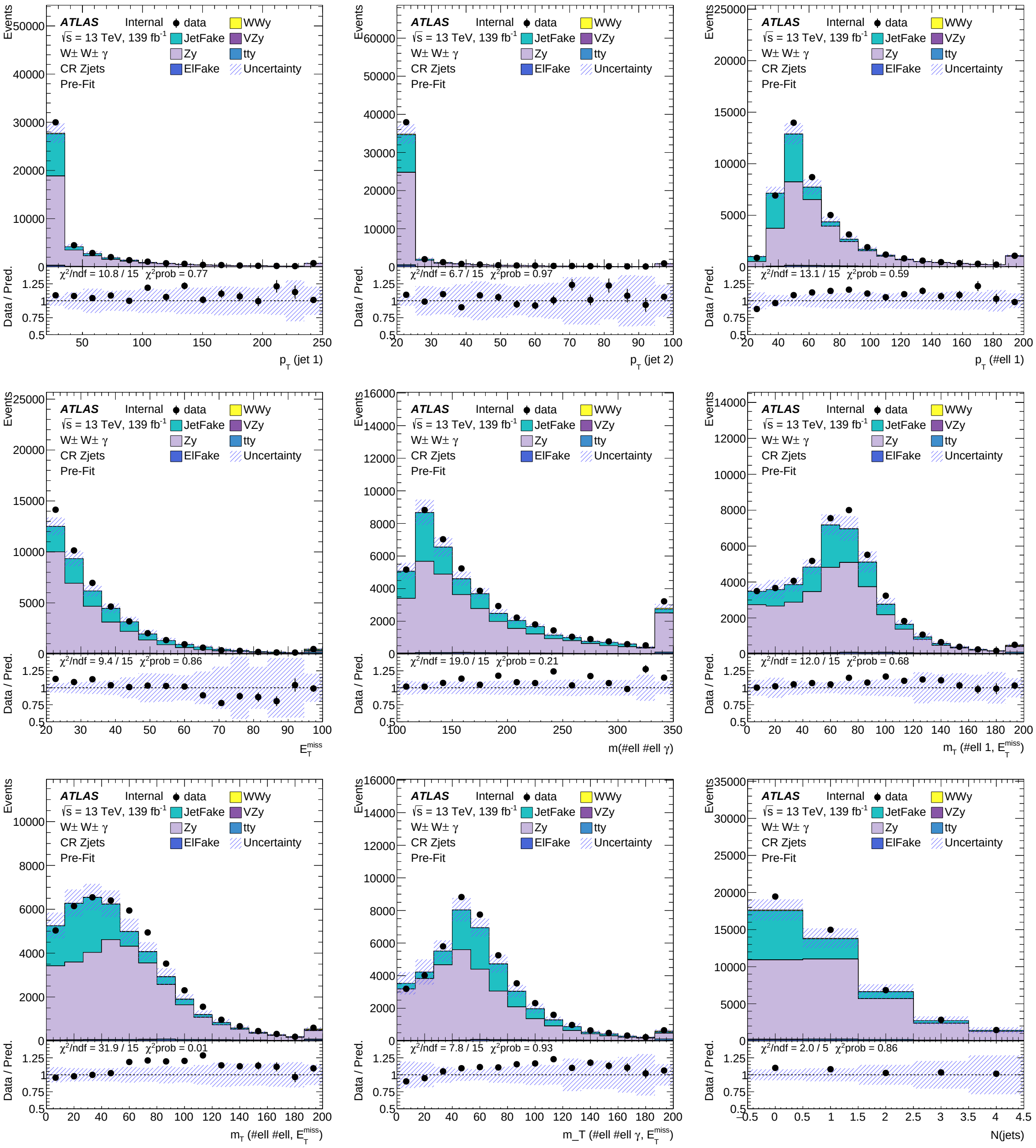

Figure 9.5: Distributions of various variables for events in the Zjets control region. The uncertainties indicated in the figures includes statistical uncertainties as well as all systematic uncertainties included in this analysis presented in this thesis.

in data:

$$SF = \frac{N(\text{Data}) - N(\text{prompt MC})}{N(\text{jet} \to \gamma \text{ MC})}$$

The measured jet $\to \gamma$ MC correction scale factors are given in Figure 9.6.

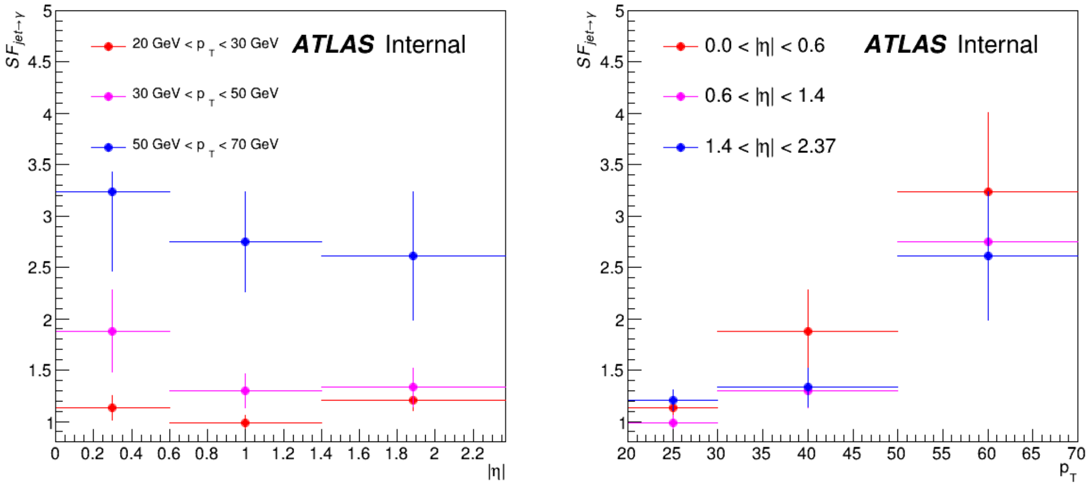

Figure 9.6: Data-driven jet → γ fake MC correction scale factors calculated in the Zjets CR. The uncertainty is statistical only.

9.4.3 jet → γ systematic uncertainties

The systematic uncertainties applied to the jet → γ fake estimate include:

- The statistical uncertainty on the jet → γ MC correction SFs
- A 30% overall uncertainty estimated from an alternative method for estimating contributions from jet → γ events.

To account for potential differences between flavor/generator, uncertainties are applied separately to light flavor/Sherpa (Zjets, VV) and heavy flavor/MadGraph ($t\bar{t}$, tW) and uncorrelated.

9.4.4 Validation of the jet → γ fake estimate

Distributions of kinematic variables for the electron, muon, and photon are given in Figure 9.7 and yields for the same regions are given in Table 9.13. From the figures and yields, we see that the Zjets control region has approximately of the 50% events from the $Z\gamma$ process and 50% of the events from the jet → γ fake (Zjets in this case) process. Since the modeling of the $Z\gamma$ process is validated in the $Z\gamma$ CR, we can consider any mis-modeling in the Zjets control region to be the result of mis-modeling in the jet → γ fake process. The $e \to \gamma$ and jet → γ processes have been corrected using data driven MC correction scale factors which have been applied to correct for mis-modeling between data and the MC prediction. The $e \to \gamma$ data driven MC correction scale factors are derived in a similar way to the jet → γ fake MC correction scale factors as discussed in the previous section. The agreement between data and the estimate provided by MC simulation is reasonable given the uncertainties on the backgrounds, suggesting that our estimate for the jet → γ process is sufficient.

$W^{\pm}W^{\mp}\gamma$	275.74 ± 12.36
$VZ\gamma$	108.67 ± 22.11
$Z\gamma$	30397.30 ± 3250.70
$t\bar{t}\gamma$	393.11 ± 34.52
jet → γ	14011.90 ± 5276.79
$e \to \gamma$	404.48 ± 29.89
Total	45591.20 ± 6352.26
data	45570

Table 9.13: Yields in the Zjets control region. Uncertainty includes statistical uncertainties as well as all systematic uncertainties included in this analysis presented in this thesis.

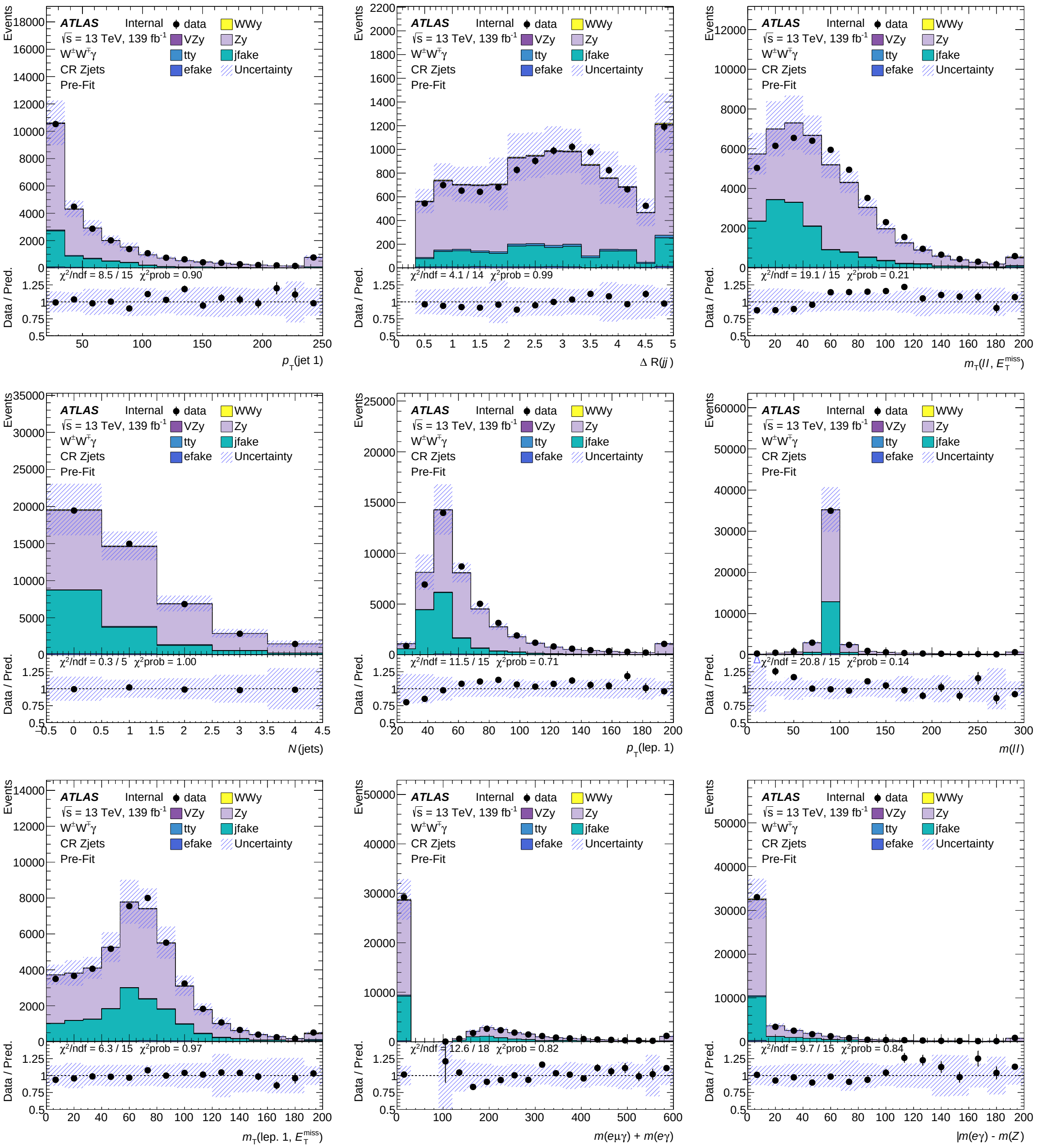

Figure 9.7: Distributions of various variables for events in the Zjets control region after the MC correction scale discussed in this section have been applied. The uncertainties indicated in the figures includes statistical uncertainties as well as all systematic uncertainties included in this analysis presented in this thesis.

Chapter 10

Machine Learning

To increase the sensitivity of the analysis, a Boosted Decision Tree (BDT) algorithm is used to combine information from many different variables to produce a new variable (the BDT output) to use during the fitting procedure. The BDT is trained using the `XGBoost` [92] package using events in the $e^{\pm}\mu^{\mp}\gamma$ signal region. To produce the BDT output that will be used during fitting, the BDT is applied to events in the $e^{\pm}\mu^{\mp}\gamma$ signal region.

The remainder of the section defines the events used to train the BDT, the variables for each event, the BDT hyperparameters, and the validation of the BDT.

10.1 `XGBoost` Hyperparameters

`XGBoost` has several hyperparameters that can be set to create different models. This section describes the hyperparameters that are used to define the BDT for this analysis.

- **Max tree depth**

  The maximum tree-depth determines the maximum number of splits (set of sequential cuts) that each tree can achieve during the training. Increasing the maximum depth increases the model complexity.

- **L2 Regularization**

The L2 regularization is used to add a regularization term to the function to be optimized. If the L2 regularization value is non-zero, an additional term is added to the function to be minimized during the training of the form:

$$\frac{1}{2}L2 \cdot \boldsymbol{w}^{\mathrm{T}}\boldsymbol{w}$$

where $\boldsymbol{w}$ is the vector of weights for each tree. This term penalizes models with large weights and helps to effectively reduce the model complexity.

- **Number of trees**

  The number of trees used in the training. Increasing the number of trees increases the model complexity.

- **Learning Rate**

  The learning rate multiplies the gradient after each training step. This reduces the impact of each event in the optimization process.

- **Event subsample**

  The event subsample is the fraction of events used by each tree during training.

- **Variable subsample**

  The variable subsample is the fraction of variables that each tree can use.

- **Min child weight**

  The min child weight is the smallest number of events that can exist in a leaf node.

These parameters define the BDT complexity.

10.2 Processes used when training the BDT

The BDT is trained using events from Monte Carlo simulation. The $t\bar{t}\gamma$ and $Z\gamma$ backgrounds used to train the BDT are not scaled using the $t\bar{t}\gamma$ and $Z\gamma$ normalization factors measured in Section 11. The $e \to \gamma$ and jet $\to \gamma$ background estimates are scaled by the MC correction scale factors described in Section 9.3.1 and Section 9.4.2, respectively.

Background	Type
$W^{\pm}W^{\mp}\gamma$	MC
$Wt\gamma$	
$VZ\gamma$	
$t\bar{t}\gamma$	
$Z\gamma$	
jet $\to \gamma$	Scaled MC
$e \to \gamma$	

Table 10.1: Summary of the processes used to train the BDT as well as the type of estimate used.

10.3 Event weights used for training

Events with negative weights are used in the BDT training. However, the absolute value of the event weights are used and then signal and background processes are re-weighted to their expected number of events. The event weight used during training is given by:

$$w_i^{\text{new}} = |w_i| \cdot \frac{\sum_i w_i}{\sum_i |w_i|}$$

Taking the absolute value of the event weights can cause the shape of the distribution of variables used to train the BDT to change. .

Additionally, an extra scale factor is applied to the background events, such that the total number of background events is equal to the number of signal events. Since there are more background events than signal events, this prevents the BDT from assigning a low BDT score to signal events. For example, if there were 99 background events and 1 signal event, the BDT could obtain 99% accuracy by labelling all signal events as background.

10.4 Obtaining the BDT output

Before training, each event is assigned a random number between 1 and 5. Based on the random number, events used to train the BDT are split into five folds. Each BDT is trained on $\frac{5-1}{5} \cdot 100\% = 80\%$ of the events and applied to the remaining 20% of the events. This procedure is repeated five times. The BDT score obtained by applying the BDT to events not used to train the BDT is used to perform the likelihood fit described in Chapter 11. This procedure ensures that the analysis does not suffer from bias when applying the BDT to events used in training.

10.5 Hyperparameter tuning

Each BDT is trained such that the area under the ROC (Receiver operating characteristic) curve, referred to as the AUC, is optimized. The ROC curve is obtained using the BDT output to calculate the probability that each event in a given set is a signal or background and plot the true positive rate against the false-positive rate. These rates are defined as follows:

$$\begin{aligned}\text{True Positive Rate} &= \frac{\text{True Positives}}{\text{True Positives} + \text{False Negatives}} \\ \text{False Positive Rate} &= \frac{\text{False Positives}}{\text{False Positives} + \text{True Negatives}}\end{aligned}$$

Integrating the ROC curve yields the AUC, which has a probabilistic interpretation: the AUC is the probability that a randomly selected signal event will have a higher BDT score than a randomly selected background event. So, the larger the AUC, the better the training will be. The AUC is a substitute for the expected significance. Since the AUC does not consider systematic uncertainties, a higher AUC does not necessarily imply a higher expected significance.

10.6 Feature Importance

The feature importance of a variable is defined as the improvement in accuracy due to that variable. It is calculated by averaging the relative improvement in purity due to splitting on a variable over all trees defining the model. This quantity is used to understand which variables contribute the most to separating signal and background.

10.7 Variable Selection

The BDT is trained using ten variables. The variables used to train the BDT are selected using the algorithm described next. When training a BDT with n variables, the n variables are selected by first training the BDT using m variables such that $m > n$, ranking the variables by feature importance, removing the variable with the lowest feature importance, and then repeating until there are only n variables left. Note: when variables are being selected, the model hyperparameters: event subsample, and column subsample, are set to 1. This helps to prevent highly correlated variables from being selected.

10.8 $e^{\pm}\mu^{\mp}\gamma$ Signal Region Training

This section describes the hyperparameters used to define the BDT, the input variables, and the validation of the BDT and input variables by applying the BDT to a control region and comparing the results with data.

The hyperparameters used to define the BDT are given in Table 10.2. A description of each of the hyperparameters is given in Section 10.1.

10.8.1 BDT Training Variables

The variables used to train the BDT in the $e^{\pm}\mu^{\mp}\gamma$ signal region as well as the feature importance of each variable for a single BDT are given in Table 10.1. The correlation between

Parameter	Value
max tree depth	4
L2 regularization	1
Number of trees	120
learning rate	0.1
event subsample	0.5
variable subsample	0.5
min child weight	1

Table 10.2: The hyperparameters used to define the BDT trained in the $e^{\pm}\mu^{\mp}\gamma$ signal region.

the input variables for the signal events can be seen in Table 10.3 and the correlation between the input variables for the background events can be seen in Table 10.4.

variable	feature importance
p_{T}(jet 1)	0.19
ΔR(jet 1, jet 2)	0.13
$m_{\mathrm{T}}(e\mu)$	0.11
N(jets)	0.11
$p_{\mathrm{T}}(\ell\ 1)$	0.10
$m(e\mu)$	0.09
$m_{\mathrm{T}}(\ell\ 1)$	0.08
$m(e\mu\gamma) + m(e\gamma)$	0.07
$\lvert m(e\gamma) - m(Z)\rvert$	0.06
$m(e\mu\gamma)$	0.06

Figure 10.1: Variables used to train the BDT in the $e^{\pm}\mu^{\mp}\gamma$ signal region and each variables feature importance for the one BDT.

Description of variables used in the training:

njets is the number of jets passing the jets selection criteria in the event.

p_T(jet 1) is the transverse momentum of the jet with the largest transverse momentum in the event. If there are no jets in the event, p_T(jet 1) is set to -99. The BDT can use this as a flag indicating that the event has no jets.

$\boldsymbol{p_T}$**(lep 1)** is the transverse momentum of the lepton (e or μ) with the largest transverse momentum in the event.

$\boldsymbol{m(e\mu)}$ is the mass of the sum of the 4-vectors of the two leptons in the event.

$\boldsymbol{m(e\mu\gamma)}$ is the mass of the sum of the lepton and photon 4-vectors.

$\boldsymbol{m(e\mu\gamma) + m(e\gamma)}$ is the sum $m(e\mu\gamma)$ and $m(e\gamma)$. Each mass term represents the mass of the object resulting from adding the indicated objects 4-vectors.

$\boldsymbol{|m(e\gamma) - m(Z)|}$ is the absolute difference between $m(e\gamma)$ and 90 GeV. $m(e\gamma)$ is the mass of the object resulting from adding the electron and photon 4-vectors.

$\boldsymbol{m_T(\ell 1, E_T^{\mathbf{miss}})}$ is the transverse mass of the 4-vector sum of the lepton (e or μ) with the largest transverse momentum in the event and E_T^{miss}.

$\boldsymbol{m_T(e\mu, E_T^{\mathbf{miss}})}$ is the transverse mass of two leptons in the event and E_T^{miss} 4-vectors.

$\boldsymbol{\Delta R(jj)}$ is the ΔR between the two leading jets in the event. If there are 0 or 1 jets in the event, $\Delta R(jj)$ is set to -99. The BDT can use this variable as a flag that indicates that the event has 0 or 1 jets.

N(jets)	1.00	0.04	0.05	0.58	0.15	0.03	0.07	0.08	0.83	0.06
$m_{\mathrm{T}}(\ell 1, E_{\mathrm{T}}^{\mathrm{miss}})$	0.04	1.00	0.91	0.04	0.61	0.43	0.35	0.29	0.03	0.12
$m_{\mathrm{T}}(e\mu, E_{\mathrm{T}}^{\mathrm{miss}})$	0.05	0.91	1.00	0.06	0.52	0.25	0.23	0.20	0.04	0.10
$p_{\mathrm{T}}(\mathrm{jet1})$	0.58	0.04	0.06	1.00	0.29	0.07	0.12	0.13	0.49	0.10
$p_{\mathrm{T}}(\ell 1)$	0.15	0.61	0.52	0.29	1.00	0.73	0.72	0.66	0.13	0.41
$m(e\mu)$	0.03	0.43	0.25	0.07	0.73	1.00	0.79	0.66	0.02	0.31
$m(e\mu\gamma)$	0.07	0.35	0.23	0.12	0.72	0.79	1.00	0.96	0.06	0.69
$m(e\mu\gamma) + m(e\gamma)$	0.08	0.29	0.20	0.13	0.66	0.66	0.96	1.00	0.07	0.83
$\Delta R(jj)$	0.83	0.03	0.04	0.49	0.13	0.02	0.06	0.07	1.00	0.06
$\lvert m(e\gamma) - m(Z)\rvert$	0.06	0.12	0.10	0.10	0.41	0.31	0.69	0.83	0.06	1.00
	N(jets)	$m_{\mathrm{T}}(\ell 1, E_{\mathrm{T}}^{\mathrm{miss}})$	$m_{\mathrm{T}}(e\mu, E_{\mathrm{T}}^{\mathrm{miss}})$	$p_{\mathrm{T}}(\mathrm{jet1})$	$p_{\mathrm{T}}(\ell 1)$	$m(e\mu)$	$m(e\mu\gamma)$	$m(e\mu\gamma) + m(e\gamma)$	$\Delta R(jj)$	$\lvert m(e\gamma) - m(Z)\rvert$

Table 10.3: Correlation between input variables used to train the BDT for the signal events in the $e^{\pm}\mu^{\mp}\gamma$ signal region.

N(jets)	1.00	0.04	0.05	0.52	0.11	0.07	0.06	0.05	0.81	0.06
$m_{\mathrm{T}}(\ell 1, E_{\mathrm{T}}^{\mathrm{miss}})$	0.04	1.00	0.90	0.00	0.59	0.44	0.30	0.24	0.05	0.10
$m_{\mathrm{T}}(e\mu, E_{\mathrm{T}}^{\mathrm{miss}})$	0.05	0.90	1.00	0.01	0.50	0.29	0.21	0.18	0.06	0.08
$p_{\mathrm{T}}(\mathrm{jet1})$	0.52	0.00	0.01	1.00	0.20	0.04	0.06	0.06	0.44	0.07
$p_{\mathrm{T}}(\ell 1)$	0.11	0.59	0.50	0.20	1.00	0.69	0.67	0.61	0.10	0.38
$m(e\mu)$	0.07	0.44	0.29	0.04	0.69	1.00	0.74	0.61	0.07	0.27
$m(e\mu\gamma)$	0.06	0.30	0.21	0.06	0.67	0.74	1.00	0.96	0.05	0.68
$m(e\mu\gamma) + m(e\gamma)$	0.05	0.24	0.18	0.06	0.61	0.61	0.96	1.00	0.04	0.80
$\Delta R(jj)$	0.81	0.05	0.06	0.44	0.10	0.07	0.05	0.04	1.00	0.04
$\lvert m(e\gamma) - m(Z)\rvert$	0.06	0.10	0.08	0.07	0.38	0.27	0.68	0.80	0.04	1.00
	N(jets)	$m_{\mathrm{T}}(\ell 1, E_{\mathrm{T}}^{\mathrm{miss}})$	$m_{\mathrm{T}}(e\mu, E_{\mathrm{T}}^{\mathrm{miss}})$	$p_{\mathrm{T}}(\mathrm{jet1})$	$p_{\mathrm{T}}(\ell 1)$	$m(e\mu)$	$m(e\mu\gamma)$	$m(e\mu\gamma) + m(e\gamma)$	$\Delta R(jj)$	$\lvert m(e\gamma) - m(Z)\rvert$

Table 10.4: Correlation between input variables used to train the BDT for the background events in the $e^{\pm}\mu^{\mp}\gamma$ signal region.

Overlay plots comparing signal and background distributions of the input variables used to train the BDT are shown in Figure 10.2. Stacked plots of each input variable used to train the BDT are shown in Figure 10.3. The BDT output distribution is given in Figure 10.4

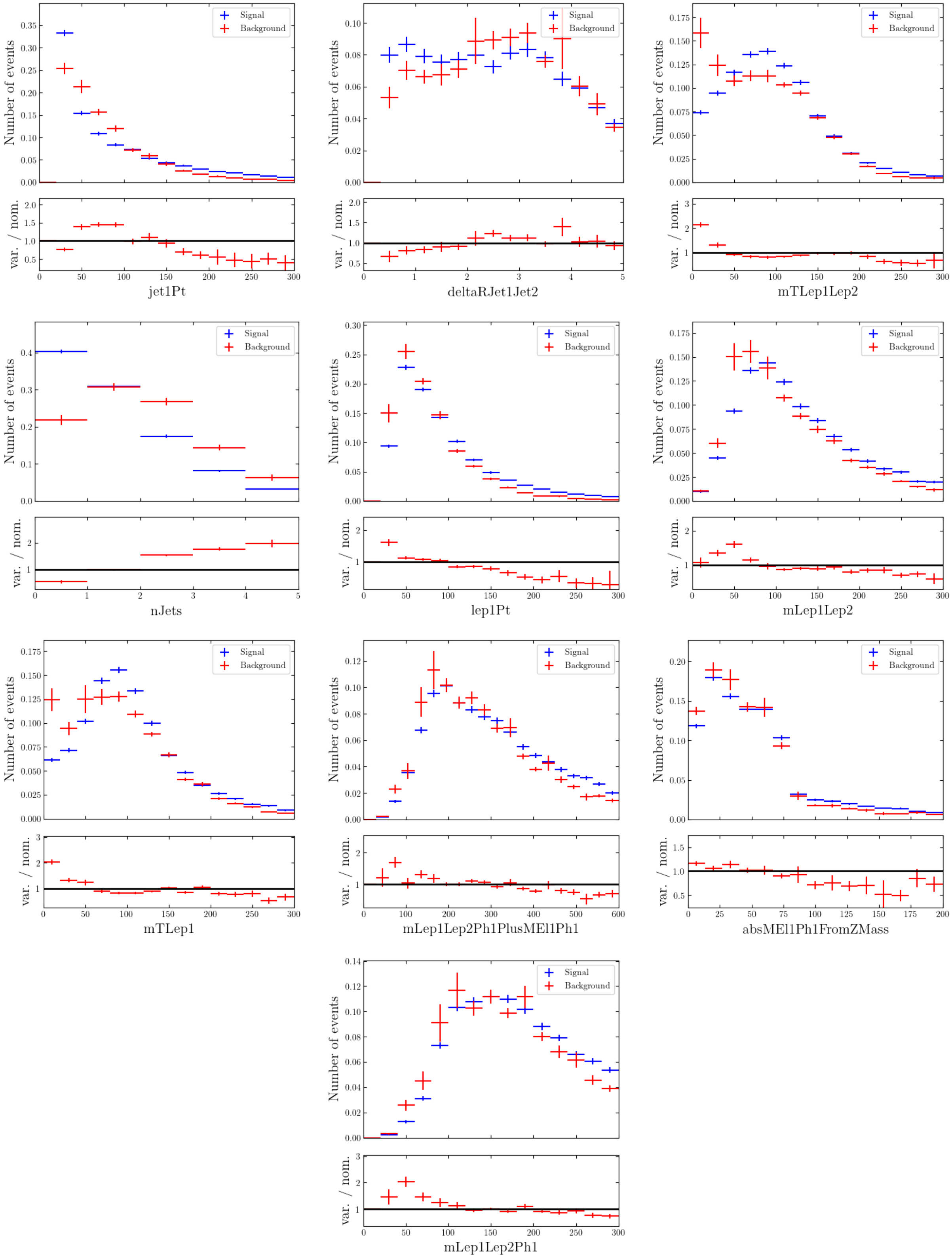

Figure 10.2: Shape comparison between signal and backgrounds for the variables used to train the BDT in the $e^{\pm}\mu^{\mp}\gamma$ signal region. Uncertainty is statistical only.

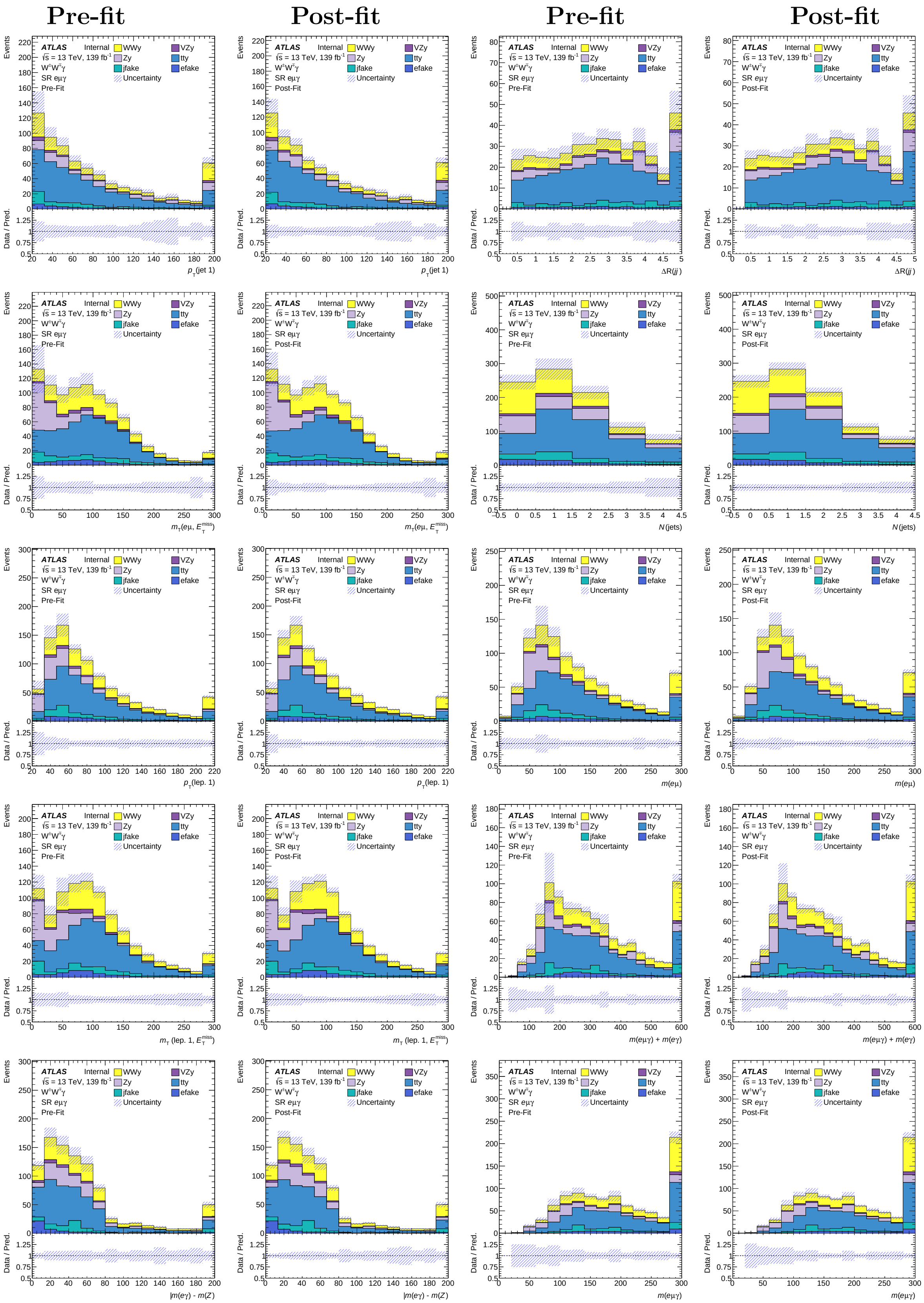

Figure 10.3: Distributions of the various variables for events in the $e^{\pm}\mu^{\mp}\gamma$ signal region (Left) pre-fit (right) post-fit. The uncertainties indicated in the figures include both statistical and systematic uncertainties. The post-fit result is obtained from the binned maximum likelihood fit with Asimov data and is described in Section 11.2.2.

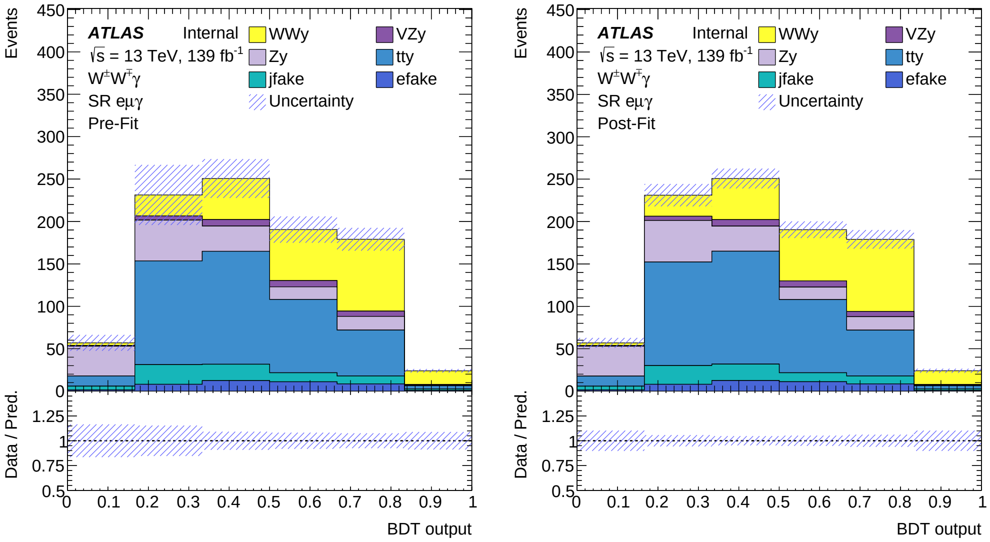

Figure 10.4: Distributions of the BDT score applied to the events in the $e^{\pm}\mu^{\mp}\gamma$ signal region (Left) pre-fit (right) post-fit. The uncertainties indicated in the figures include both statistical and systematic uncertainties. The post-fit result is obtained from the binned maximum likelihood fit with Asimov data and is described in Section 11.2.2.

10.9 BDT validation

Since the signal region is blinded, we validate the variables used to train the BDT in the $e^{\pm}\mu^{\mp}\gamma$ signal region by considering the agreement between data and MC for the BDT distribution in each of the control regions and validation region. Pre-fit and post-fit BDT distributions are given in Figure 10.5 for the Diboson validation region, Figure 10.6 for the $t\bar{t}\gamma$ control region, Figure 10.7 for the $Z\gamma$ control region, Figure 10.8 for the Zjets control region. Reasonable agreement between data and MC is observed. Here, pre-fit and post-fit refer to the results of fitting the control regions to data as described in Section 11.2.1.

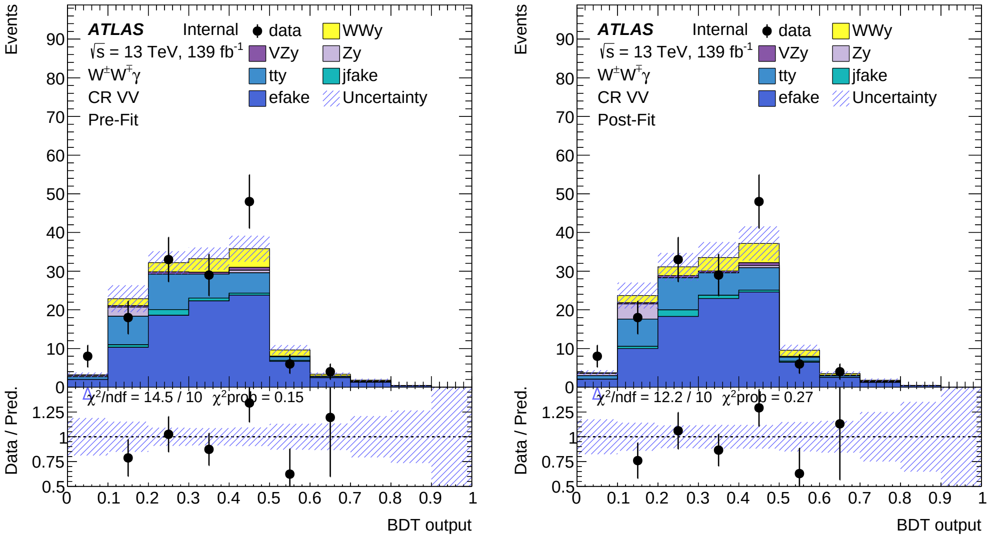

Figure 10.5: Distributions of the BDT score applied to the events in the Diboson validation region (Left) pre-fit (right) post-fit. The uncertainties indicated in the figures include both statistical and systematic uncertainties. The post-fit result is obtained from the binned maximum likelihood fit with the control regions to data and is described in Section 11.2.1.

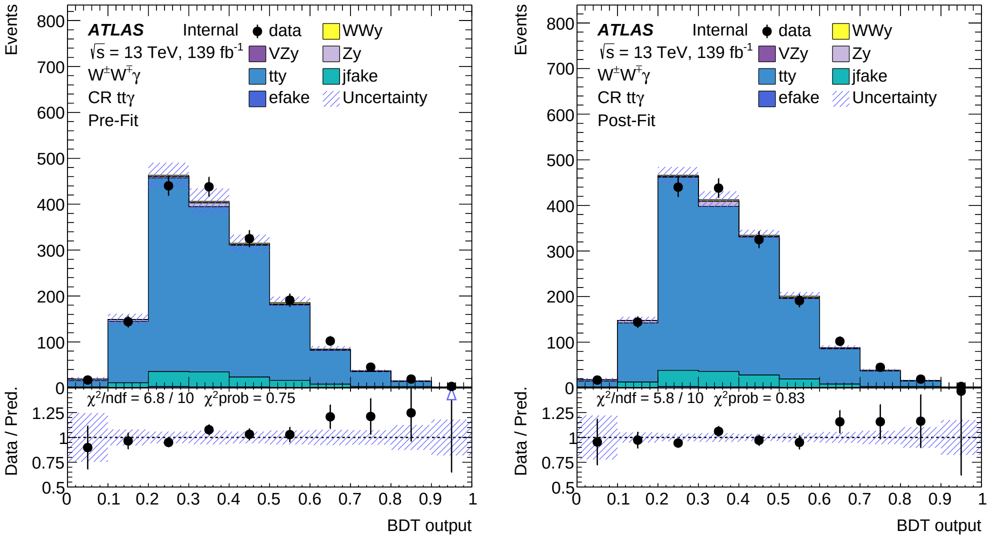

Figure 10.6: Distributions of the BDT score applied to the events in $t\bar{t}\gamma$ control region (Left) pre-fit (right) post-fit. The uncertainties indicated in the figures include both statistical and systematic uncertainties. The post-fit result is obtained from the binned maximum likelihood fit with the control regions to data and is described in Section 11.2.1.

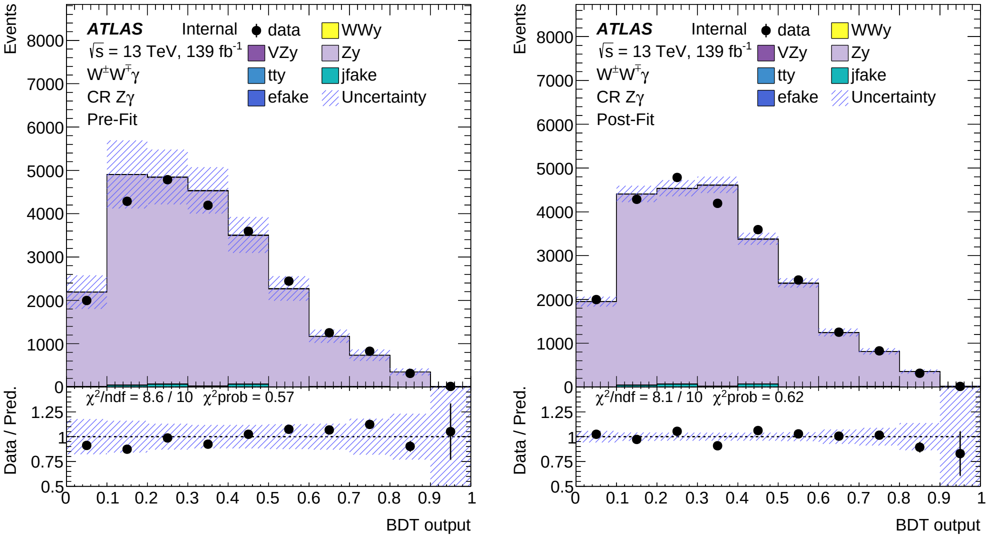

Figure 10.7: Distributions of the BDT score applied to the events in $Z\gamma$ control region (Left) pre-fit (right) post-fit. The uncertainties indicated in the figures include both statistical and systematic uncertainties. The post-fit result is obtained from the binned maximum likelihood fit with the control regions to data and is described in Section 11.2.1.

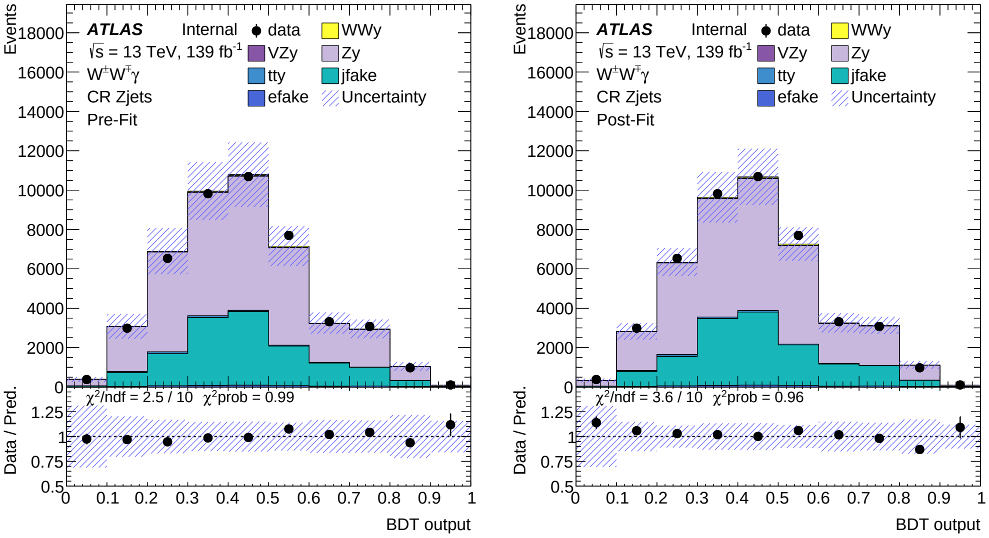

Figure 10.8: Distributions of the BDT score applied to the events in Zjets control region (Left) pre-fit (right) post-fit. The uncertainties indicated in the figures include both statistical and systematic uncertainties. The post-fit result is obtained from the binned maximum likelihood fit with the control regions to data and is described in Section 11.2.1.

Chapter 11

Statistical Analysis and Results

The measurement of the $W^{\pm}W^{\mp}\gamma$ cross section is performed by multiplying the predicted $W^{\pm}W^{\mp}\gamma$ cross section by measuring the signal strength μ, which represents the ratio between the measured $W^{\pm}W^{\mp}\gamma$ cross section and the $W^{\pm}W^{\mp}\gamma$ cross section predicted by theory. The signal strength is determined by performing a binned maximum likelihood fit to the output of the BDT distribution in the $e^{\pm}\mu^{\mp}\gamma$ signal region and the control regions simultaneously. The likelihood function is constructed and the binned maximum likelihood fit is performed using `TRExFitter` [93] software package.

11.1 The likelihood function

11.1.1 Single bin likelihood function

Since the theoretical cross section times the experimentally determined integrated luminosity gives the expected number of events for a particular process, we can measure the cross section by counting the number of signal events in a particular region and comparing this to the number of events predicted by theory. The probability to measure n events when the expected number of events is given by $\nu = \langle n \rangle$ is given by a Poisson distribution:

$$P(n|\nu) = \frac{\nu^n}{n!} e^{-\nu}. \tag{11.1}$$

The expected number of events is given by the sum of the expected number of signal events, $\langle s \rangle$, that we want to measure and the expected number of background events, $\langle b \rangle$, that we are not interested in:

$$\nu = \langle s \rangle + \sum_i \langle b \rangle_i \tag{11.2}$$

where the sum runs over the different background processes considered. The signal process is parameterized by multiplying the expected number of signal events by the signal strength, which is left unconstrained during the fitting procedure:

$$\nu = \mu \langle s \rangle + \sum_i \langle b \rangle_i. \tag{11.3}$$

A signal strength of 1 corresponds to the SM prediction given by the MC simulation. Other values correspond to departures from the SM prediction. Formally, the signal strength can be written as the ratio of the measured cross section (proportional to the number of events) to the predicted cross section:

$$\mu = \frac{\sigma^{\text{measured}}_{W^\pm W^\mp \gamma}}{\sigma^{\text{predicted}}_{W^\pm W^\mp \gamma}} \tag{11.4}$$

To measure the signal strength, a likelihood function is constructed using Equation 11.1 with the parameterized expectation value given in Equation 11.3:

$$L(\mu|n) = \frac{(\mu \langle s \rangle + \sum_i \langle b \rangle_i)^n}{n!} e^{-(\mu \langle s \rangle + \sum_i \langle b \rangle_i)} \tag{11.5}$$

Finding the value of the signal strength that maximizes the likelihood function in Equation 11.5 provides the measured value of μ.

11.1.2 Multi-bin likelihood function

When the expected number of signal events is small or on the order of the expected number of background events, it is necessary to include more information into the likelihood function than is present in the total number of events. Differences in the shape of the distribution of a variable for signal and background processes can be included in the likelihood function by binning the distribution in a histogram, forming the single bin likelihood function given in Equation 11.5 for each bin, and then multiplying the individual likelihood functions together to form a multi-bin likelihood function:

$$L(\mu|\boldsymbol{n}) = \prod_i \frac{(\mu\langle s\rangle_i + \sum_j \langle b\rangle_j)^{n_i}}{n_i!} e^{-(\mu\langle s\rangle_i + \sum_j \langle b\rangle_j)} \tag{11.6}$$

where the sum runs over the histogram bins included. Additional information on the shape and normalization of the background processes in the signal region is included in the likelihood function by including bins for control regions enriched in those processes.

11.1.3 Systematic uncertainties

The expected number of signal and background events per bin is provided by MC simulation that includes several sources of uncertainties as described in Chapter 7. Performing the binned maximum likelihood fit while neglecting these systematic uncertainties leads to a potentially overly optimistic estimate, called the statistical only estimate. Except in the low statistics limit, the sources of systematic uncertainties will influence the results of the measurement and must be taken into account. The systematic uncertainties are included in the likelihood function by parameterizing the expected number of signal and background events as a function of a set of constrained parameters:

$$s(\boldsymbol{\alpha}) = \mu\langle s\rangle \prod_k (1 + \alpha_k \delta_k) \tag{11.7}$$

$$b(\boldsymbol{\alpha}) = \langle b\rangle \prod_k (1 + \alpha_k \delta_k) \tag{11.8}$$

where δ_k is the magnitude of uncertainty k and α_k is a free parameter associated with uncertainty k. As an example, an 20% uncertainty on the expected number of events for the signal would correspond to $\delta = 0.2$. The free parameters associated with each systematic uncertainty is determined simultaneously with the signal strength. Since the free parameter for each systematic uncertainty must be measured during the likelihood fit procedure but are not of interest to the actual measurement, they are referred to as nuisance parameters. For each nuisance parameter, a Gaussian constraint multiplies the likelihood function:

$$N(\alpha) = \frac{1}{\sqrt{2\pi}} e^{\alpha^2} \tag{11.9}$$

The likelihood function now has the form:

$$L(\mu|\boldsymbol{n}, \boldsymbol{\alpha}) = \prod_i \frac{(\mu\langle s(\alpha)\rangle_i + \sum_j \langle b(\alpha)\rangle_j)^{n_i}}{n_i!} e^{-(\mu\langle s(\alpha)\rangle_i + \sum_j \langle b(\alpha)\rangle_j)} \prod_k N(\alpha_k) \tag{11.10}$$

where $s(\alpha)$ and $b(\alpha)$ are given by Equation 11.7.

11.1.4 Treatment of systematic uncertainties

There are different types of uncertainties: uncertainties that affect the shape of the distribution of an observable or variable, uncertainties that affect the number of events expected in a region of interest, referred to as acceptance uncertainties, uncertainties that affect the total number of predicted events, referred to as normalization uncertainties, and uncertainties that are a combinations of shape, acceptance, and normalization uncertainties.

Some uncertainties can affect one specific sample, for example, theoretical uncertainties associated with a particular MC sample. Others can affect all MC samples, for example, detector systematic uncertainties.

Symmetrization

Each uncertainty is used to construct an up and down variation of the nominal prediction. A Gaussian constraint is associated with each uncertainty where the width is determined by the size of the uncertainty. The mean of the Gaussian distribution is set to be the nominal estimate so that there are no pulls unless data provides evidence for a different value. Since the nominal estimate is not guaranteed to be exactly at the center of the up and down variations, the uncertainties are symmetrized. There are two types of symmetrization used in the analysis presented in this thesis: two-sided symmetrization and one-sided symmetrization. One-sided symmetrization is used when there is only a single variation provided (as opposed to separate up and down variations). In this case, the variation is taken as the up variation and the down variation is formed by reflecting the up variation across the nominal estimate. Two-sided symmetrization is used when separate up and down variations are provided. In this case, the up variation is constructed by taking the average deviation of the two uncertainties. The down variation is constructed by reflecting the up variation across the nominal variation.

Pruning

There are over a hundred systematic uncertainties considered in the statistical analysis of ATLAS data presented in this thesis. Each systematic uncertainty is associated with an independent nuisance parameter in the likelihood fit used to perform the measurement of the $W^{\pm}W^{\mp}\gamma$ signal strength that needs to be determined during the fitting procedure. To simplify the likelihood fit, nuisance parameters associated with systematic uncertainties are removed if there impact on the yield of shape is less than 0.5%. Similarly, nuisance parameters associated with statistical uncertainties per bin that are less that 0.5% are removed. A study was performed to insure that removing these nuisance parameters has a negligible effect on the measurement of the $W^{\pm}W^{\mp}\gamma$ signal strength.

11.1.5 Background normalization nusiance parameters

An unconstrained parameter in the likelihood fit, like the signal strength, corresponds to a constrained nuisance parameter with infinite uncertainty. This allows the measured number of events for the corresponding process to be determine entirely by data. When the number of events in data is large and the measurement is performed in a region dominated by the process associated with the unconstrained nuisance parameter, the uncertainty on the number of events is bounded by the uncertainty on the number of events in data, $\sqrt{N}$. While these conditions do not hold for the $W^{\pm}W^{\mp}\gamma$ process in the $e^{\pm}\mu^{\mp}\gamma$ signal region, it is true for several backgrounds to the $W^{\pm}W^{\mp}\gamma$ process. To take advantage of this, nuisance parameters denoted by β multiply the expected number of background events in Equation 11.7 for major backgrounds in the same way that the signal strength multiplies the expected number of signal events and the binned BDT output distributions in the associated control regions are included in the likelihood fit. For backgrounds that do not have an associated control region $\beta == 1$. The β nuisance parameters along with the α nuisance parameters introduced earlier are combined into vectors and are collectively denoted by $\boldsymbol{\theta} = (\boldsymbol{\alpha}, \boldsymbol{\beta})$. The likelihood function now has the form:

$$L(\mu|\boldsymbol{n}, \boldsymbol{\theta}) = \prod_{i} \frac{(\mu\langle s(\alpha)\rangle_i + \sum_j \beta_i \langle b(\alpha)\rangle_j)^{n_i}}{n_!!} e^{-(\mu\langle s(\alpha)\rangle_i + \sum_j \beta_i \langle b(\alpha)\rangle_j)} \prod_{k} N(\alpha_k) \tag{11.11}$$

where β_i is an unconstrained parameter for the $t\bar{t}\gamma$, $Z\gamma$, and $e \rightarrow \gamma$ fake backgrounds and 1 for all others.

11.1.6 MC uncertainty nuisance parameters

The expected number of events for a process is given by the sum of the event weights

$$\langle n \rangle = \sum_i w_i \tag{11.12}$$

where the index i runs over all events considered and w_i corresponds to the weight associated with each event. Since the number of expected events follows a Poisson distribution, the uncertainty is given by the sum-of-squares of the event weights:

$$\delta(\langle n \rangle) = \sqrt{\sum_i w_i^2} \tag{11.13}$$

Similarly, the total number of events in a region or bin of a histogram is given by the sum of the expected number of events for each process and the uncertainty is given by the sum-of-squares of the event weights for all events from all processes. Since the number of MC events produced is finite, the uncertainty on the expected number of events is not zero and must be accounted for.

The MC statistical uncertainty is accounted for in the likelihood function by multiplying the expected total number of events per bin by a nuisance parameter denoted by γ constrained by a Gamma constraint $\Gamma(\gamma)$. The vector of nuisance parameters is now given by $\boldsymbol{\theta} = (\boldsymbol{\alpha}, \boldsymbol{\beta}, \boldsymbol{\gamma})$. The final form of the likelihood function is given by:

$$L(\mu|\boldsymbol{n}, \boldsymbol{\theta}) = \prod_i \frac{(\gamma_i \nu_i)^{n_i}}{n_!!} e^{-(\gamma_i \nu_i)} \Gamma(\gamma_i) \prod_k N(\alpha_k) \tag{11.14}$$

where

$$\nu_i(\mu, \boldsymbol{\alpha}, \boldsymbol{\beta}) = \mu \langle s_i \rangle \prod_k (1 + \alpha_k \delta_{ik}) + \sum_j \beta_j \langle b_{ij} \rangle \prod_l (1 + \alpha_{jl} \delta_{ijl}) \tag{11.15}$$

11.2 Expected results

Currently, the analysis is blinded meaning that the analysis is waiting for approval to use data in the $e^{\pm}\mu^{\mp}\gamma$ signal region to extract the measured $W^{\pm}W^{\mp}\gamma$ signal strength and associated cross section; therefore, the results presented here will include only the expected results. The expected results are obtained in two steps: first, a binned maximum likelihood fit is performed using data in the control regions to obtain the best-fit values for all nuisance parameters. Using the best fit values of all of the nuisance parameters, an Asimov data set is constructed using the expected signal and background distributions after all of the nuisance parameters have been fit to their best fit values. The maximum likelihood fit is then repeated using the Asimov data set instead of data and including the $e^{\pm}\mu^{\mp}\gamma$ signal region. The best fit values for the signal strength and nuisance parameters obtained by performing the binned maximum likelihood fit using the Asimov data set will be one by construction. The measured statistical significance and uncertainty on the measured signal strength represent the expected values for these quantities. When approval to unblind is given, the binned maximum likelihood fit will be performed using data in all regions and the expected results will be updated with the measured results.

The expected $W^{\pm}W^{\mp}\gamma$ signal strength is measured by maximizing the likelihood function given in Equation 11.14 that is constructed using the binned BDT output distribution in the $e^{\pm}\mu^{\mp}\gamma$ signal region and the $t\bar{t}\gamma$, $Z\gamma$, and VV control regions with respect to the Asimov data. The regions, distribution, and number of bins used is summarized in Table 11.1. The processes considered in each control region is summarized in Table 11.2.

Table 11.1: Overview of the regions included in the fit.

Region	Distribution	Number of Bins	Type
$e^{\pm}\mu^{\mp}\gamma$ SR	BDT	6	Signal
$t\bar{t}\gamma$ CR	BDT	6	Control
$Z\gamma$ CR	BDT	6	Control
VV CR	BDT	6	Control

Classification	Type	Name
Signal	MC	$W^{\pm}W^{\mp}\gamma$
Background	MC	$VZ\gamma$ jet → γ
	Free floating MC	$t\bar{t}\gamma$ $Z\gamma$ $e \rightarrow \gamma$

Table 11.2: Summary of processes included in the likelihood fit.

11.2.1 Control region fit to data

This section describes the results of the binned maximum likelihood fit performed using data in the control regions. The measured nuisance parameters, including the $t\bar{t}\gamma$, $Z\gamma$, and $e \rightarrow \gamma$ normalization factors will later be used to construct the Asimov data set used when performing the binned maximum likelihood fit with the signal region used to extract the expected statistical significance and the expected uncertainty on the signal strength. Performing the fit in the $t\bar{t}\gamma$ $Z\gamma$, and VV CRs with data also helps to validate the fit procedure.

The expected number of events and uncertainty on the total number of events as well as for each process before the likelihood fit has been performed are referred to as pre-fit yields and pre-fit uncertainties. The expected number of events and associated uncertainties after the nuisance parameters have been set to their best fit values are referred to as post-fit yields and post-fit uncertainties. The pre-fit and post-fit BDT output distributions in the $t\bar{t}\gamma$, $Z\gamma$, and VV CRs are compared in Figure 11.1 for the $t\bar{t}\gamma$ CR, Figure 11.2 for the $Z\gamma$ CR, and Figure 11.3 for the VV CR. Similarly, the pre-fit and post-fit yields in the $t\bar{t}\gamma$, $Z\gamma$, and VV CRs are given in Table 11.3 through Table 11.5. The pre-fit and post-fit distributions and yields are similar, indicating that the background estimations agree well with data. One difference between the pre-fit and post-fit results is the magnitude of the uncertainty on the number of events, specifically $Z\gamma$ and $t\bar{t}\gamma$. This result is due to the fact that the control regions for $t\bar{t}\gamma$ and $Z\gamma$ have large number of events and the regions are mostly pure in the process of interest, resulting in an uncertainty determined primarily by the uncertainty on the number of events, $\sqrt{N}$.

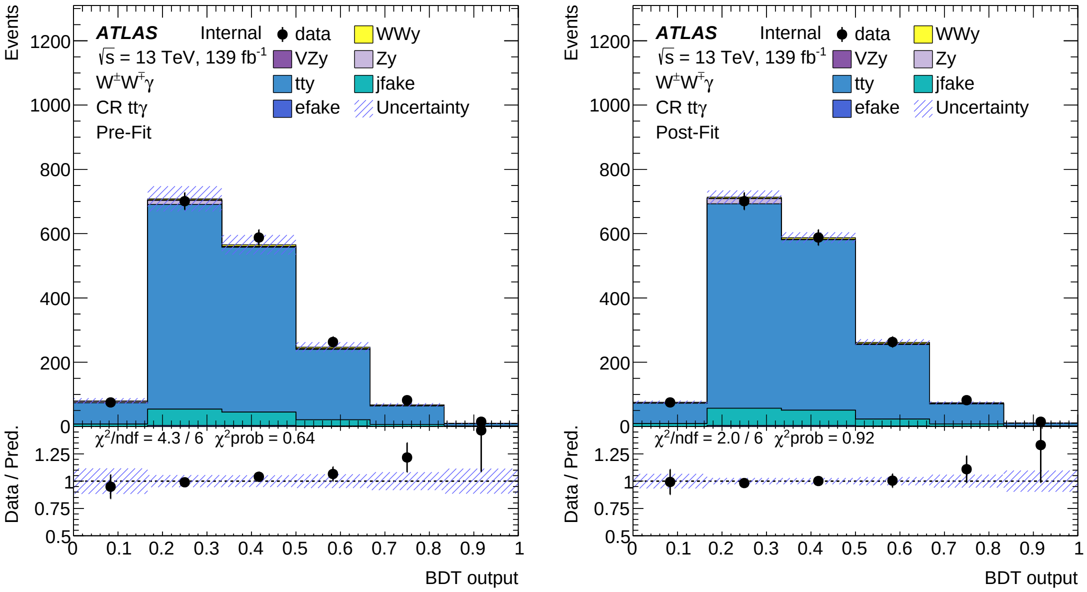

Figure 11.1: Pre-fit (left) and post-fit (right) distributions for the $t\bar{t}\gamma$ CR. Uncertainty is from both statistical and systematic uncertainties.

	Pre-fit	Post-fit
$W^{\pm}W^{\mp}\gamma$	17.52 ± 2.17	17.07 ± 2.01
$VZ\gamma$	3.53 ± 0.78	3.46 ± 0.73
$Z\gamma$	20.54 ± 11.15	21.21 ± 5.75
$t\bar{t}\gamma$	1500.28 ± 57.15	1532.27 ± 69.20
jet $\rightarrow \gamma$	125.78 ± 53.92	139.95 ± 56.37
$e \rightarrow \gamma$	9.53 ± 1.13	9.53 ± 1.46
Total	1677.18 ± 82.09	1723.49 ± 42.21
data	1724	1724

Table 11.3: Pre and post-fit event yields in the $t\bar{t}\gamma$ CR. Uncertainties include statistical and systematic uncertainties.

The nuisance parameters are either: α nuisance parameters associated with systematic uncertainties, β nuisance parameters associated with the background normalization, or γ nuisance parameters associated with the MC statistical uncertainty for each bin.

	Pre-fit	Post-fit
$W^{\pm}W^{\mp}\gamma$	41.26 ± 2.02	40.98 ± 2.00
$VZ\gamma$	31.57 ± 6.49	31.46 ± 6.40
$Z\gamma$	24208.40 ± 2783.95	23392.00 ± 172.78
$t\bar{t}\gamma$	37.28 ± 5.16	35.39 ± 3.95
jet $\to \gamma$	198.89 ± 92.75	188.58 ± 67.63
$e \to \gamma$	19.50 ± 6.54	19.36 ± 5.10
Total	24536.90 ± 2786.90	23707.80 ± 157.84
data	23707	23707

Table 11.4: Pre and post-fit event yields in the $Z\gamma$ CR. Uncertainties include statistical and systematic uncertainties.

	Pre-fit	Post-fit
$W^{\pm}W^{\mp}\gamma$	15.10 ± 0.75	15.05 ± 0.75
$VZ\gamma$	2.44 ± 0.52	2.44 ± 0.50
$Z\gamma$	3.48 ± 2.41	5.28 ± 1.98
$t\bar{t}\gamma$	30.02 ± 3.30	29.49 ± 2.69
jet $\to \gamma$	3.86 ± 1.52	4.15 ± 1.33
$e \to \gamma$	87.66 ± 6.41	88.65 ± 12.42
Total	142.56 ± 8.41	145.06 ± 11.96
data	146	146

Table 11.5: Pre and post-fit event yields in the VV CR. Uncertainties include statistical and systematic uncertainties.

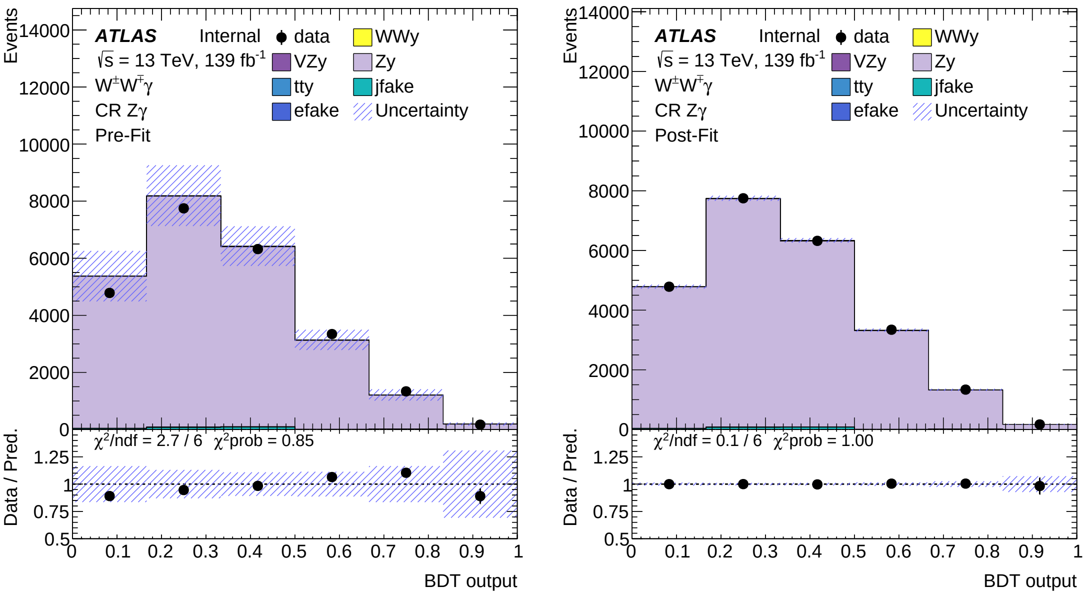

Figure 11.2: Pre-fit (left) and post-fit (right) distributions for the $Z\gamma$ CR. Uncertainty is from both statistical and systematic uncertainties.

The measured value of the unconstrained parameters: $t\bar{t}\gamma$, $Z\gamma$, and $e \to \gamma$ background normalization factors are presented in Figure 11.4. The MINOS function is used to calculate the uncertainties on the unconstrained normalization factors. The measured values are all effectively one indicating that the normalization for the pre-fit background estimate agrees well with in these data regions.

The measured nuisance parameters associated with the systematic uncertainties are presented in Figure 11.5 through Figure 11.14.

Since all of the nuisance parameters associated with the systematic uncertainties are all constrained by a unit Gaussian they are centered on zero. Nuisance parameters with a post-fit value other than one are said to be pulled. The dotted line in the figure represents a pull of one. A pull can be considered significant if the pull is greater than 1 standard deviation, given by the vertical line in the Figure 11.5, from 0. Significant pulls can indicated mis-modeling in the estimation of a process but this is not always the case. Here, we see that there are no significant pulls.

Finally, the measured nuisance parameters associated with the MC statistical uncertainty

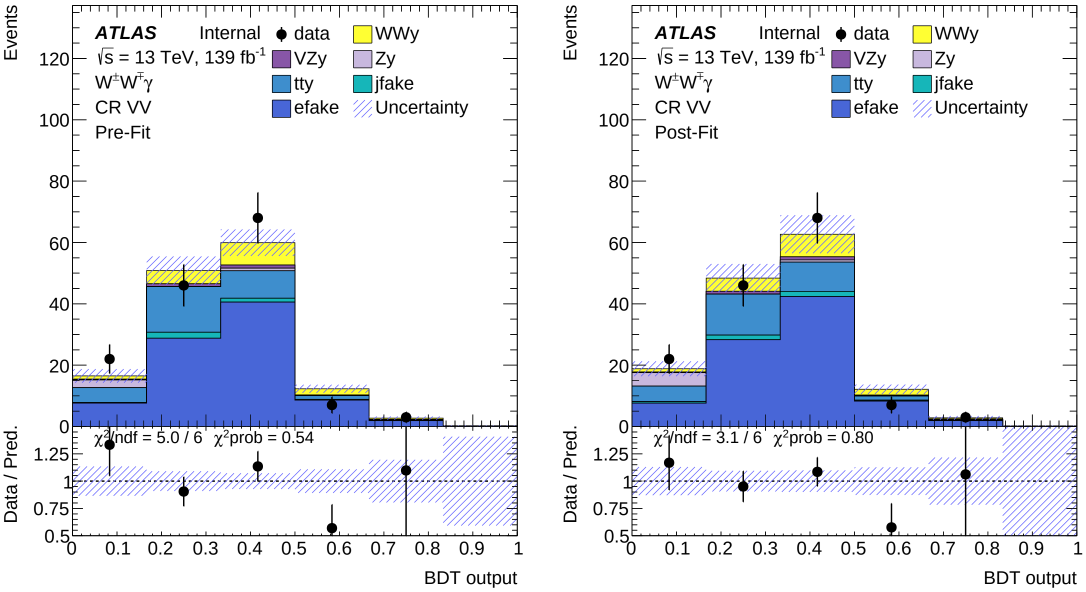

Figure 11.3: Pre-fit (left) and post-fit (right) distributions for the VV CR. Uncertainty is from both statistical and systematic uncertainties.

in each bin are given in Figure 11.15. Here we see there are bins with a large uncertainty on the expected number of events in that bin. This large uncertainty is due to finite number of MC events produced for the $Z\gamma$ and Zjets processes and the fact that there exist events with larger than average event weight that inflate the MC statistical uncertainty.

11.2.2 Asimov fit

The Asimov fit is performed by fitting the signal and control regions to an Asimov data set using the expected number of signal and background events per bin after all of the nuisance parameters have been set to the best fit values obtained by performing the binned maximum likelihood fit using data in the control regions presented in Section 11.2.1. The pre-fit and post-fit distributions of the $e^{\pm}\mu^{\mp}\gamma$ SR are given in Figure 11.16. The pre-fit and post-fit yields in the $e^{\pm}\mu^{\mp}\gamma$ SR are given in Table 11.6. The measured signal strength and the other unconstrained background normalization factors are given in Figure 11.4. The uncertainty on the expected signal strength is found to be 15%.

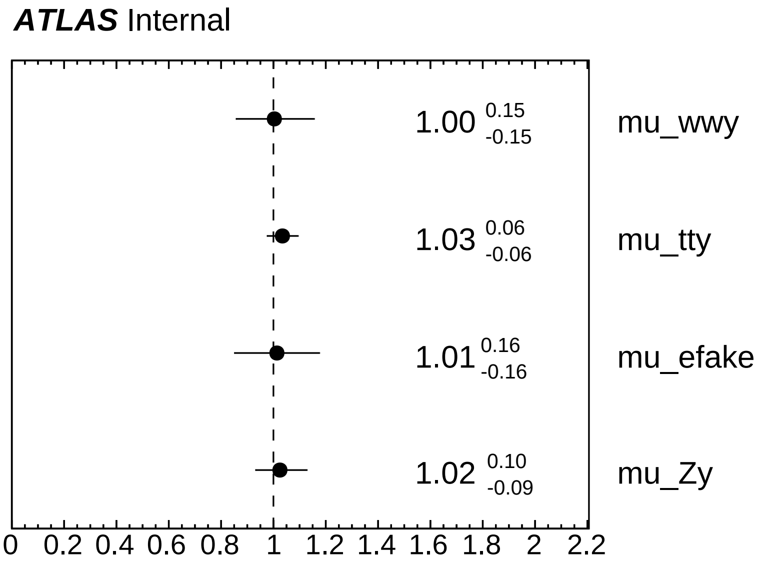

Figure 11.4: Normalization factors for the $t\bar{t}\gamma$ and $Z\gamma$ processes as determined by the fitting procedure described in the note.

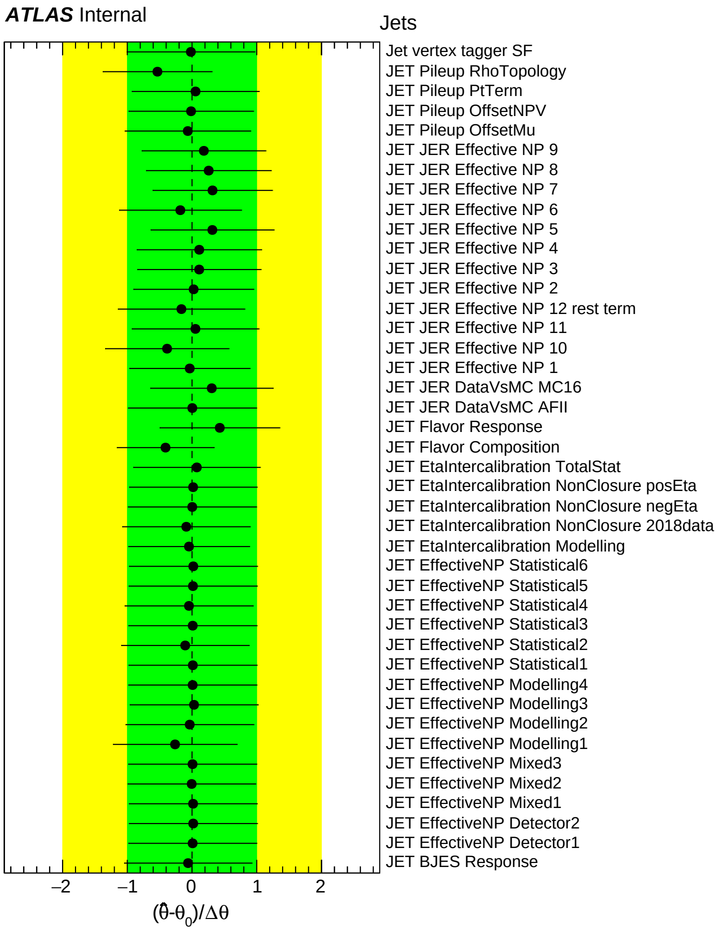

Figure 11.5: Post-fit values obtained for the nuisance parameters associated with the jet systematic uncertainties considered in the likelihood fit.

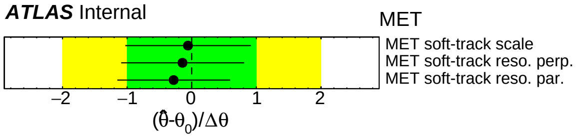

Figure 11.6: Post-fit values obtained for the nuisance parameters associated with the $E_{\mathrm{T}}^{\mathrm{miss}}$ systematic uncertainties considered in the likelihood fit.

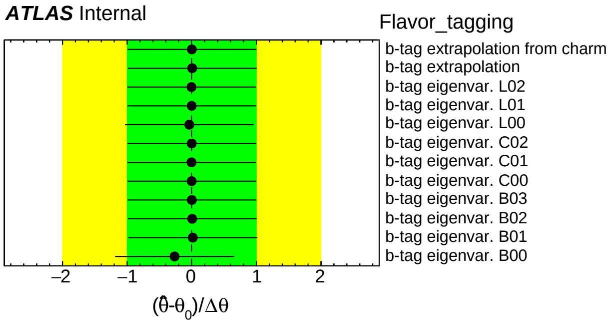

Figure 11.7: Post-fit values obtained for the nuisance parameters associated with the flavor tagging systematic uncertainties considered in the likelihood fit.

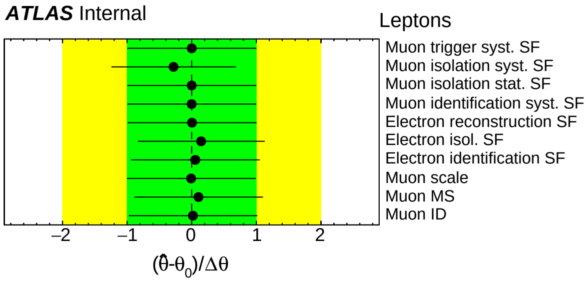

Figure 11.8: Post-fit values obtained for the nuisance parameters associated with the lepton systematic uncertainties considered in the likelihood fit.

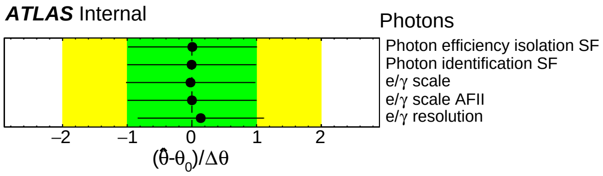

Figure 11.9: Post-fit values obtained for the nuisance parameters associated with the photon systematic uncertainties considered in the likelihood fit.

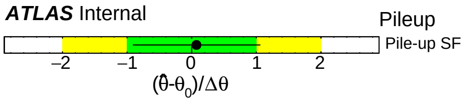

Figure 11.10: Post-fit values obtained for the nuisance parameters associated with the systematic uncertainties considered in the likelihood fit.

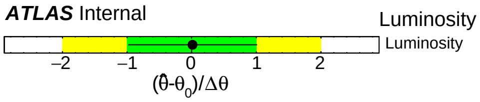

Figure 11.11: Post-fit values obtained for the nuisance parameters associated with the luminosity systematic uncertainty considered in the likelihood fit.

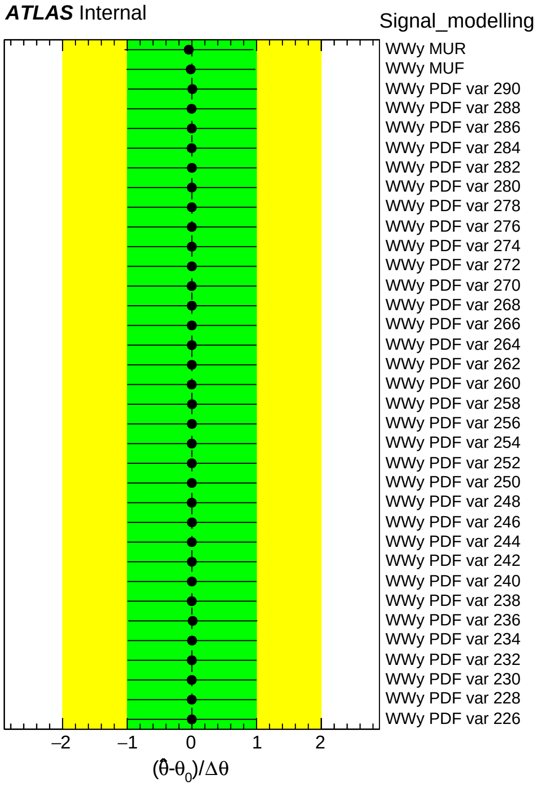

Figure 11.12: Post-fit values obtained for the nuisance parameters associated with the signal modeling systematic uncertainties considered in the likelihood fit.

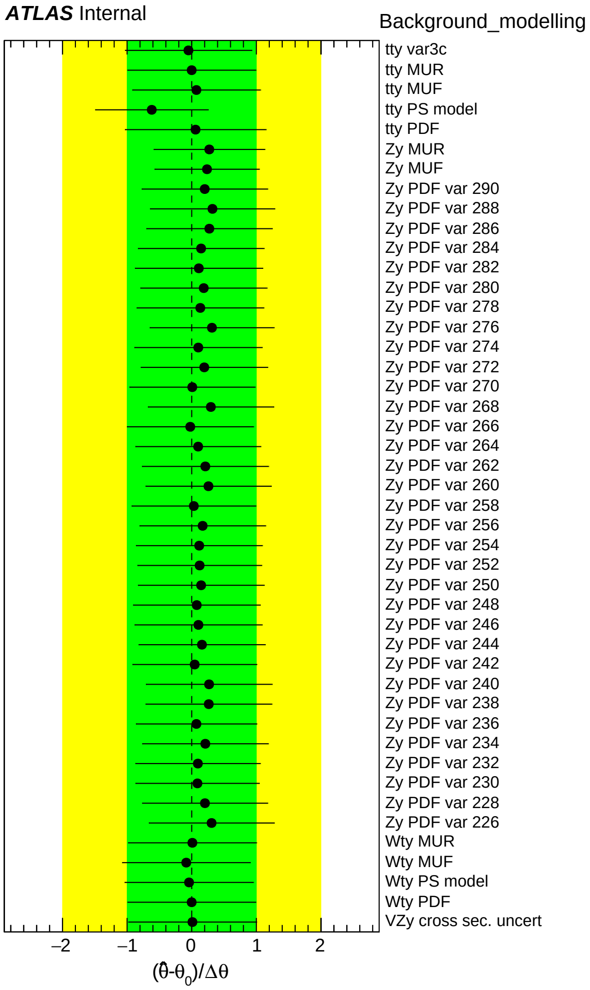

Figure 11.13: Post-fit values obtained for the nuisance parameters associated with the background systematic uncertainties considered in the likelihood fit.

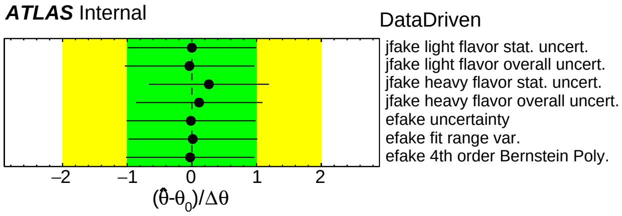

Figure 11.14: Post-fit values obtained for the nuisance parameters associated with the data driven systematic uncertainties considered in the likelihood fit.

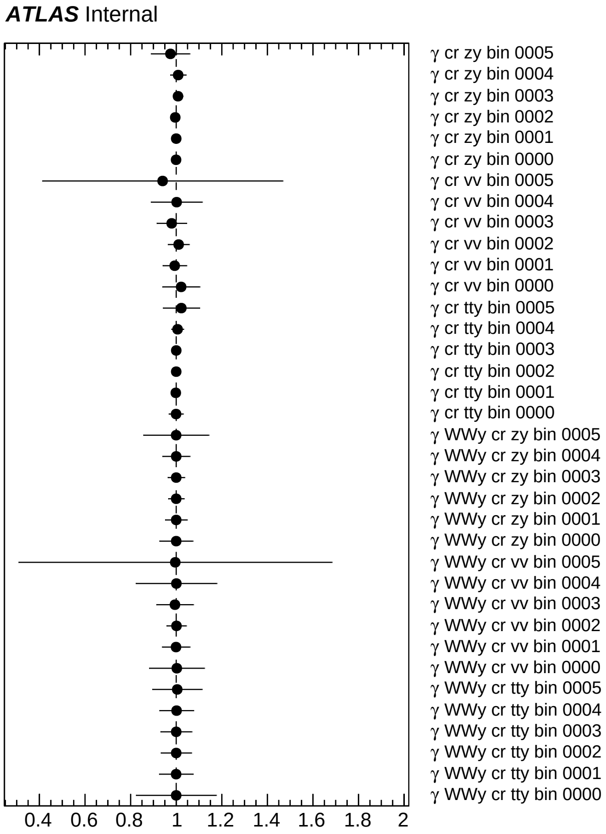

Figure 11.15: Post-fit values of the γ parameters that represent the uncertainty per bin due to finite Monte Carlo statistics.

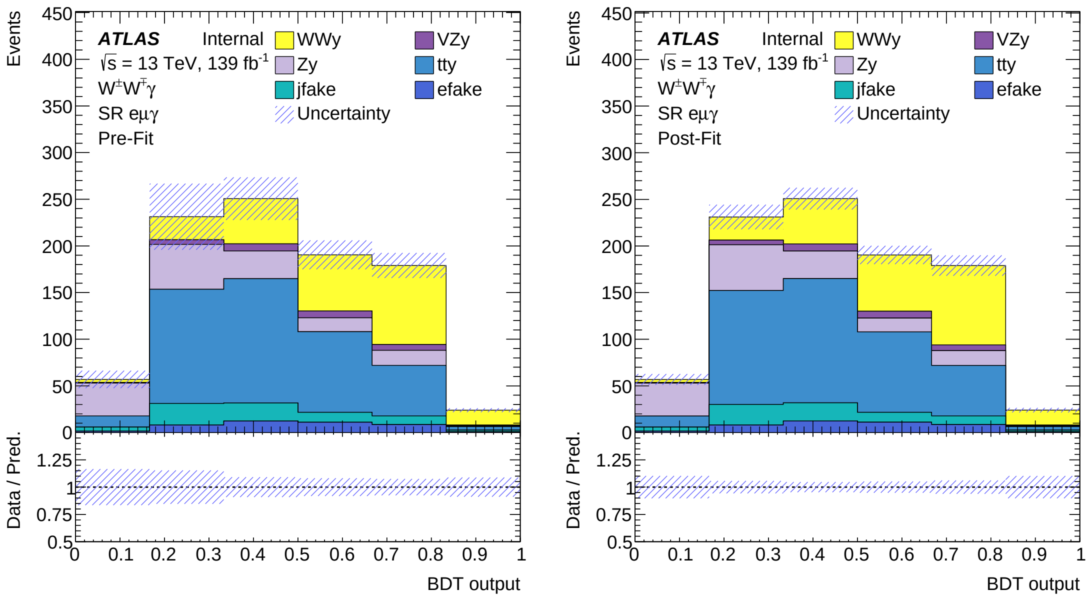

Figure 11.16: Pre-fit (left) and post-fit (right) distributions for the $e^{\pm}\mu^{\mp}\gamma$ SR. Uncertainty is from both statistical and systematic uncertainties.

	Pre-fit	Post-fit
$W^{\pm}W^{\mp}\gamma$	237.14 ± 11.19	237.97 ± 34.69
$VZ\gamma$	27.84 ± 5.68	27.85 ± 5.64
$Z\gamma$	144.76 ± 25.71	145.13 ± 13.32
$t\bar{t}\gamma$	411.82 ± 36.32	411.39 ± 29.00
jet $\rightarrow \gamma$	68.59 ± 34.11	67.55 ± 23.77
$e \rightarrow \gamma$	42.12 ± 3.14	42.27 ± 6.46
Total	932.27 ± 62.98	932.15 ± 29.07

Table 11.6: Pre and post-fit event yields in the $e^{\pm}\mu^{\mp}\gamma$ SR. Uncertainties include statistical and systematic uncertainties.

To understand what individual systematic uncertainties have the largest impact on the measurement, for each nuisance parameter, the fit is repeated four additional times after fixing the value of the nuisance parameter to $\pm 1\sigma$ of pre-fit and post-fit uncertainty with respect to the nominal value of 0. The impact is then calculated as:

$$\Delta\mu = \mu^{*} - \mu_0 \tag{11.16}$$

where μ_0 is the value of μ obtained from the nominal fit and μ^* is the value of μ obtained for each the four additional fits mentioned above. If the impact of a nuisance parameter is large, this indicates that the measurement is sensitive to that nuisance parameter and that nuisance parameter contributes significantly to the uncertainty on the measured signal strength. Conversely, a nuisance parameter that has a negligible impact on the signal strength, has a negligible impact on the measurement. The impact of each nuisance parameter is presented in Figure 11.17.

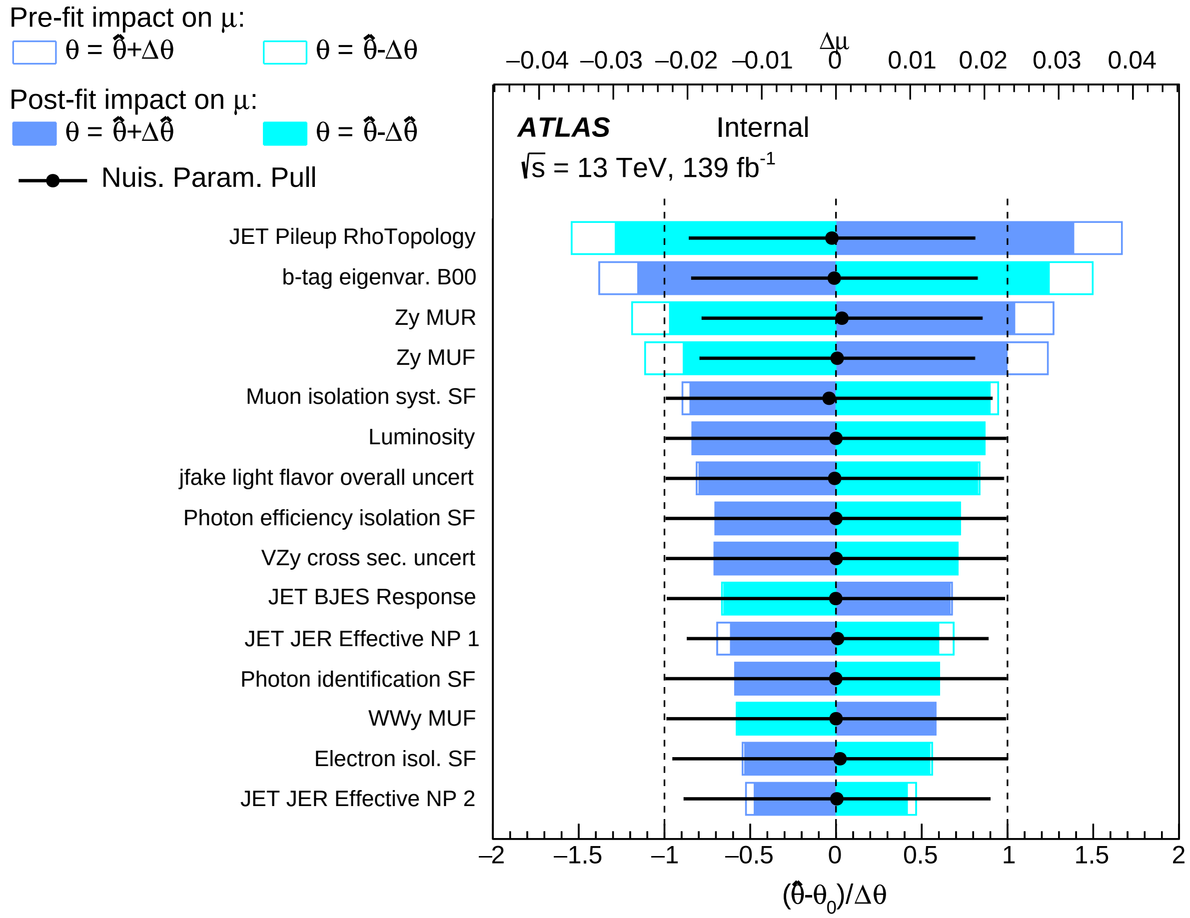

Figure 11.17: Expected NP rankings for the $W^{\pm}W^{\mp}\gamma$ normalization factor obtained in the Asimov fit.

To better understand the origin of the uncertainty on the measured signal strength, the uncertainty on the measured signal strength due to different categories or groups of nuisance parameters is calculated as the impact given in Equation 11.16 divided by the signal strength from the nominal maximum likelihood fit:

$$\frac{\Delta\mu}{\mu_0} = \frac{\mu^* - \mu_0}{\mu_0}. \tag{11.17}$$

In this analysis the systematic uncertainties are grouped according to the sections in Chapter 5. The uncertainty due to each category is calculated by performing a fit where the nuisance parameters for the category are fixed to their best-fit values, and then subtracting the resulting uncertainty in the measured signal strength in quadrature from the uncertainty from the nominal fit. In addition to the impact due to groups of uncertainties, the systematic uncertainty due to all systematics as well as the statistical uncertainty are given in Table 11.7. We see that the largest sources of systematic uncertainty to the analysis is related to jets. This makes sense in light of the fact that the primary difference between the largest background to the $W^{\pm}W^{\mp}\gamma$ process, $t\bar{t}\gamma$, is due to the presence of b-tagged jets.

SubCategory	Uncertainty ($\Delta\mu/\mu[\%]$)
Jets	5.0
MC statistics	3.9
Background modeling	3.6
Flavor tagging	3.1
Data-driven	2.7
Leptons	2.4
Photons	2.3
Luminosity	1.8
Signal modeling	1.6
Pile-up	1.0
MET	1.0
Total systematic uncertainty	10.3
Data statistics	10.9
Normalization factors	4.3
Total statistical uncertainty	11.9

Table 11.7: The impact for each group of systematic uncertainties. The groups are grouped according to the sections in Chapter 5

After the maximum likelihood fit has been performed, we can form the test statistic

$$\lambda(\boldsymbol{\theta}) = \ln \frac{L(\mu, \hat{\hat{\boldsymbol{\theta}}})}{L(\hat{\mu}, \hat{\boldsymbol{\theta}})} \tag{11.18}$$

where $L(\hat{\mu}, \hat{\boldsymbol{\theta}})$ represents the maximum likelihood result when μ and all nuisance parameters are fit simultaneous (i.e. the nominal fit result) and $L(\mu, \hat{\hat{\boldsymbol{\theta}}})$ represents the maximum likelihood results obtained when μ is set to a particular value. Hence, the test statistic λ is a function of the signal strength and the value of the nuisance parameters must be obtained for each value of μ. The test statistic λ follows a χ^2 distribution with one degree of freedom in the asymptotic regime. This allows us to compare the different values of μ. The significance of a particular value of μ measured in standard deviations from the measured result is given by the formula

$$Z = \sqrt{-2 \ln \lambda(\mu, \boldsymbol{\theta})}. \tag{11.19}$$

Of particular interest is the comparison between the nominal fit result and the background only case ($\mu == 0$). Comparing these two points yields the significance of the measurement. A scan of the likelihood function about the minimum achieved during the fitting procedure is given in Figure 11.18. The statistical significance can be obtained using Equation 11.19 for the value of $-\ln \lambda(\mu, \boldsymbol{\theta})$ when $\mu == 0$. The expected statistical significance calculated with and without systematic uncertainties and is presented in Table 11.8. The expected statistical significance is above the 5σ discovery threshold in high energy physics experiments for a process. This analysis expects to provide the first observation of the $W^{\pm}W^{\mp}\gamma$ process. the expected fiducial cross section is $10.5^{+17.0\%}_{11.2\%}$ (theory) ± 15% fb (experiment). Where the theory uncertainty is associated with the determination of the fiducial volume and the experimental uncertainty is associated with the determination of the signal strength.

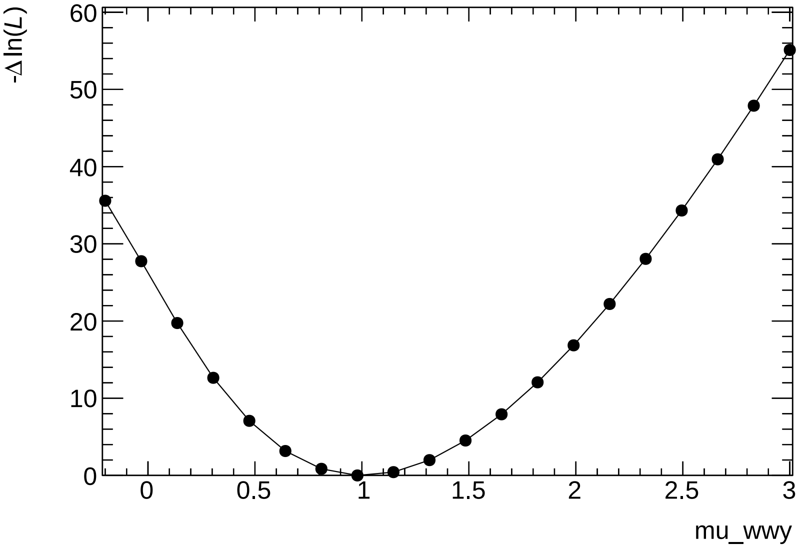

Figure 11.18: Scan of the likelihood function about the minimum achieved during the Asimov fit.

Systematics	Stat. Only
7.21	9.82

Table 11.8: The expected significance with and without systematic uncertainties for the Asimov fit.

Chapter 12

Conclusion

In this thesis, a search for the Standard Model (MS) $W^{\pm}W^{\mp}\gamma$ triboson process in the $e^{\pm}\mu^{\mp}\gamma$ channel was presented. The analysis used $139\,\text{fb}^{-1}$ of proton-proton collision data collided at center of mass energy ($\sqrt{s}$) of 13 TeV collected by the ATLAS detector. The $W^{\pm}W^{\mp}\gamma$ process was studied using events with two opposite-sign, opposite-flavor leptons (e or μ) in association with exactly one photon with transverse momentum greater than 20 GeV. Various backgrounds were estimated using either data-driven methods or simulated MC samples. A BDT was trained using the `XGBoost` package and applied to events in the $e^{\pm}\mu^{\mp}\gamma$ Signal Region to increase the search sensitivity. The BDT distribution was used for the binned maximum likelihood fit to calculate the expected signal strength and its fiducial cross-section. The expected statistical significance of the measurement is 7.2 σ, providing the first observation of the $W^{\pm}W^{\mp}\gamma$ process at the LHC. The expected fiducial cross section is $10.5^{+17.0\%}_{-11.2\%}$ (theory) ± 15% fb (experiment). Where the theory uncertainty is associated with the determination of the fiducial volume and the experimental uncertainty is associated with the determination of the signal strength.

Upon unblinding, significant deviations from the measured $W^{\pm}W^{\mp}\gamma$ cross section and the Standard Model prediction provide can provide evidence for beyond the Standard Model (BSM) physics. In addition, any deviation from the SM prediction can be parameterized in the framework of an effective field theory (EFT) and limits can be placed on these EFT parameters. The results of the EFT measurement are beyond the scope of this thesis and will be presented in another thesis.

References

[1] P.A. Zyla et al. "Review of Particle Physics, 2020-2021. RPP". In: *PTEP* 2020.8 (2020), p. 083C01. DOI: `10.1093/ptep/ptaa104`. URL: `https://cds.cern.ch/record/2729066`.

[2] S. L. Glashow. "Partial Symmetries of Weak Interactions". In: *Nucl. Phys.* 22 (1961), pp. 579–588. DOI: `10.1016/0029-5582(61)90469-2`.

[3] Steven Weinberg. "A Model of Leptons". In: *Phys. Rev. Lett.* 19 (1967), pp. 1264–1266. DOI: `10.1103/PhysRevLett.19.1264`.

[4] Abdus Salam. "Weak and Electromagnetic Interactions". In: *Conf. Proc. C* 680519 (1968), pp. 367–377. DOI: `10.1142/9789812795915_0034`.

[5] Michael E. Peskin and Daniel V. Schroeder. *An Introduction to quantum field theory.* Reading, USA: Addison-Wesley, 1995. ISBN: 978-0-201-50397-5.

[6] Michele Maggiore. *A Modern introduction to quantum field theory.* 2005.

[7] A. Zee. *Quantum field theory in a nutshell.* 2003. ISBN: 978-0-691-14034-6.

[8] A. Zee. *Group Theory in a Nutshell for Physicists.* USA: Princeton University Press, 2016. ISBN: 978-0-691-16269-0, 978-0-691-16269-0, 978-1-4008-8118-5.

[9] Peter W. Higgs. "Broken Symmetries and the Masses of Gauge Bosons". In: *Phys. Rev. Lett.* 13 (1964). Ed. by J. C. Taylor, pp. 508–509. DOI: `10.1103/PhysRevLett.13.508`.

[10] G. S. Guralnik, C. R. Hagen, and T. W. B. Kibble. “Global Conservation Laws and Massless Particles”. In: *Phys. Rev. Lett.* 13 (1964). Ed. by J. C. Taylor, pp. 585–587. DOI: `10.1103/PhysRevLett.13.585`.

[11] F Englert and R Brout. “Broken symmetry and the masses of gauge vector mesons”. In: *Phys. Rev. Lett.* 13 (1964), pp. 321–323. DOI: `10.1103/PhysRevLett.13.321`. URL: `http://cds.cern.ch/record/641592`.

[12] Jeffrey Goldstone, Abdus Salam, and Steven Weinberg. “Broken Symmetries”. In: *Phys. Rev.* 127 (1962), pp. 965–970. DOI: `10.1103/PhysRev.127.965`.

[13] ATLAS Collaboration. “The ATLAS Experiment at the CERN Large Hadron Collider”. In: *JINST* 3 (2008), S08003. 437 p. DOI: `10.1088/1748-0221/3/08/S08003`. URL: `https://cds.cern.ch/record/1129811`.

[14] M Benedikt et al. *LHC Design Report.* CERN Yellow Reports: Monographs. Geneva: CERN, 2004. DOI: `10.5170/CERN-2004-003-V-1`. URL: `http://cds.cern.ch/record/782076`.

[15] ATLAS Collaboration. “Observation of a new particle in the search for the Standard Model Higgs boson with the ATLAS detector at the LHC.” In: *Phys. Lett. B* 716 (2012), pp. 1–29. DOI: `10.1016/j.physletb.2012.08.020`. arXiv: `1207.7214`. URL: `https://cds.cern.ch/record/1471031`.

[16] CMS Collaboration. “Observation of a new boson at a mass of 125 GeV with the CMS experiment at the LHC. Observation of a new boson at a mass of 125 GeV with the CMS experiment at the LHC”. In: *Phys. Lett. B* 716 (2012), pp. 30–61. DOI: `10.1016/j.physletb.2012.08.021`. arXiv: `1207.7235`. URL: `https://cds.cern.ch/record/1471016`.

[17] Emmy Noether. “Invariant variation problems”. In: *Transport Theory and Statistical Physics* 1.3 (Jan. 1971), pp. 186–207. DOI: `10.1080/00411457108231446`. URL: `https://doi.org/10.1080/00411457108231446`.

[18] ATLAS Collaboration. “Study of $WW\gamma$ and $WZ\gamma$ production in pp collisions at $\sqrt{s} = 8$ TeV and search for anomalous quartic gauge couplings with the ATLAS experiment”. In: *Eur. Phys. J. C* 77 (2017), p. 646. DOI: `10.1140/epjc/s10052-017-5180-3`. arXiv: `1707.05597 [hep-ex]`.

[19] ATLAS Collaboration. “The ATLAS Inner Detector commissioning and calibration.” In: *Eur. Phys. J. C* 70 (2010), 787–821. 34 p. DOI: `10.1140/epjc/s10052-010-1366-7`. arXiv: `1004.5293`. URL: `https://cds.cern.ch/record/1262789`.

[20] Martina Ressegotti. *Overview of the CMS detector performance at LHC Run 2*. Tech. rep. Geneva: CERN, 2019. DOI: `10.3390/universe5010018`. URL: `http://cds.cern.ch/record/2649417`.

[21] Kenneth Aamodt et al. “The ALICE experiment at the CERN LHC. A Large Ion Collider Experiment”. In: *JINST* 3 (2008), S08002. 259 p. DOI: `10.1088/1748-0221/3/08/S08002`. URL: `https://cds.cern.ch/record/1129812`.

[22] LHCb Collaboration. “The LHCb Detector at the LHC”. In: *JINST* 3 (2008), S08005. DOI: `10.1088/1748-0221/3/08/S08005`. URL: `https://cds.cern.ch/record/1129809`.

[23] R Schmidt. “Accelerator physics and technology of the LHC”. In: (1999). DOI: `10.5170/CERN-1999-001.7`. URL: `https://cds.cern.ch/record/450636`.

[24] S van der Meer. *Calibration of the effective beam height in the ISR*. Tech. rep. Geneva: CERN, 1968. URL: `https://cds.cern.ch/record/296752`.

[25] G Avoni et al. “The new LUCID-2 detector for luminosity measurement and monitoring in ATLAS”. In: *JINST* 13 (2018), P07017. 33 p. DOI: `10.1088/1748-0221/13/07/P07017`. URL: `http://cds.cern.ch/record/2633501`.

[26] ATLAS Collaboration. *Luminosity determination in pp collisions at $\sqrt{s} = 13$ TeV using the ATLAS detector at the LHC*. ATLAS-CONF-2019-021. 2019. URL: `https://cds.cern.ch/record/2677054`.

[27] Heinz Pernegger. *The Pixel Detector of the ATLAS Experiment for LHC Run-2*. Tech. rep. Geneva: CERN, 2015. DOI: 10.1088/1748-0221/10/06/C06012. URL: https://cds.cern.ch/record/1985432.

[28] M Capeans et al. *ATLAS Insertable B-Layer Technical Design Report*. Tech. rep. 2010. URL: https://cds.cern.ch/record/1291633.

[29] ATLAS Collaboration. "Production and Integration of the ATLAS Insertable B-Layer". In: *JINST* 13 (May 2018), T05008. 90 p. DOI: 10.1088/1748-0221/13/05/T05008. arXiv: 1803.00844. URL: https://cds.cern.ch/record/2307576.

[30] *Technical Design Report for the ATLAS Inner Tracker Strip Detector*. Tech. rep. Geneva: CERN, 2017. URL: https://cds.cern.ch/record/2257755.

[31] ATLAS Collaboration. "Performance of the ATLAS Transition Radiation Tracker in Run 1 of the LHC: tracker properties." In: *JINST* 12 (May 2017), P05002. 45 p. DOI: 10.1088/1748-0221/12/05/P05002. arXiv: 1702.06473. URL: https://cds.cern.ch/record/2253059.

[32] Bartosz Mindur. *ATLAS Transition Radiation Tracker (TRT): Straw tubes for tracking and particle identification at the Large Hadron Collider*. Tech. rep. Geneva: CERN, 2017. DOI: 10.1016/j.nima.2016.04.026. URL: https://cds.cern.ch/record/2139567.

[33] A Vogel. *ATLAS Transition Radiation Tracker (TRT): Straw Tube Gaseous Detectors at High Rates*. Tech. rep. Geneva: CERN, 2013. URL: https://cds.cern.ch/record/1537991.

[34] Steffen Starz. "ATLAS Calorimeter system: Run-2 performance, Phase-1 and Phase-2 upgrades". In: (2018). URL: https://cds.cern.ch/record/2628123.

[35] *ATLAS Liquid Argon Calorimeter Phase-II Upgrade: Technical Design Report*. Tech. rep. Geneva: CERN, 2017. DOI: 10.17181/CERN.6QIO.YGHO. URL: https://cds.cern.ch/record/2285582.

[36] Nikiforos Nikiforou. *Performance of the ATLAS Liquid Argon Calorimeter after three years of LHC operation and plans for a future upgrade*. Tech. rep. 2013. DOI: `10.1109/ANIMMA.2013.6728060`. arXiv: `1306.6756`. URL: `https://cds.cern.ch/record/1558820`.

[37] Pavol Bartos. *Performance of the ATLAS hadronic Tile calorimeter*. Tech. rep. Geneva: CERN, 2016. DOI: `10.22323/1.276.0204`. URL: `https://cds.cern.ch/record/2211419`.

[38] *ATLAS tile calorimeter: Technical Design Report*. Technical design report. ATLAS. Geneva: CERN, 1996. DOI: `10.17181/CERN.JRBJ.7028`. URL: `https://cds.cern.ch/record/331062`.

[39] L Pontecorvo. “The ATLAS Muon Spectrometer”. In: (2004). DOI: `10.1140/epjcd/s2004-04-013-y`. URL: `https://cds.cern.ch/record/676896`.

[40] *ATLAS muon spectrometer: Technical Design Report*. Technical design report. ATLAS. Geneva: CERN, 1997. URL: `https://cds.cern.ch/record/331068`.

[41] *ATLAS magnet system: Technical Design Report, 1*. Technical design report. ATLAS. Geneva: CERN, 1997. DOI: `10.17181/CERN.905C.VDTM`. URL: `https://cds.cern.ch/record/338080`.

[42] ATLAS Collaboration. “Performance of the ATLAS Trigger System in 2015. Performance of the ATLAS Trigger System in 2015”. In: *Eur. Phys. J. C* 77 (May 2017), 317. 76 p. DOI: `10.1140/epjc/s10052-017-4852-3`. arXiv: `1611.09661`. URL: `https://cds.cern.ch/record/2235584`.

[43] ATLAS Collaboration. “Performance of the ATLAS trigger system in 2015”. In: *Eur. Phys. J. C* 77 (2017), p. 317. DOI: `10.1140/epjc/s10052-017-4852-3`. arXiv: `1611.09661 [hep-ex]`.

[44] ATLAS Collaboration. *2015 start-up trigger menu and initial performance assessment of the ATLAS trigger using Run-2 data*. ATL-DAQ-PUB-2016-001. 2016. URL: https://cds.cern.ch/record/2136007.

[45] ATLAS Collaboration. *Trigger Menu in 2016*. ATL-DAQ-PUB-2017-001. 2017. URL: https://cds.cern.ch/record/2242069.

[46] ATLAS Collaboration. *Trigger Menu in 2017*. ATL-DAQ-PUB-2018-002. 2018. URL: https://cds.cern.ch/record/2625986.

[47] ATLAS Collaboration. "Electron and photon energy calibration with the ATLAS detector using 2015-2016 LHC proton-proton collision data". In: 14 (Tues 2019), P03017.61p. DOI: 10.1088/1748-0221/14/03/P03017. arXiv: 1812.03848. URL: https://cds.cern.ch/record/2650720.

[48] ATLAS Collaboration. "Muon reconstruction performance of the ATLAS detector in proton–proton collision data at $\sqrt{s} = 13\,\mathrm{TeV}$". In: *Eur. Phys. J. C* 76 (2016), p. 292. DOI: 10.1140/epjc/s10052-016-4120-y. arXiv: 1603.05598 [hep-ex].

[49] ATLAS Collaboration. "Muon reconstruction and identification efficiency in ATLAS using the full Run 2 *pp* collision data set at $\sqrt{s} = 13$ TeV". In: *Eur. Phys. J., C* 81 (July 2021), 578. 44 p. DOI: 10.1140/epjc/s10052-021-09233-2. arXiv: 2012.00578. URL: http://cds.cern.ch/record/2746302.

[50] ATLAS Collaboration. "Muon reconstruction performance of the ATLAS detector in proton–proton collision data at $\sqrt{s}$=13 TeV." In: *Eur. Phys. J. C* 76 (May 2016), 292. 45 p. DOI: 10.1140/epjc/s10052-016-4120-y. arXiv: 1603.05598. URL: https://cds.cern.ch/record/2139897.

[51] ATLAS Collaboration. "Measurement of the photon identification efficiencies with the ATLAS detector using LHC Run 2 data collected in 2015 and 2016". In: *Eur. Phys. J. C* 79 (Tues 2019), 205.55p. DOI: 10.1140/epjc/s10052-019-6650-6. arXiv: 1810.05087. URL: https://cds.cern.ch/record/2643391.

[52] Matteo Cacciari, Gavin P Salam, and Gregory Soyez. "The anti-k_t jet clustering algorithm". In: *Journal of High Energy Physics* 2008.04 (Apr. 2008), pp. 063–063. DOI: 10.1088/1126-6708/2008/04/063. URL: https://doi.org/10.1088/1126-6708/2008/04/063.

[53] ATLAS Collaboration. "Jet reconstruction and performance using particle flow with the ATLAS Detector." In: *Eur. Phys. J. C* 77 (July 2017), 466. 67 p. DOI: 10.1140/epjc/s10052-017-5031-2. arXiv: 1703.10485. URL: https://cds.cern.ch/record/2257597.

[54] ATLAS Collaboration. *Tagging and suppression of pileup jets with the ATLAS detector.* ATLAS-CONF-2014-018. 2014. URL: https://cds.cern.ch/record/1700870.

[55] ATLAS Collaboration. "Jet energy scale measurements and their systematic uncertainties in proton-proton collisions at $\sqrt{s} = 13$ TeV with the ATLAS detector." In: *Phys. Rev. D* 96 (Oct. 2017), 072002. 36 p. DOI: 10.1103/PhysRevD.96.072002. arXiv: 1703.09665. URL: https://cds.cern.ch/record/2257300.

[56] *Graph Neural Network Jet Flavour Tagging with the ATLAS Detector.* Tech. rep. Geneva: CERN, 2022. URL: https://cds.cern.ch/record/2811135.

[57] ATLAS Collaboration. *E_T^{miss} performance in the ATLAS detector using 2015–2016 LHC pp collisions.* ATLAS-CONF-2018-023. 2018. URL: https://cds.cern.ch/record/2625233.

[58] ATLAS Collaboration. "Performance of missing transverse momentum reconstruction with the ATLAS detector using proton-proton collisions at $\sqrt{s} = 13$ TeV". In: *Eur. Phys. J. C* 78 (Nov. 2018), 903. 66 p. DOI: 10.1140/epjc/s10052-018-6288-9. arXiv: 1802.08168. URL: https://cds.cern.ch/record/2305380.

[59] ATLAS Collaboration. "The ATLAS Simulation Infrastructure." In: *Eur. Phys. J. C* 70 (2010), 823–874. 53 p. DOI: 10.1140/epjc/s10052-010-1429-9. arXiv: 1005.4568. URL: https://cds.cern.ch/record/1267853.

[60] S. Agostinelli et al. “GEANT4 – a simulation toolkit”. In: *Nucl. Instrum. Meth. A* 506 (2003), p. 250. DOI: 10.1016/S0168-9002(03)01368-8.

[61] Coll ATLAS et al. *The simulation principle and performance of the ATLAS fast calorimeter simulation FastCaloSim*. Tech. rep. Geneva: CERN, 2010. URL: https://cds.cern.ch/record/1300517.

[62] ATLAS Collaboration. *Further ATLAS tunes of* PYTHIA *6 and Pythia 8*. ATL-PHYS-PUB-2011-014. 2011. URL: https://cds.cern.ch/record/1400677.

[63] Enrico Bothmann et al. “Event Generation with Sherpa 2.2”. In: *SciPost Phys.* 7.3 (2019), p. 034. DOI: 10.21468/SciPostPhys.7.3.034. arXiv: 1905.09127 [hep-ph].

[64] J. Alwall et al. “The automated computation of tree-level and next-to-leading order differential cross sections, and their matching to parton shower simulations”. In: *JHEP* 07 (2014), p. 079. DOI: 10.1007/JHEP07(2014)079. arXiv: 1405.0301 [hep-ph].

[65] Richard D. Ball et al. “Parton distributions for the LHC Run II”. In: *JHEP* 04 (2015), p. 040. DOI: 10.1007/JHEP04(2015)040. arXiv: 1410.8849 [hep-ph].

[66] Torbjörn Sjöstrand et al. “An introduction to PYTHIA 8.2”. In: *Comput. Phys. Commun.* 191 (2015), p. 159. DOI: 10.1016/j.cpc.2015.01.024. arXiv: 1410.3012 [hep-ph].

[67] ATLAS Collaboration. *ATLAS Pythia 8 tunes to* 7 *TeV data*. ATL-PHYS-PUB-2014-021. 2014. URL: https://cds.cern.ch/record/1966419.

[68] Stefano Frixione et al. “Angular correlations of lepton pairs from vector boson and top quark decays in Monte Carlo simulations”. In: *JHEP* 04 (2007), p. 081. DOI: 10.1088/1126-6708/2007/04/081. arXiv: hep-ph/0702198.

[69] Pierre Artoisenet et al. “Automatic spin-entangled decays of heavy resonances in Monte Carlo simulations”. In: *JHEP* 03 (2013), p. 015. DOI: 10.1007/JHEP03(2013)015. arXiv: 1212.3460 [hep-ph].

[70] Federico Buccioni et al. “OpenLoops 2”. In: *Eur. Phys. J. C* 79.10 (2019), p. 866. DOI: `10.1140/epjc/s10052-019-7306-2`. arXiv: `1907.13071 [hep-ph]`.

[71] Fabio Cascioli, Philipp Maierhofer, and Stefano Pozzorini. “Scattering Amplitudes with Open Loops”. In: *Phys. Rev. Lett.* 108 (2012), p. 111601. DOI: `10.1103/PhysRevLett.108.111601`. arXiv: `1111.5206 [hep-ph]`.

[72] Ansgar Denner, Stefan Dittmaier, and Lars Hofer. “COLLIER: A fortran-based complex one-loop library in extended regularizations”. In: *Comput. Phys. Commun.* 212 (2017), pp. 220–238. DOI: `10.1016/j.cpc.2016.10.013`. arXiv: `1604.06792 [hep-ph]`.

[73] Stefano Frixione, Paolo Nason, and Giovanni Ridolfi. “A Positive-weight next-to-leading-order Monte Carlo for heavy flavour hadroproduction”. In: *JHEP* 09 (2007), p. 126. DOI: `10.1088/1126-6708/2007/09/126`. arXiv: `0707.3088 [hep-ph]`.

[74] Paolo Nason. “A new method for combining NLO QCD with shower Monte Carlo algorithms”. In: *JHEP* 11 (2004), p. 040. DOI: `10.1088/1126-6708/2004/11/040`. arXiv: `hep-ph/0409146`.

[75] Stefano Frixione, Paolo Nason, and Carlo Oleari. “Matching NLO QCD computations with parton shower simulations: the POWHEG method”. In: *JHEP* 11 (2007), p. 070. DOI: `10.1088/1126-6708/2007/11/070`. arXiv: `0709.2092 [hep-ph]`.

[76] Simone Alioli et al. “A general framework for implementing NLO calculations in shower Monte Carlo programs: the POWHEG BOX”. In: *JHEP* 06 (2010), p. 043. DOI: `10.1007/JHEP06(2010)043`. arXiv: `1002.2581 [hep-ph]`.

[77] Charalampos Anastasiou et al. “High precision QCD at hadron colliders: Electroweak gauge boson rapidity distributions at NNLO”. In: *Phys. Rev. D* 69 (2004), p. 094008. DOI: `10.1103/PhysRevD.69.094008`. arXiv: `hep-ph/0312266`.

[78] Tanju Gleisberg and Stefan Höche. “Comix, a new matrix element generator”. In: *JHEP* 12 (2008), p. 039. DOI: `10.1088/1126-6708/2008/12/039`. arXiv: `0808.3674 [hep-ph]`.

[79] G. Avoni et al. "The new LUCID-2 detector for luminosity measurement and monitoring in ATLAS". In: *JINST* 13.07 (2018), P07017. DOI: 10.1088/1748-0221/13/07/P07017.

[80] Z Marshall. *Simulation of Pile-up in the ATLAS Experiment.* Tech. rep. Geneva: CERN, 2014. DOI: 10.1088/1742-6596/513/2/022024. URL: https://cds.cern.ch/record/1616394.

[81] ATLAS Collaboration. *Electron efficiency measurements with the ATLAS detector using the 2015 LHC proton–proton collision data.* ATLAS-CONF-2016-024. 2016. URL: https://cds.cern.ch/record/2157687.

[82] ATLAS Collaboration. "Electron and photon performance measurements with the ATLAS detector using the 2015-2017 LHC proton-proton collision data". In: *JINST* 14 (Dec. 2019), P12006. 70 p. DOI: 10.1088/1748-0221/14/12/P12006. arXiv: 1908.00005. URL: https://cds.cern.ch/record/2684552.

[83] ATLAS Collaboration. "Electron and photon energy calibration with the ATLAS detector using LHC Run 1 data." In: *Eur. Phys. J. C* C74 (Oct. 2014), 3071. 48 p. DOI: 10.1140/epjc/s10052-014-3071-4. arXiv: 1407.5063. URL: https://cds.cern.ch/record/1744017.

[84] ATLAS Collaboration. *Photon identification in 2015 ATLAS data.* ATL-PHYS-PUB-2016-014. 2016. URL: https://cds.cern.ch/record/2203125.

[85] ATLAS Collaboration. "Jet energy scale measurements and their systematic uncertainties in proton–proton collisions at $\sqrt{s} = 13\,\text{TeV}$ with the ATLAS detector". In: *Phys. Rev. D* 96 (2017), p. 072002. DOI: 10.1103/PhysRevD.96.072002. arXiv: 1703.09665 [hep-ex].

[86] ATLAS Collaboration. "Jet energy resolution in proton-proton collisions at $\sqrt{s} = 7$ TeV recorded in 2010 with the ATLAS detector." In: *Eur. Phys. J. C* 73 (Mar. 2013),

2306. 13 p. DOI: 10.1140/epjc/s10052-013-2306-0. arXiv: 1210.6210. URL: https://cds.cern.ch/record/1489592.

[87] James Ferrando et al. *Measurement of the b-jet identification efficiency with $t\bar{t}$ events using an improved likelihood method: Calibration INT note of ANA-FTAG-2018-01*. Tech. rep. ATL-COM-PHYS-2018-1072. Geneva: CERN, June 2018. URL: https://cds.cern.ch/record/2631547.

[88] ATLAS Collaboration. *Measurement of b-tagging efficiency of c-jets in $t\bar{t}$ events using a likelihood approach with the ATLAS detector*. ATLAS-CONF-2018-001. 2018. URL: https://cds.cern.ch/record/2306649.

[89] ATLAS Collaboration. *Calibration of light-flavour b-jet mistagging rates using ATLAS proton–proton collision data at $\sqrt{s} = 13$ TeV*. ATLAS-CONF-2018-006. 2018. URL: https://cds.cern.ch/record/2314418.

[90] Benjamin Brunt et al. *Performance of missing transverse momentum reconstruction with the ATLAS detector using proton-proton collisions at $\sqrt{s} = 13$ TeV*. Tech. rep. Geneva: CERN, 2016. URL: https://cds.cern.ch/record/2149445.

[91] ATLAS Collaboration. “Performance of missing transverse momentum reconstruction with the ATLAS detector using proton–proton collisions at $\sqrt{s} = 13\,\text{TeV}$”. In: *Eur. Phys. J. C* 78 (2018), p. 903. DOI: 10.1140/epjc/s10052-018-6288-9. arXiv: 1802.08168 [hep-ex].

[92] Tianqi Chen and Carlos Guestrin. “XGBoost: A Scalable Tree Boosting System”. In: *Proceedings of the 22nd ACM SIGKDD International Conference on Knowledge Discovery and Data Mining*. KDD ’16. San Francisco, California, USA: ACM, 2016, pp. 785–794. ISBN: 978-1-4503-4232-2. DOI: 10.1145/2939672.2939785. URL: http://doi.acm.org/10.1145/2939672.2939785.

[93] *TRExFitter*. URL: https://twiki.cern.ch/twiki/bin/viewauth/AtlasProtected/TtHFitter.

Appendices

Appendix A

Additional plots

This section summarizes the different regions considered in the analysis presented in this thesis. Table A.1 provides the definitions for each of the different regions. For each control or validation region, the cuts that make the region orthogonal to the $e^{\pm}\mu^{\mp}\gamma$ SR are given in bold. For each region, yields and pre-fit and post-fit distributions for several variables are provided. Information on the fit and the BDT are provided in a later section of this thesis.

Cut	$e^{\pm}\mu^{\mp}\gamma$ SR	$t\bar{t}\gamma$ CR	$Z\gamma$ CR	Zjets CR	VV CR
Leptons	$e^{\pm}\mu^{\mp}$	$e^{\pm}\mu^{\mp}$	**$e^{\pm}e^{\mp}$ or $\mu^{\pm}\mu^{\mp}$**	**$e^{\pm}e^{\mp}$ or $\mu^{\pm}\mu^{\mp}$**	$e^{\pm}\mu^{\mp}$
N(γ)	1	1	1	1	1
Leading lepton p_{T}	> 27 GeV	> 27 GeV	> 27 GeV	> 27 GeV	> 27 GeV
E_T^{miss}	> 20 GeV	> 20 GeV	> 20 GeV	> 20 GeV	> 20 GeV
$\lvert m(e,y) - m_Z \rvert$	> 5 GeV	> 5 GeV	–	–	**< 5 GeV**
$m(\ell\ell\gamma)$	–	–	**< 100 GeV**	**> 100 GeV**	–
N(b-Jets)	0	**1**	0	0	0

Table A.1: Definition of each region considered in the analysis. Cuts that cause each region to be orthogonal to the signal region are given in bold.

A.1 Additional $e^{\pm}\mu^{\mp}\gamma$ plots and tables

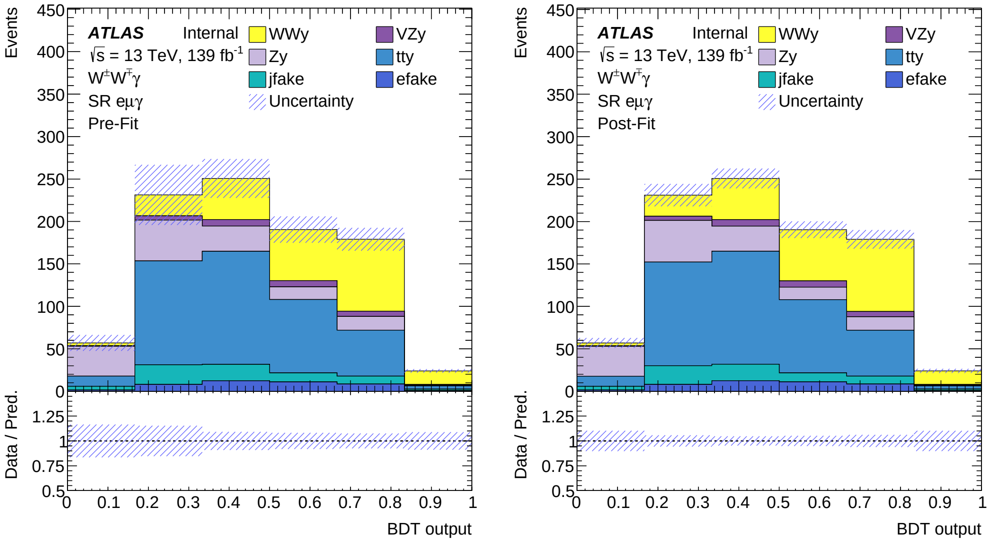

Figure A.1: Distributions of the BDT score applied to the events in the $e^{\pm}\mu^{\mp}\gamma$ signal region (Left) pre-fit (right) post-fit. The uncertainties indicated in the figures include both statistical and systematic uncertainties. The post-fit result is obtained from the binned maximum likelihood fit with Asimov data and is described in Section 11.2.2.

Pre-fit	
$W^{\pm}W^{\mp}\gamma$	237.14 ± 11.19
$VZ\gamma$	27.84 ± 5.68
$Z\gamma$	144.76 ± 25.71
$t\bar{t}\gamma$	411.82 ± 36.32
jet → γ	68.59 ± 34.11
$e \rightarrow \gamma$	42.12 ± 3.14
Total	932.27 ± 62.98

Table A.2: Pre-fit event yields in the $e^{\pm}\mu^{\mp}\gamma$ signal region. Uncertainties include statistical and systematic uncertainties.

Post-fit	
$W^{\pm}W^{\mp}\gamma$	237.97 ± 34.69
$VZ\gamma$	27.85 ± 5.64
$Z\gamma$	145.13 ± 13.32
$t\bar{t}\gamma$	411.39 ± 29.00
jet → γ	67.55 ± 23.77
$e \rightarrow \gamma$	42.27 ± 6.46
Total	932.15 ± 29.07

Table A.3: Post-fit event yields in the $e^{\pm}\mu^{\mp}\gamma$ signal region. Uncertainties include statistical and systematic uncertainties.

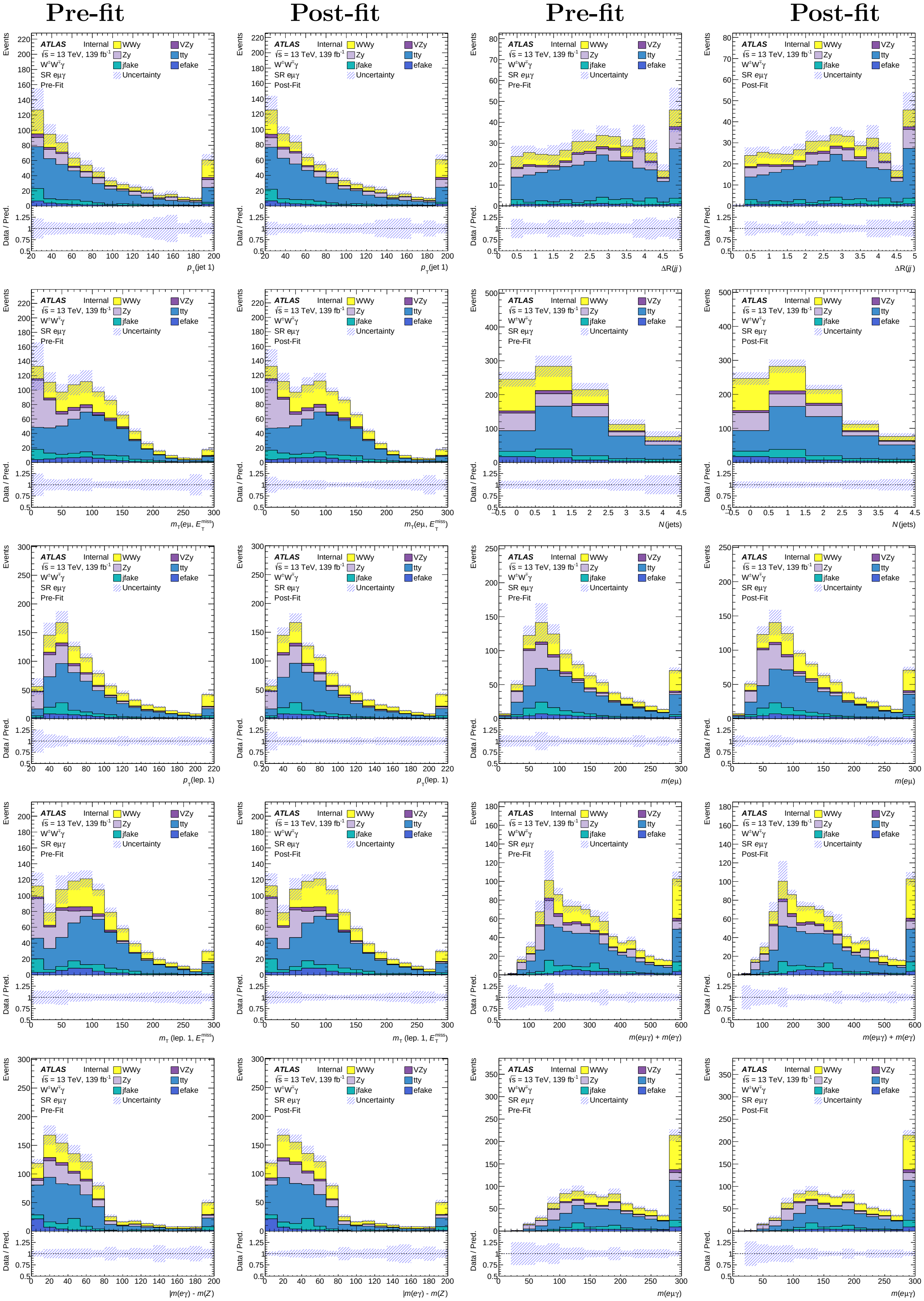

Figure A.2: Distributions of the various variables for events in the $e^{\pm}\mu^{\mp}\gamma$ signal region (Left) pre-fit (right) post-fit. The uncertainties indicated in the figures include both statistical and systematic uncertainties. The post-fit result is obtained from the binned maximum likelihood fit with Asimov data and is described in Section 11.2.2.

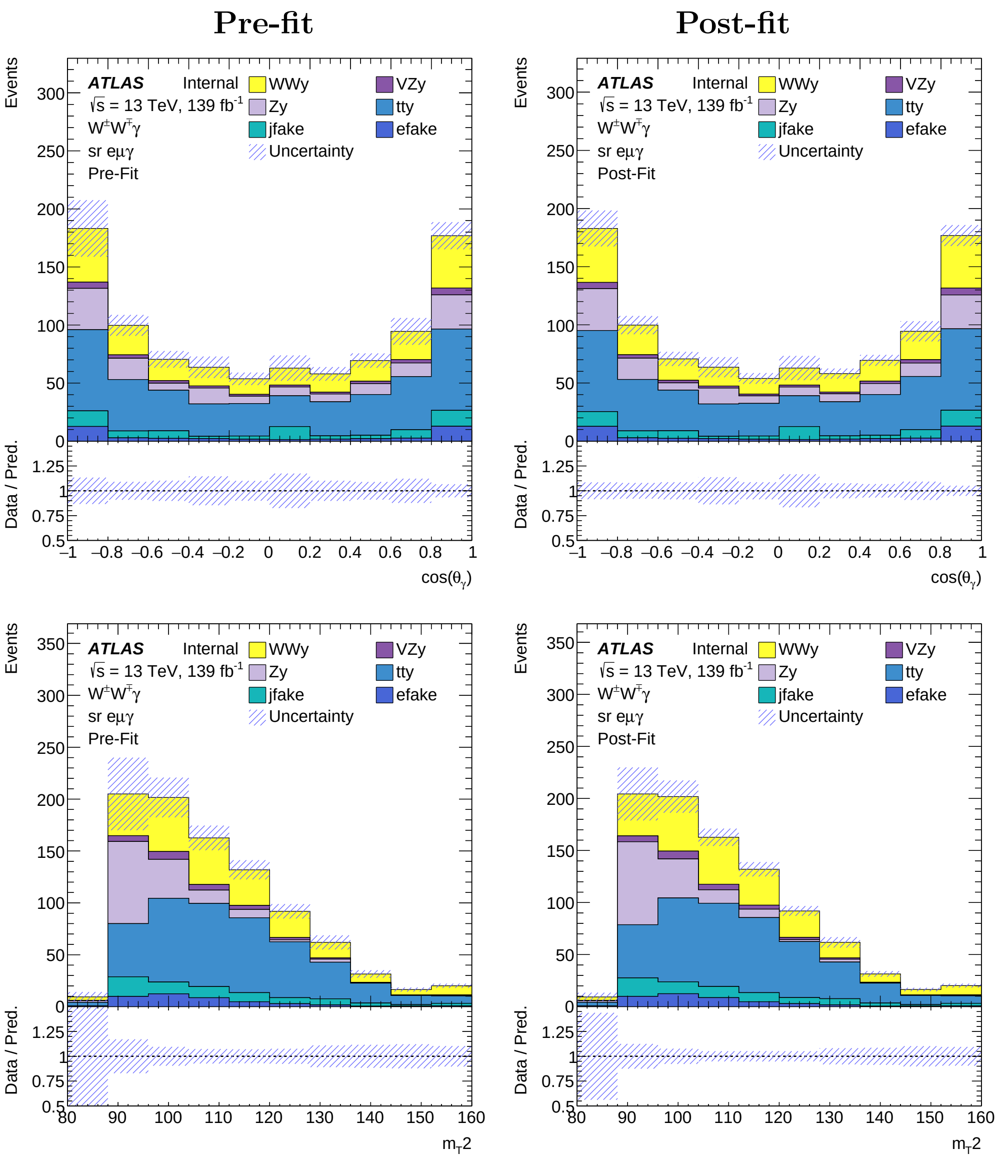

Figure A.3: Pre-fit (left)and post-fit (right) distributions of $\cos(\theta) = \tanh(\eta)$ of the photon (top) and the stransverse mass, $m_{\mathrm{T}}2$ (bottom). The uncertainties indicated in the figures include both statistical and systematic uncertainties. The post-fit result is obtained from the binned maximum likelihood fit with Asimov data and is described in Section 11.2.2.

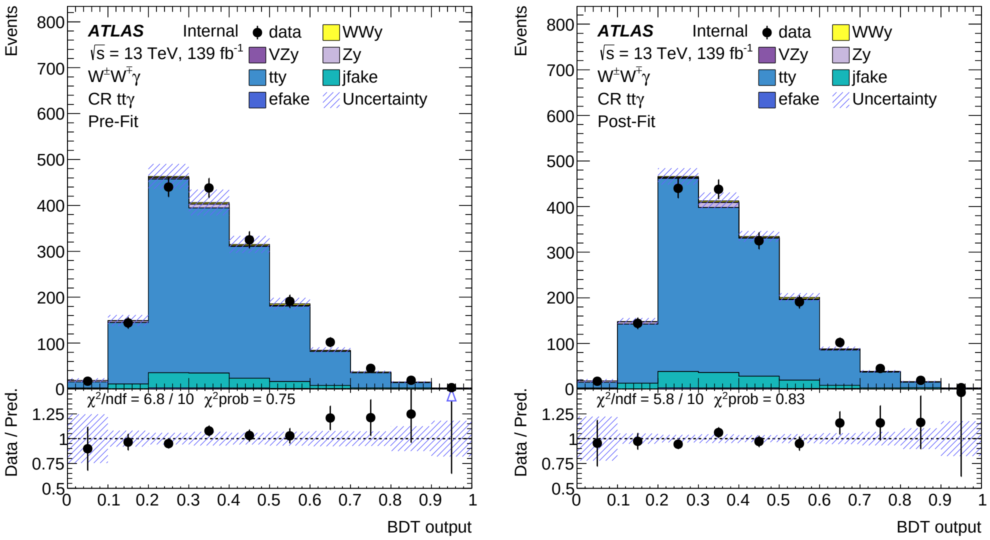

Figure A.4: Distributions of the BDT score applied to the events in $t\bar{t}\gamma$ control region (Left) pre-fit (right) post-fit. The uncertainties indicated in the figures include both statistical and systematic uncertainties. The post-fit result is obtained from the binned maximum likelihood fit with the control regions to data and is described in Section 11.2.1.

A.2 Additional $t\bar{t}\gamma$ plots and tables

Pre-fit	
$W^{\pm}W^{\mp}\gamma$	17.52 ± 2.17
$VZ\gamma$	3.53 ± 0.78
$Z\gamma$	21.02 ± 11.41
$t\bar{t}\gamma$	1552.31 ± 59.14
jet $\rightarrow \gamma$	125.78 ± 53.92
$e \rightarrow \gamma$	9.62 ± 1.14
Total	1729.78 ± 83.62
data	1724

Table A.4: Pre-fit event yields in the $t\bar{t}\gamma$ control region. Uncertainties include statistical and systematic uncertainties.

Post-fit	
$W^{\pm}W^{\mp}\gamma$	17.60 ± 3.28
$VZ\gamma$	3.53 ± 0.75
$Z\gamma$	21.21 ± 5.72
$t\bar{t}\gamma$	1551.03 ± 67.13
jet $\rightarrow \gamma$	126.17 ± 51.83
$e \rightarrow \gamma$	9.65 ± 1.48
Total	1729.18 ± 41.15
data	1724

Table A.5: Post-fit event yields in the $t\bar{t}\gamma$ control region. Uncertainties include statistical and systematic uncertainties.

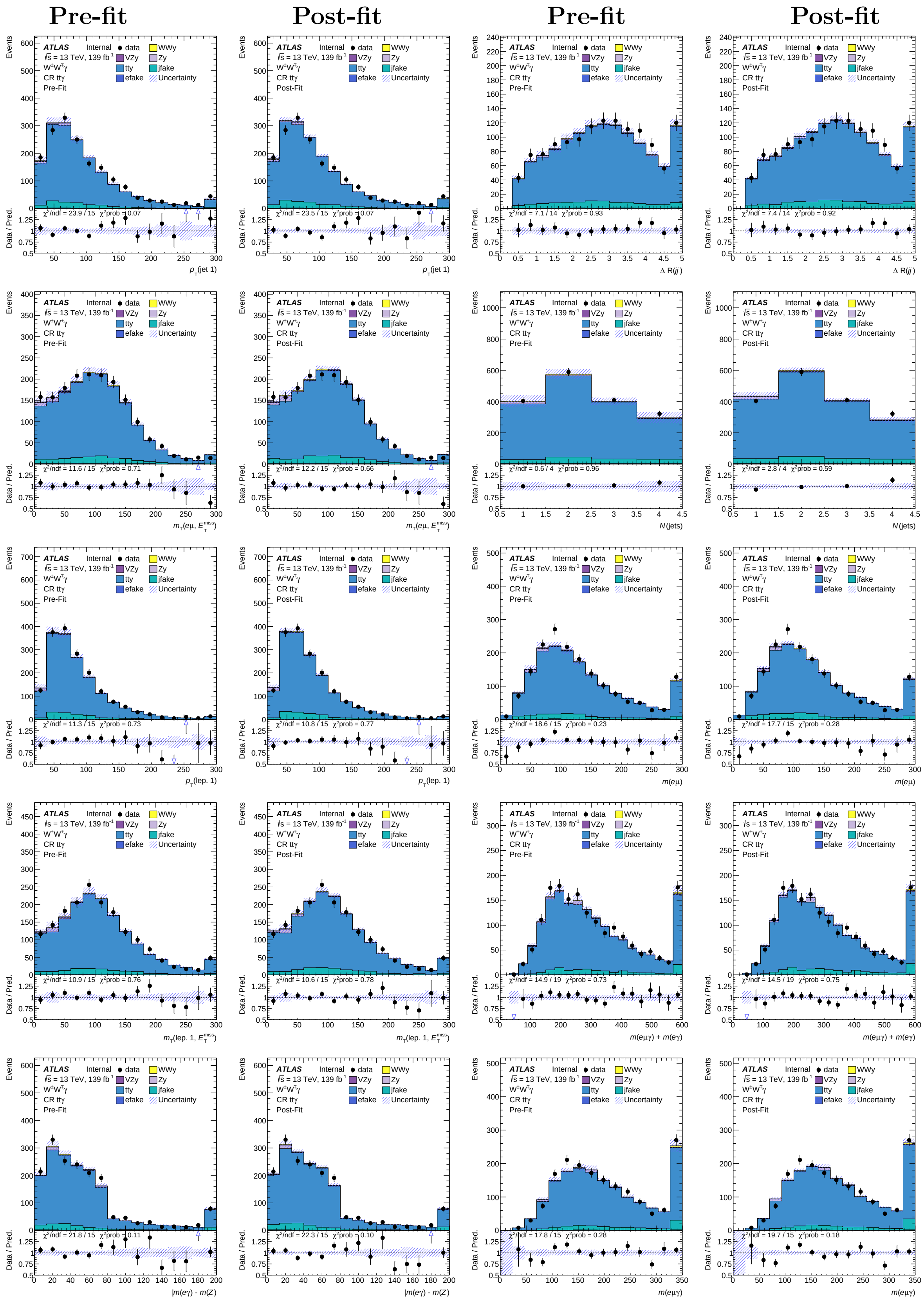

Figure A.5: Distributions of the various variables for events in the $t\bar{t}\gamma$ control region (Left) pre-fit (right) post-fit. The uncertainties indicated in the figures include both statistical and systematic uncertainties. The post-fit result is obtained from the binned maximum likelihood fit with the control regions to data and is described in Section 11.2.1.

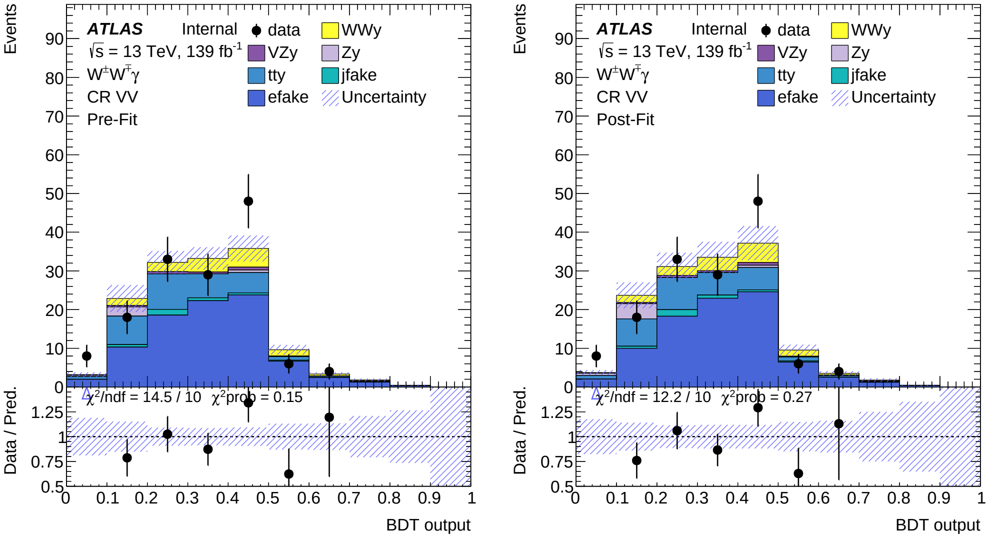

Figure A.6: Distributions of the BDT score applied to the events in the VV control region (Left) pre-fit (right) post-fit. The uncertainties indicated in the figures include both statistical and systematic uncertainties. The post-fit result is obtained from the binned maximum likelihood fit with the control regions to data and is described in Section 11.2.1.

A.3 Additional VV plots and tables

Pre-fit	
$W^{\pm}W^{\mp}\gamma$	15.10 ± 0.75
$VZ\gamma$	2.44 ± 0.52
$Z\gamma$	3.56 ± 2.47
$t\bar{t}\gamma$	31.06 ± 3.41
jet $\rightarrow \gamma$	3.86 ± 1.52
$e \rightarrow \gamma$	88.52 ± 6.48
Total	144.54 ± 8.53
data	146

Table A.6: Pre-fit event yields in the VV control region. Uncertainties include statistical and systematic uncertainties.

Post-fit	
$W^{\pm}W^{\mp}\gamma$	15.15 ± 2.26
$VZ\gamma$	2.44 ± 0.50
$Z\gamma$	3.66 ± 1.31
$t\bar{t}\gamma$	30.96 ± 2.72
jet $\rightarrow \gamma$	3.88 ± 1.19
$e \rightarrow \gamma$	88.81 ± 12.62
Total	144.91 ± 11.91
data	146

Table A.7: Post-fit event yields in the VV control region. Uncertainties include statistical and systematic uncertainties.

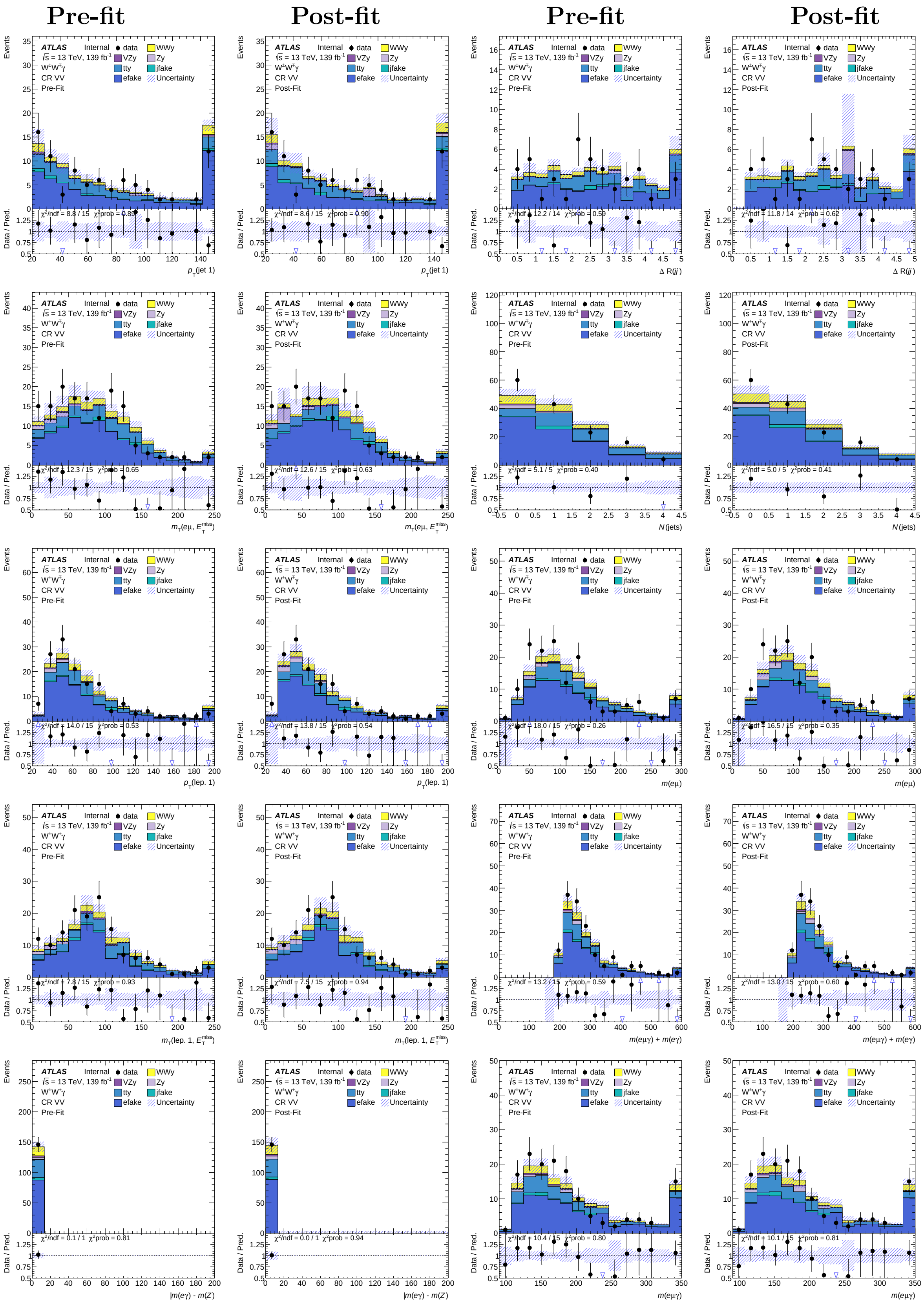

Figure A.7: Distributions of the various variables for events in the VV control region (Left) pre-fit (right) post-fit. The uncertainties indicated in the figures include both statistical and systematic uncertainties. The post-fit result is obtained from the binned maximum likelihood fit with the control regions to data and is described in Section 11.2.1.

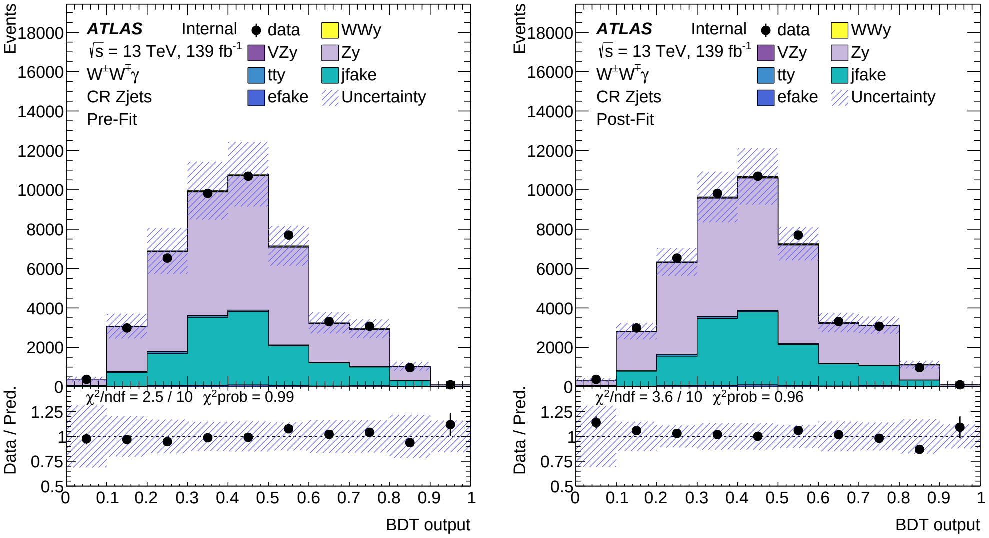

Figure A.8: Distributions of the BDT score applied to the events in Zjets validation region (Left) pre-fit (right) post-fit. The uncertainties indicated in the figures include both statistical and systematic uncertainties. The post-fit result is obtained from the binned maximum likelihood fit with the control regions to data and is described in Section 11.2.1.

A.4 Additional Zjets plots and tables

Pre-fit

$W^{\pm}W^{\mp}\gamma$	275.74 ± 12.36
$VZ\gamma$	108.67 ± 22.11
$Z\gamma$	30397.30 ± 3250.70
$t\bar{t}\gamma$	393.11 ± 34.52
jet $\rightarrow \gamma$	14011.90 ± 5276.79
$e \rightarrow \gamma$	404.48 ± 29.89
Total	45591.20 ± 6352.26
data	45570

Table A.8: Pre-fit event yields in the Zjets validation region. Uncertainties include statistical and systematic uncertainties.

Post-fit

$W^{\pm}W^{\mp}\gamma$	275.45 ± 12.09
$VZ\gamma$	108.61 ± 21.89
$Z\gamma$	29524.40 ± 889.24
$t\bar{t}\gamma$	395.28 ± 28.79
jet $\rightarrow \gamma$	13958.90 ± 5212.42
$e \rightarrow \gamma$	409.30 ± 60.13
Total	44672.00 ± 5187.86
data	45570

Table A.9: Post-fit event yields in the Zjets validation region. Uncertainties include statistical and systematic uncertainties.

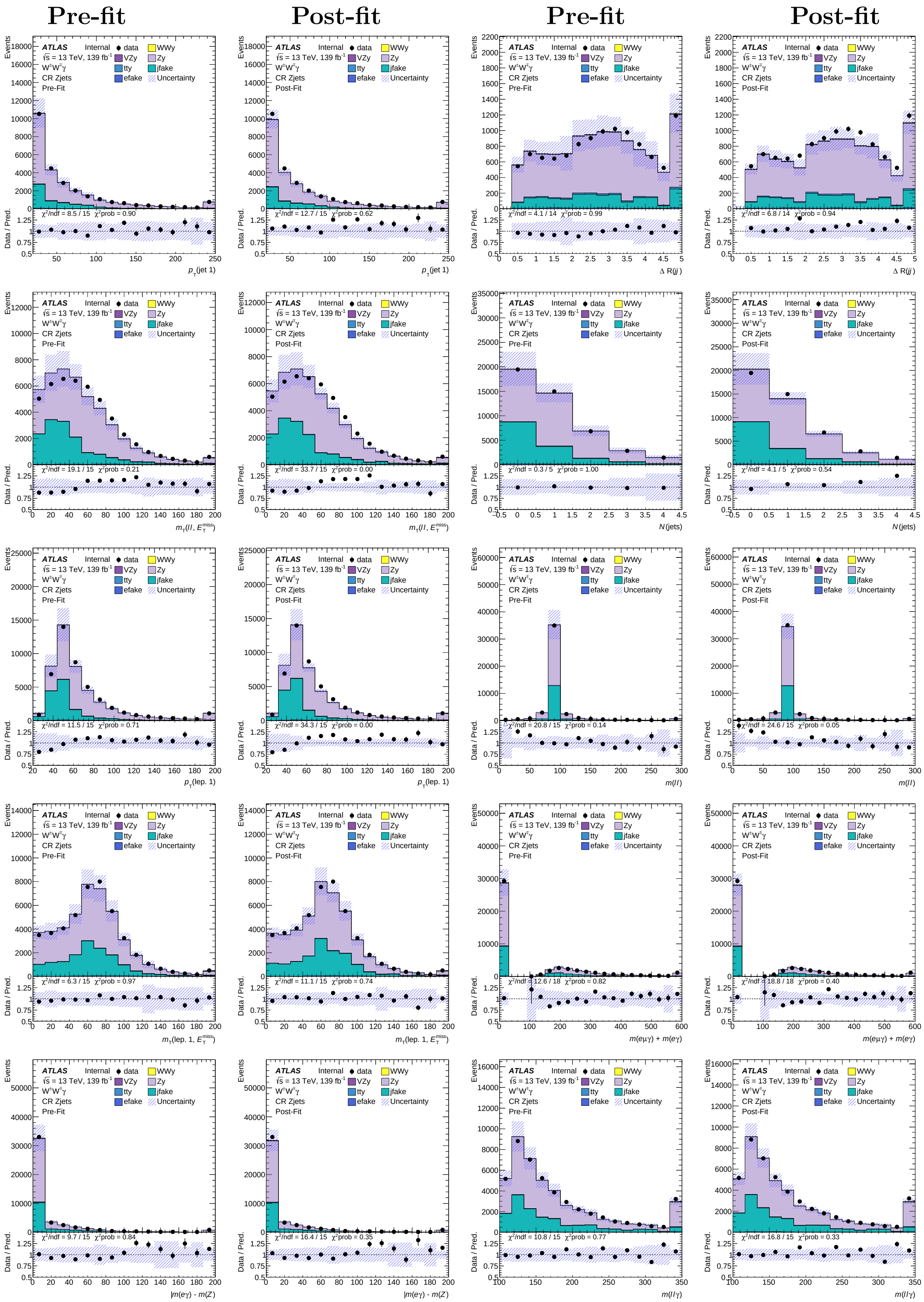

Figure A.9: Distributions of the various variables for events in the Zjets validation region (Left) pre-fit (right) post-fit. The uncertainties indicated in the figures include both statistical and systematic uncertainties. The post-fit result is obtained from the binned maximum likelihood fit with the control regions to data and is described in Section 11.2.1.

Pre-fit Post-fit Pre-fit Post-fit

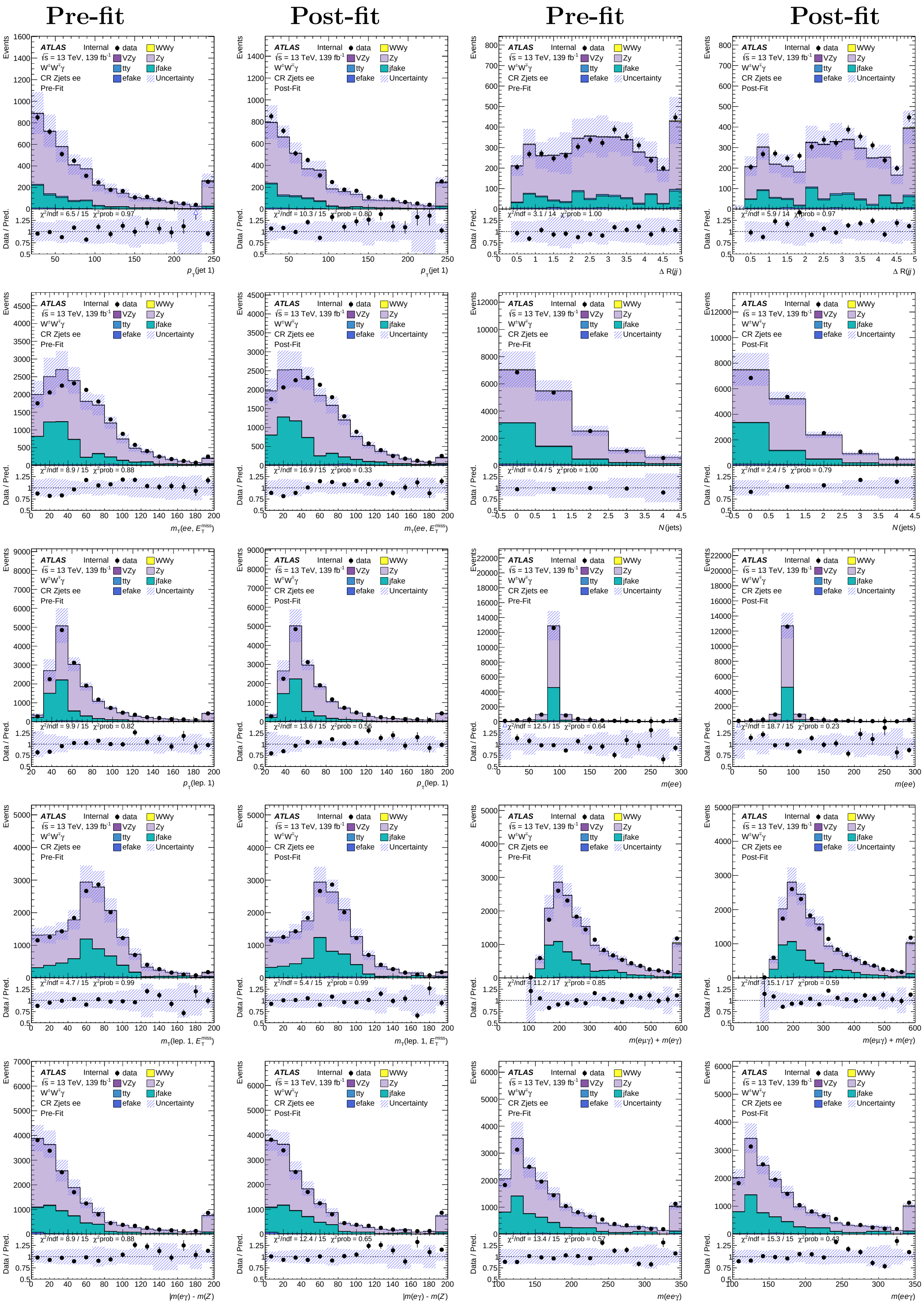

Figure A.10: Distributions of the various variables for events in the Zjets validation region with two electrons (Left) pre-fit (right) post-fit. The uncertainties indicated in the figures include both statistical and systematic uncertainties. The post-fit result is obtained from the binned maximum likelihood fit with the control regions to data and is described in Section 11.2.1.

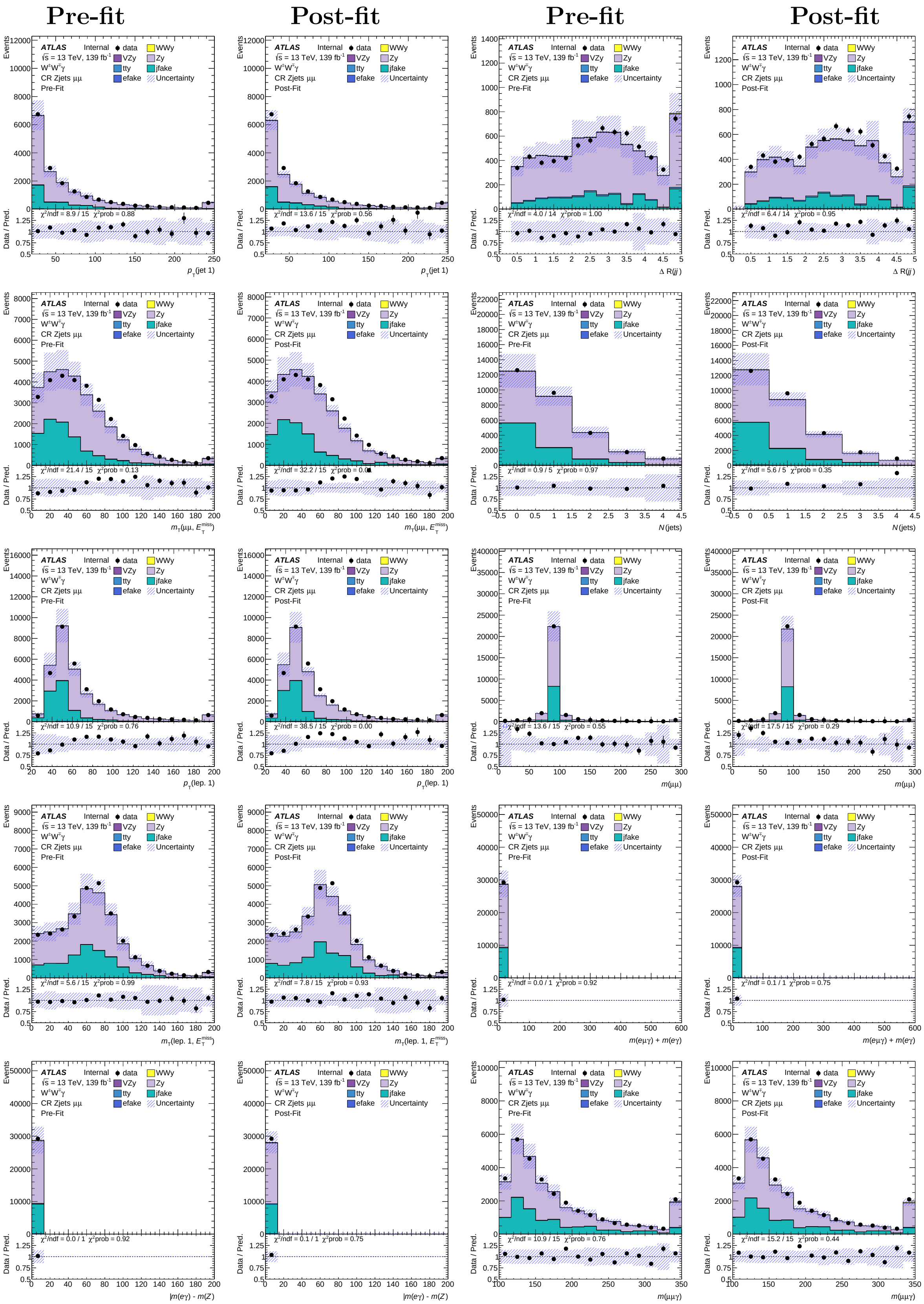

Figure A.11: Distributions of the various variables for events in the Zjets validation region with two muons (Left) pre-fit (right) post-fit. The uncertainties indicated in the figures include both statistical and systematic uncertainties. The post-fit result is obtained from the binned maximum likelihood fit with the control regions to data and is described in Section 11.2.1.

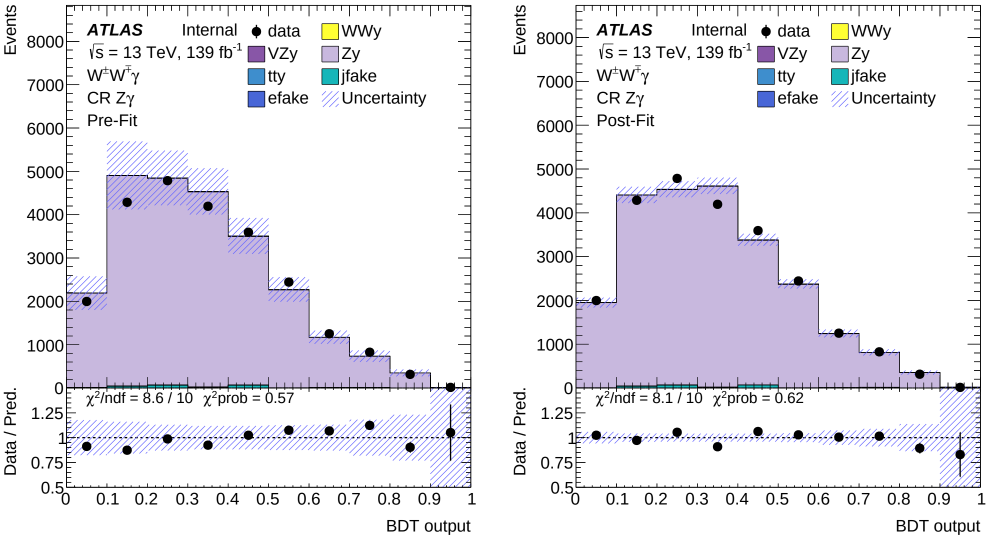

Figure A.12: Distributions of the BDT score applied to the events in $Z\gamma$ control region (Left) pre-fit (right) post-fit. The uncertainties indicated in the figures include both statistical and systematic uncertainties. The post-fit result is obtained from the binned maximum likelihood fit with the control regions to data and is described in Section 11.2.1.

A.5 Additional $Z\gamma$ plots and tables

Pre-fit	
$W^{\pm}W^{\mp}\gamma$	41.26 ± 2.02
$VZ\gamma$	31.57 ± 6.49
$Z\gamma$	24773.20 ± 2848.90
$t\bar{t}\gamma$	38.57 ± 5.34
jet → γ	198.89 ± 92.75
$e \to \gamma$	19.69 ± 6.60
Total	25103.20 ± 2851.84
data	23707

Table A.10: Pre-fit event yields in the $Z\gamma$ control region. Uncertainties include statistical and systematic uncertainties.

Post-fit	
$W^{\pm}W^{\mp}\gamma$	41.37 ± 6.07
$VZ\gamma$	31.56 ± 6.43
$Z\gamma$	24775.00 ± 173.87
$t\bar{t}\gamma$	38.37 ± 4.04
jet → γ	197.75 ± 69.14
$e \to \gamma$	19.94 ± 5.33
Total	25104.00 ± 158.66
data	23707

Table A.11: Post-fit event yields in the $Z\gamma$ control region. Uncertainties include statistical and systematic uncertainties.

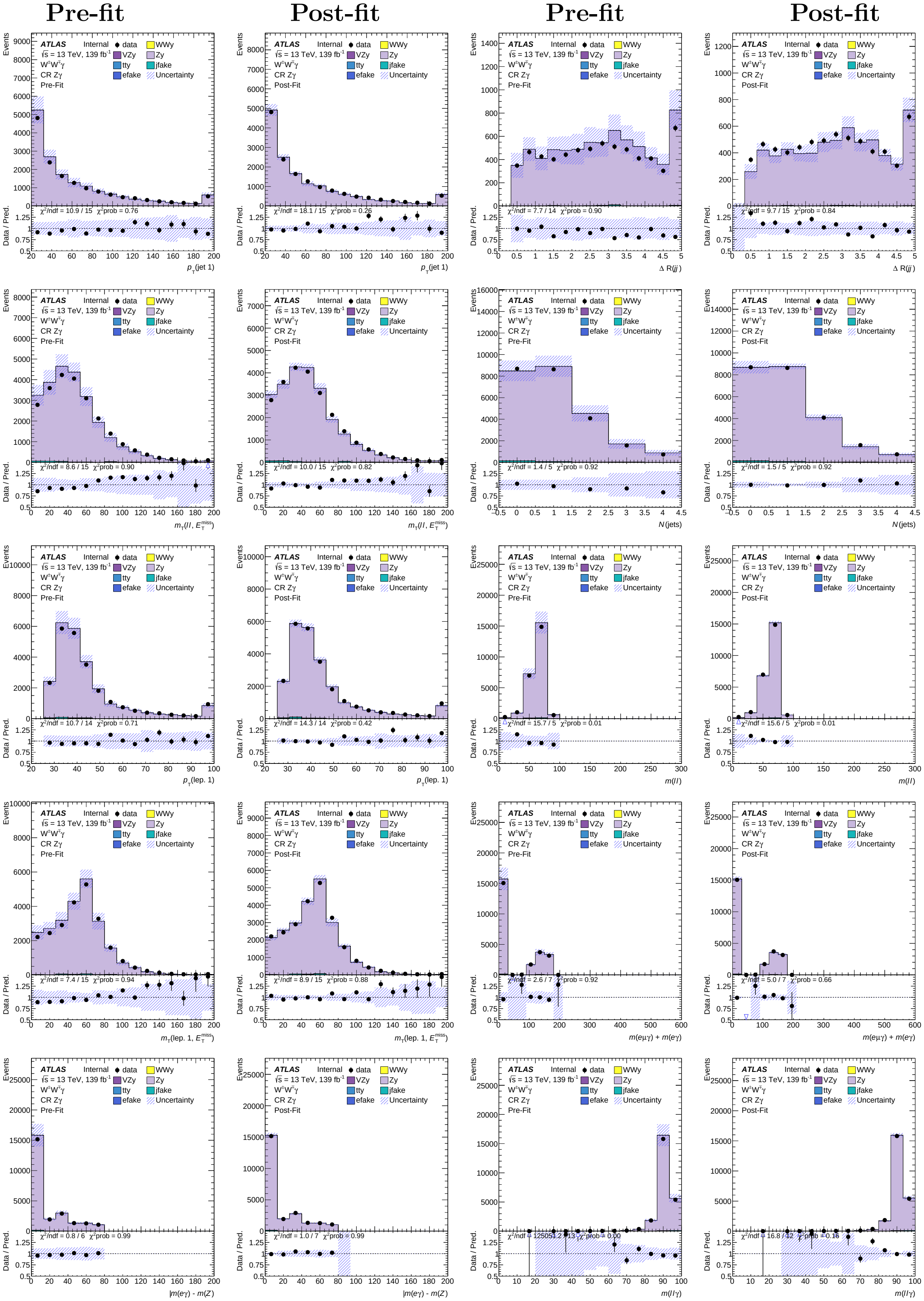

Figure A.13: Distributions of the various variables for events in the $Z\gamma$ control region (Left) pre-fit (right) post-fit. The uncertainties indicated in the figures include both statistical and systematic uncertainties. The post-fit result is obtained from the binned maximum likelihood fit with the control regions to data and is described in Section 11.2.1.

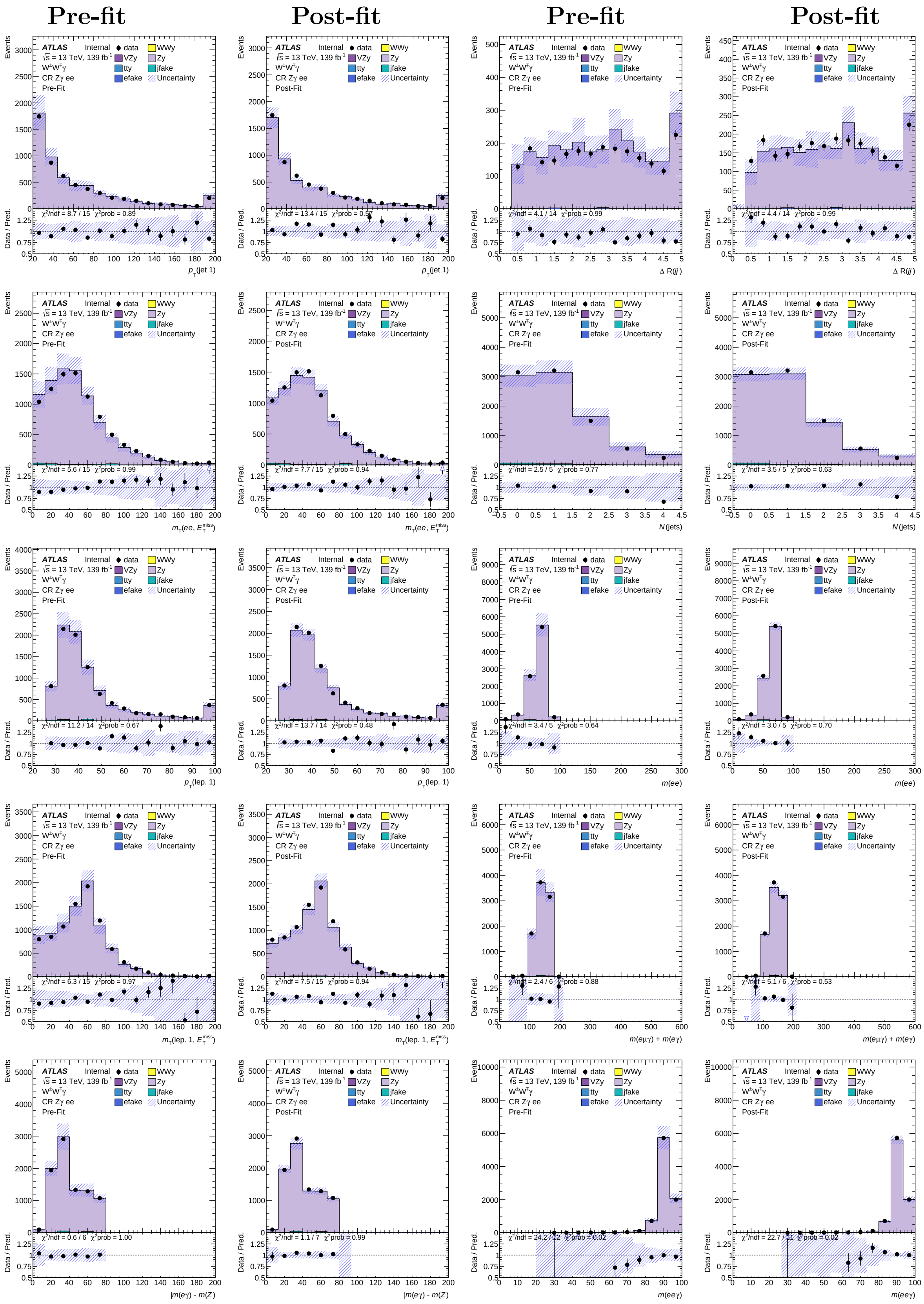

Figure A.14: Distributions of the various variables for events in the $Z\gamma$ control region with two electrons (Left) pre-fit (right) post-fit. The uncertainties indicated in the figures include both statistical and systematic uncertainties. The post-fit result is obtained from the binned maximum likelihood fit with the control regions to data and is described in Section 11.2.1.

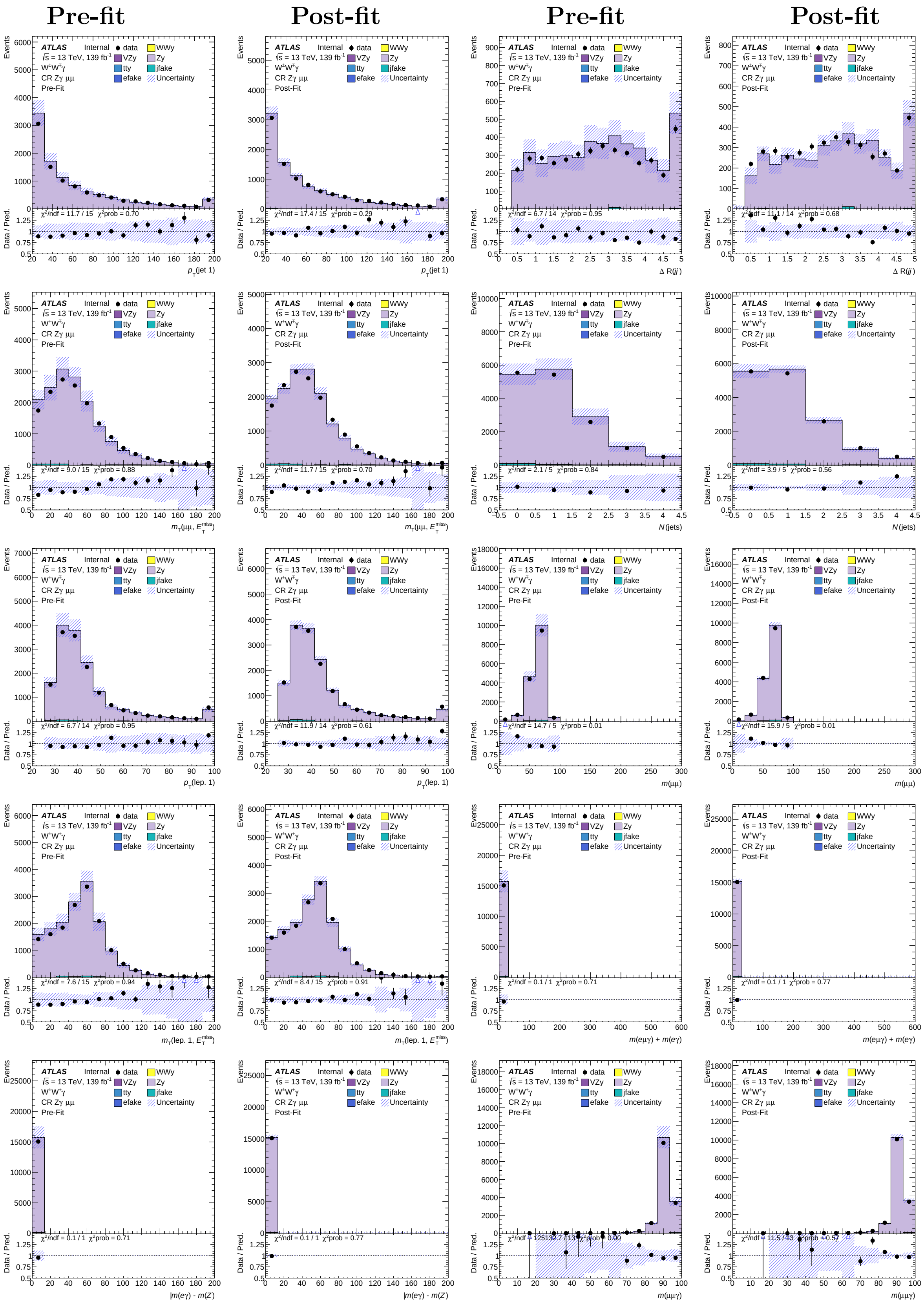

Figure A.15: Distributions of the various variables for events in the $Z\gamma$ control region with two muons (Left) pre-fit (right) post-fit. The uncertainties indicated in the figures include both statistical and systematic uncertainties. The post-fit result is obtained from the binned maximum likelihood fit with the control regions to data and is described in Section 11.2.1.

Appendix B

Feynman diagrams

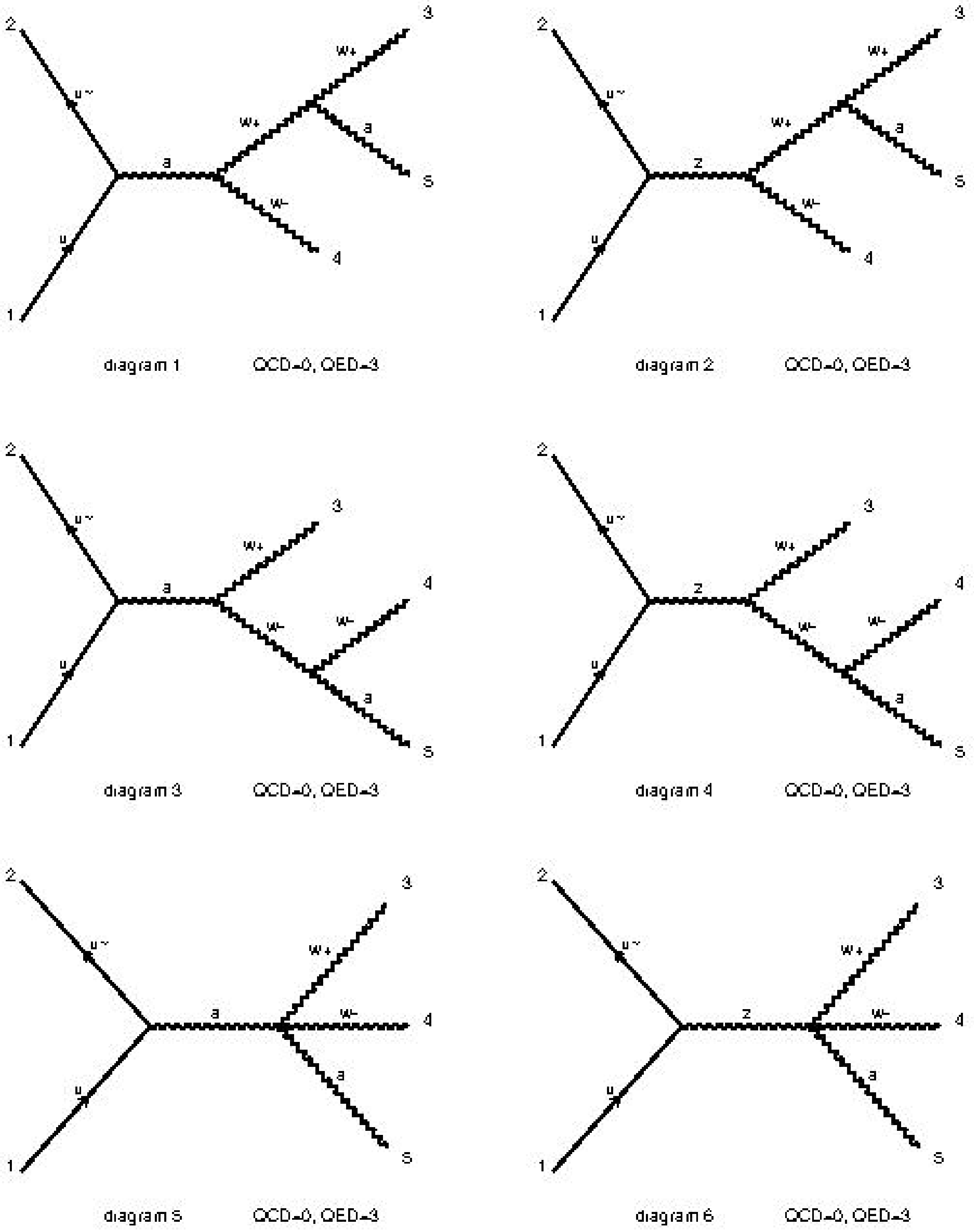

Figure B.1: Feynman diagrams for the LO $W^{\pm}W^{\mp}\gamma$ process produced with MadGraph.

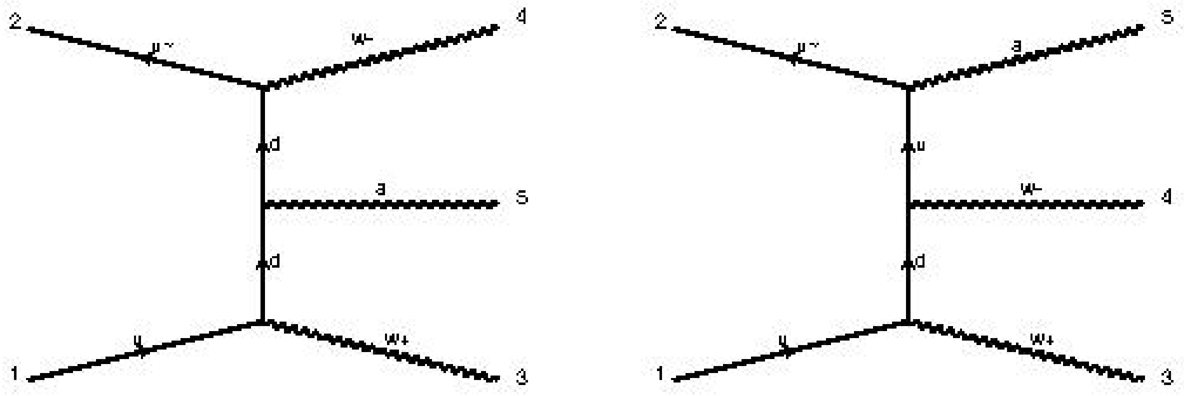

diagram 7 QCD=0, QED=3

diagram 8 QCD=0, QED=3

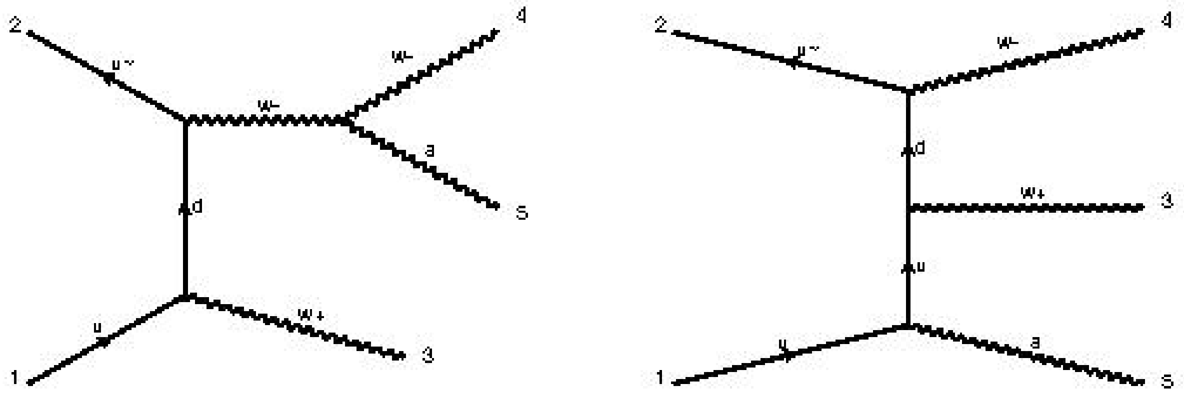

diagram 9 QCD=0, QED=3

diagram 10 QCD=0, QED=3

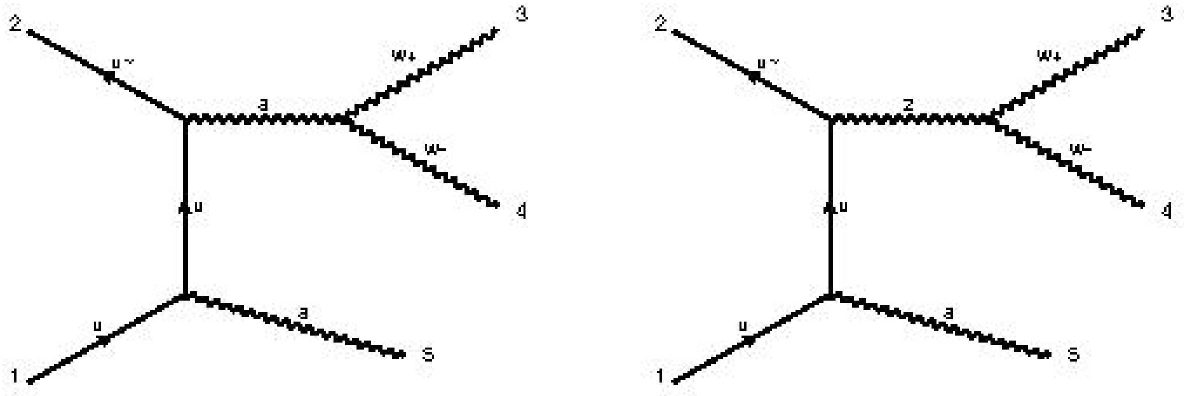

diagram 11 QCD=0, QED=3

diagram 12 QCD=0, QED=3

Figure B.2: Feynman diagrams for the LO $W^{\pm}W^{\mp}\gamma$ process produced with MadGraph.

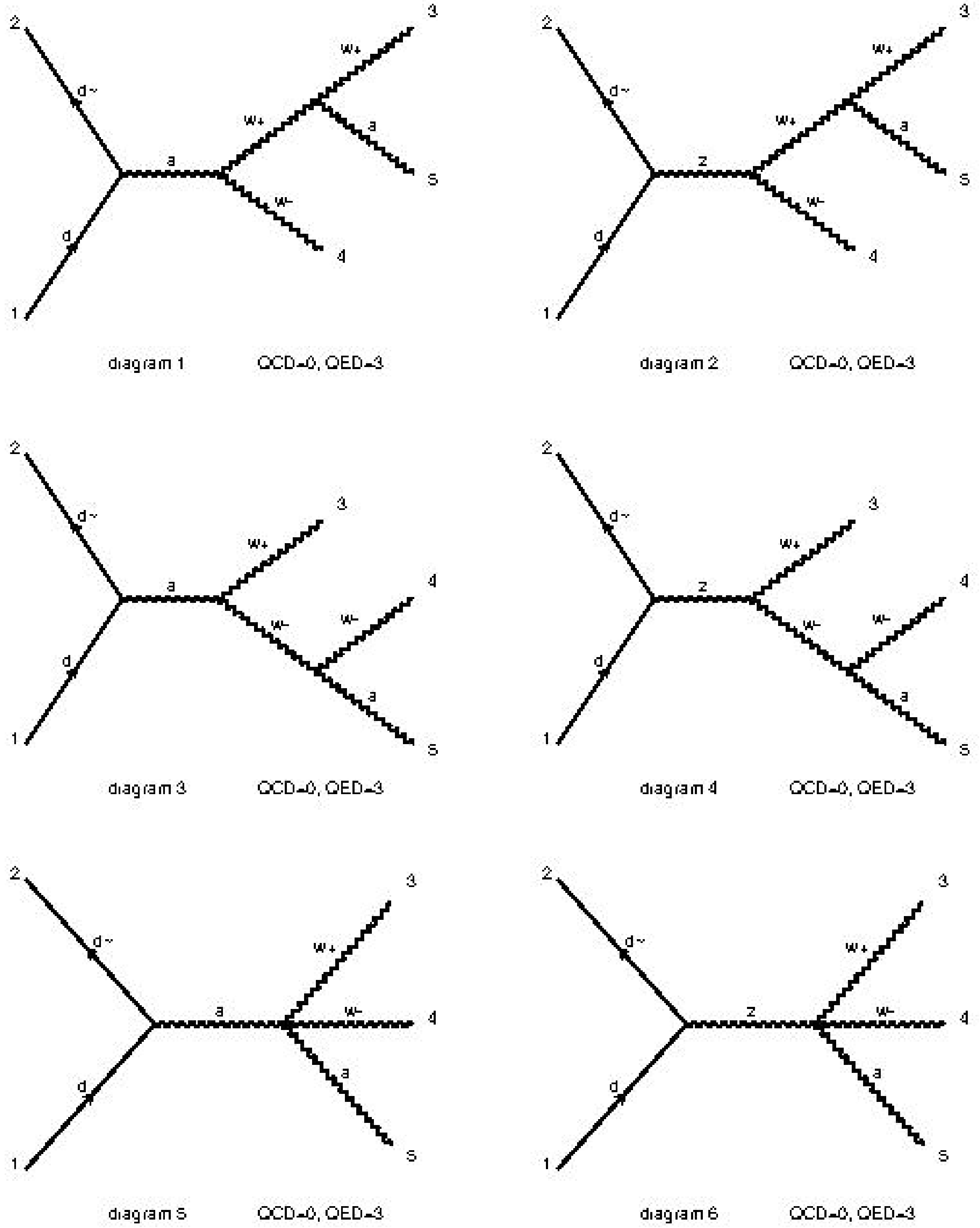

Figure B.3: Feynman diagrams for the LO $W^{\pm}W^{\mp}\gamma$ process produced with MadGraph.

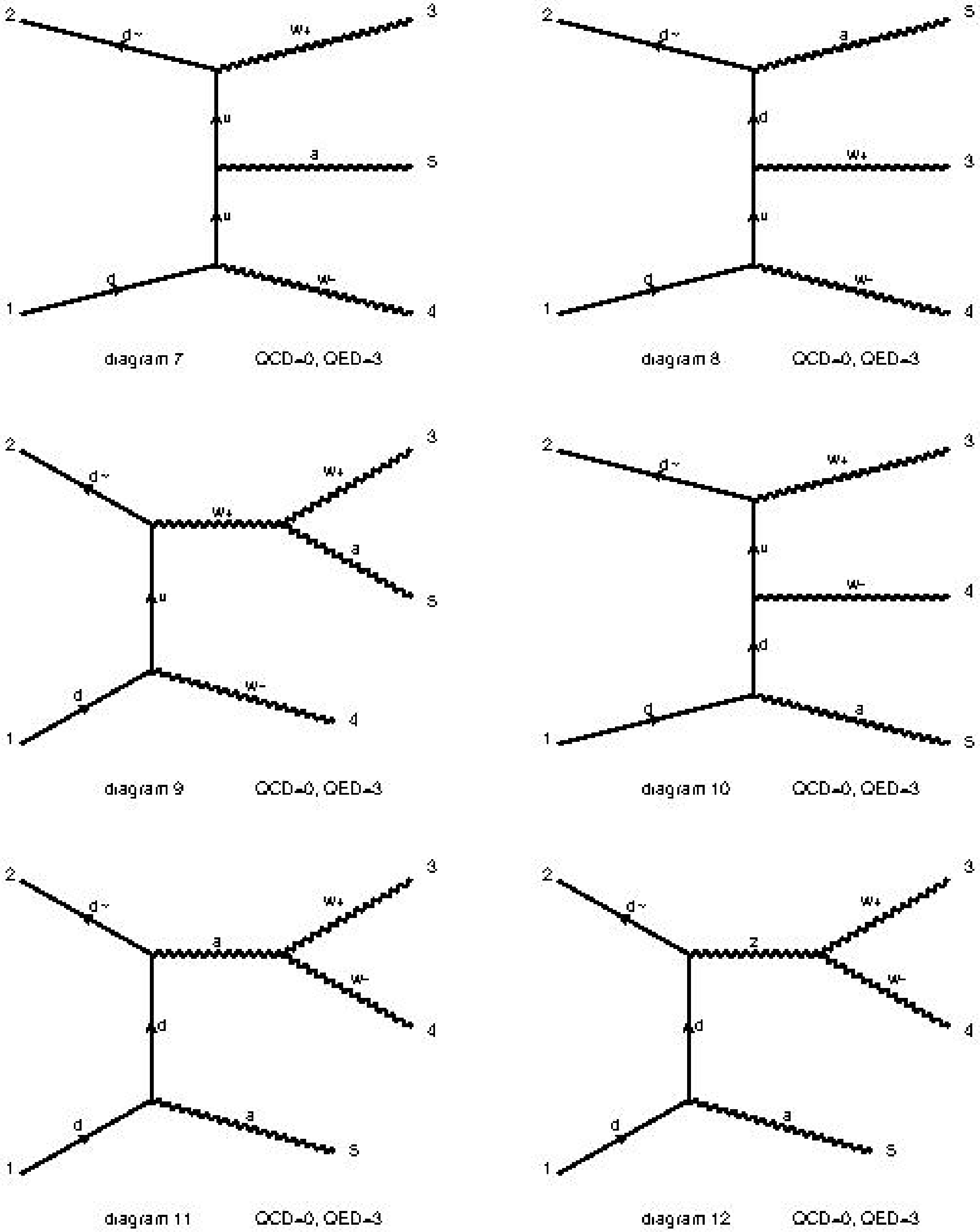

diagram 7 QCD=0, QED=3

diagram 8 QCD=0, QED=3

diagram 9 QCD=0, QED=3

diagram 10 QCD=0, QED=3

diagram 11 QCD=0, QED=3

diagram 12 QCD=0, QED=3

Figure B.4: Feynman diagrams for the LO $W^{\pm}W^{\mp}\gamma$ process produced with MadGraph.